UNIVERSITY OF CALIFORNIA
RIVERSIDE

An All-sky Search For VHE γ-Ray Sources With The Milagrito Water Cerenkov Telescope

A Dissertation submitted in partial satisfaction
of the requirements for the degree of

Doctor of Philosophy

in

Physics

by

Kelin Wang

September, 2001

Dissertation Committee:

Professor Benjamin C. Shen, Chairperson

Professor Cyrus M. Hoffman

Professor Allen D. Zych

The Dissertation of Kelin Wang is approved:

Committee Chairperson

University of California at Riverside

Acknowledgements

My long career as a graduate student now comes to a positive result. I never regret that I chose physics as my major, and I firmly believe that the time I spent both in Riverside and in Los Alamos National Laboratory will benefit me in my future endeavors. I would like to express my appreciation to a few people who supported, encouraged and guided me in my course of study:

I want to deeply thank my adviser, Professor Benjamin Shen, for his extreme patience and outstanding teaching, both in doing research and in making a good life. During all these years I had been away from my family, Ben cared about me like a father. With his guidance and support, I overcame a lot of difficulties in life. Any words I could say can hardly express my appreciation.

I also want to deeply thank my co-adviser, Dr. Cyrus Hoffman. My degree would never be possible without Cy's special guidance. For both his sagacity as a real physicist and his good personality, I enjoyed more and more working with Cy in Los Alamos, especially the last year before I left. I feel so lucky and honored to have Cy as my advisor, and I will always be grateful to him.

I want to thank Dr. Allen Zych, who so was kind to be my thesis committee when he was very busy. I also want to say thanks to his kindly care on me when I was his Teaching Assistant.

I want to sincerely thank Dr. Andrew Smith, who had been a big help to me. To tell the truth, I never found Andy was mistaken in research, neither in having an idea nor in processing a project. I surely believe that Andy will be fruitful in physics and I wish him very good luck.

Other post-doctors working in Los Alamos used to give me a lot of helps. I would like to express my appreciation to Dr. Frank Samuelson for teaching me so many computer skills, also to Dr. Javier Bussons-Gordo who is also my good friend, for helping me in working on my thesis.

The graduate students in Los Alamos, Morgan Wascko, Joe McCullough, Rob Atkins, Roman Fleysher and Lazar Fleysher, had made the experiment colorful. Roman and Lazar's movie, Joe's homepage on his car, Morgan's erudite knowledge on all kinds of special topics, ... I enjoy that we used to work togather and help each other, and I hope we can meet again in the future.

I would like to express my thanks to Isabel Leonor who gave me a lot of helps in doing research as a good friend. I hope her good luck in the future.

I will always thank the Milagro collaboration, for their contribution to make the experiment works.

My fiance, Guojie Liu, came to my life three years ago when I was in Los Alamos. Many thanks for the care and love she gave me. I will cherish our relationship and I hope we may create a wonderful future togather.

I want to thank my brother, Yalin, and my sister in-law, Xia, for their support for taking care of my parents for me when I studied in the States, especially during the period that our mother was ill. I feel so fortune to have such a good brother and a good sister in-law.

Everybody has parents, and I don't think I could repay my parents' love. My father has kept on supporting me during my career as a graduate student. My mother passed away right before I took the comprehensive exam in 1994. She chose not to tell me until her last breath because she did not want to influnence my career. I wish my mother could see my accomplishment in heaven today. I lovingly dedicate this thesis to my parents, especially to my mother. Thank you for being my parents, and thank you for everything all these years.

To my parents

Ms. Wenxiao Yin and Mr. Yunyong Wang

Especially dedicated to the memory of my mother
For her love
That I never have a chance to repay

ABSTRACT OF THE DISSERTATION

An All-sky Search For VHE γ-Ray Sources With The Milagrito Water Cerenkov Telescope

by

Kelin Wang

Doctor of Philosophy, Graduate Program in Physics

University of California, Riverside, September, 2001

Professor Benjamin Shen, Chairperson

Milagrito was the first large water-Cerenkov extensive air-shower detector sensitive to TeV γ-rays. A search for steady TeV point sources in the northern sky has been made with data from Milagrito. Over 8.9×10^9 events were collected from February 1997 to May 1998, of which 1/3 have been used in this study. The searched region was between -5° and 71.7° in declination and all right-ascension. No statistically significant excess above the background from the isotropic flux of cosmic rays was found for any direction of the sky. Upper limits at 90% confidence level were derived for the photon flux above 1 TeV from any steady point sources in the whole northern sky.

Contents

List of Figures

List of Tables

Chapter 1

Introduction

1.1 Very-High Energy (VHE) γ-Ray Astrophysics

Astrophysics is a science which studies the physical processes taking place beyond the atmosphere of the Earth, in the stars, galaxies, clusters or other celestial bodies [1]. An astronomical observation requires measurement of particles, which carry the information from a celestial body to us. Those particles must be stable, otherwise the information they carry from the source will be lost due to the long journey to the Earth.

1.1.1 Particles From Celestial Bodies

Basically there are 3 types of stable particles in the universe: charged particles, photons and neutrinos. Gravitons are considered to be stable, but there is no experimental evidence of their existence. The lifetime of a neutrons is about 13 minutes. It decays into a proton, an electron and an anti-neutrino. A 1-TeV (1 TeV = 10^{12} eV) neutron may survive for about a week in the rest frame of reference, which is much longer than some unstable particles, such as pions or muons. With the one-week lifetime, a 1-TeV neutron trvavels ~0.02 light year. However, compared to intergalactic distance, which is normally in unit of pc (1 pc = 3.26 light year), this is extremely short. Celestial neutrons of a few TeV which are detected on the Earth can only possibly come from the sun or other celestial objects inside our solar system. Thus using neutrons as an information carrier for the universe is not applicable.

Cosmic rays are charged particles, $\sim 90\%$ of which are protons, the rest are mostly α particles (Helium nuclei). Although cosmic rays are stable radiation, they cannot be used as the information carrier of astronomical observation. The reason is that because there are many unknown intergalactic magnetic fields in the universe, cosmic rays will interact with the magnetic field and therefore travel in irregularly bent trajectories. So when a cosmic charged particle reaches a detector, one cannot trace the charged particle back to its origin. In fact, cosmic rays appear to come from all directions of the sky and form an isotropic cosmic-ray background [2].

The neutrino was predicted by Pauli in 1932, and was first detected in the 1950s. Most physicists believe that neutrinos are neutral, stable and nearly massless leptons which have a huge flux in the universe with respect to other elementary particles. However, because of the tiny weak interaction cross section, it takes a long time to accumulate a statistically significant observation in any of the current neutrino detectors.

In addition to the many neutrino experiments that are being performed to study neutrino oscillations [3][4][5], there are several neutrino experiments to search for celestial objects as neutrino sources [6][7]. The basic idea is to build a big detector under a thick overburden which attenuates cosmic rays and muons so that only neutrinos can penetrate the overburden and reach the detector, and possibly generate muons via weak interactions with the medium in the detector. To realize this idea, the experiments are usually built in deep caves in the earth or in the polar ice; some use the whole earth as a huge overburden as well as the detector for the cosmic neutrinos bombarding the other side of the earth.

Using photons to observe celestial bodies is an ideal choice, since photons do not bend in magnetic fields. In addition, photons can be detected with high efficiency.

1.1.2 VHE Region In The Electromagnetic Spectrum

Very-high energy (VHE) γ-ray astrophysics, in which one observes 300 GeV to 300 TeV (1 GeV $= 10^9$ eV) γ-ray emission, is a relatively new field. Since the 1980s, a few of strong galactic and extra-galactic sources of photons above 1 TeV have been observed [8][9][10], which gave birth to VHE γ-ray astrophysics. Despite significant progress in observations in the last 2 decades, the knowledge of high-energy photon sources is still rather limited. We do not know how many very-high energy sources exist, nor the energy spectrum of those sources.

The VHE region is one part of the electromagnetic spectrum which astronomers have not studied thoroughly. Every time a new region of spectrum had been studied, some new physics was discovered. For example, Supernovae were first observed based on the observation in the optical region (energy $\sim$ 1 eV), and Hubble's Law was proposed from the study of red shifts [11]; another example is the observation of the radio spectrum (energy $\sim 10^{-4}$ eV) of celestial bodies, in which many radio-loud pulsars, and the 3K Cosmic Microwave Background Radiation (CMBR) were discovered [12]. We expect that TeV γ-ray observation will open a new window to astrophysics as well.

1.1.3 Physics Of γ-ray Emission

How are the high-energy γ-ray photons produced in celestial objects? i.e. what are the physics processes leading to the emission of γ-rays? There are the following possible processes: particle decay, synchrotron emission, inverse Compton scattering (ICS), bremsstrahlung and other non-thermal processes.

There are many hadronic interactions taking place in the galaxies, where many pions are produced. A neutral pion decays into 2 photons. The energy of those 2 photons could reach GeV to TeV depending the original energy of the pion.

When a high energy charged particle interacts with a low energy photon (normally in the microwave regime), the energy will be transfered from the charged particle to the photon, resulting in a high-energy photon is produced. This process is called inverse Compton scattering.

Strong synchrotron emission is given off when charged particles, normally electrons and positrons, are accelerated in a magnetic field [13]. For a relativistic charged particle, the total energy loss in the laboratory frame is [11]:

$$-\frac{dE}{dt} = \frac{e^4 B^2}{6\pi\epsilon_0 c M^2}\frac{v^2}{c^2}\gamma^2 sin^2\theta \tag{1.1}$$

in which E is the energy, B is the magnetic field, M is the mass of the charged particle, and θ is the angle between the velocity and the magnetic field. Equation 1.1 shows that the energy loss for synchrotron radiation is inversely propotional to M^2; consequensively, light particles, such as electrons/positrons, will lose much more energy than heavier particles, such as protons/anti-protons.

TeV γ-ray radiation from the supernova remnanets (SNRs) such as the Crab Nebula, are believed to be caused by the combination of synchrotron emission and ICS. The synchrotron emission generates high energy electrons/positrons and low-energy photon “clouds”. When these “clouds” interact with high-energy particles, high-energy photons will be generated via ICS. [1] The same processes could take place in Active Galactic Nuclei (AGNs), which give rise to high-energy photons.

Bremsstrahlung occurs when a high energy charged particle (normally an electron or a positron) interacts with the electromagnetic field of an atomic nucleus. The

---

[1] The high-energy particle which interact with the low-energy ”clouds” are not necessarily the same electrons/positrons in the sychrotron emission.

charged particle will lose some energy by emitting a high-energy photon. This process also happens when a charged particle interacts with the atmosphere of the earth, which contributes to the formation of an extensive air shower (EAS).

1.2 What Has Been Observed Recently

One of the most fruitful experiments in last decade is the Compton Gamma Ray Observatory (CGRO) project. CGRO is a satellite project operated from 1991 to 2000. It has four detectors: EGRET, BATSE [14], OSSE [15][16] and COMPTEL [17][18].

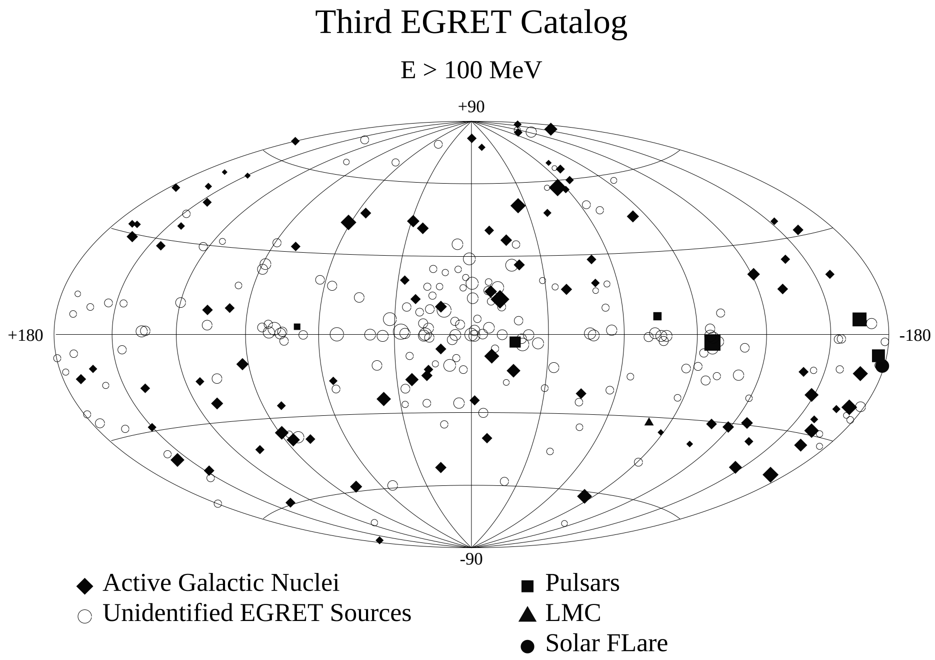

Figure 1.1: All-sky γ-ray map(E > 100 MeV) from EGRET in galactic coordinates.

EGRET, which stands for Energetic Gamma Ray Experiment Telescope, used a spark chamber to detect γ-rays in the energy range from 20 MeV to 30 GeV. EGRET discovered more than 270 γ-ray sources since 1995 [19], as shown in an all-sky γ-ray map above 100 MeV (Figure 1.1). In this map, the Large Magellanic Cloud, 5 pulsars, 1 radio galaxy, 93 blazars are identified, and the remaining 170 sources are not yet identified with known celestial objects. Most of the sources, for instance, the known pulsars, are located in the galactic plane, and there are also sources outside our galaxy, such as radio galaxies, blazars and quasars.

The interesting results of EGRET greatly increased the understanding of high-energy astrophysics. Some new physics, such as the processes of generating high energy photons, could be studied based on the new observations. In EGRET's all-sky map, how many of the sources have TeV emission? Are there any other TeV sources which EGRET did not detect? To answer those questions, TeV γ-ray observations need to be performed.

1.3 Ground-based Techniques

1.3.1 Flux of VHE particles

An empirical power law formula describes that the flux of VHE particles, both charged particles and photons, drops dramatically as the energy increases,

$$\frac{dN(E)}{dE} = C * E^{-r} \tag{1.2}$$

in which C is a constant. For charged particles, such as protons, the range of r is 2.6-2.8; for photons it is 2.0-2.4. Note: for different sources, both r and C are different. For example, the γ-ray flux for the Crab (measured by Whipple Observatory [20]) is:

$$J_\gamma = (3.20 \pm 0.17 \pm 0.6) \times 10^{-7} \times (\frac{E}{TeV})^{-2.49 \pm 0.06 \pm 0.04} m^{-2} s^{-1} TeV^{-1} \tag{1.3}$$

in which the first error (±0.17) is statistical and the second (±0.6) is systematic.

In order to accumulate a sufficient number of events, a detector of extremely large area is needed, which makes satellite-borne experiments impractical. For TeV γ-ray observations, ground-based techniques are used.

1.3.2 Extensive Air Shower (EAS)

TeV particles interact with atmospherical molecules before they reach the ground. The interactions of TeV particles and the atmosphere generate a huge number of secondary particles which forms an extensive air shower (EAS). For particles involved only in electromagnetic interactions, such as electrons, positrons and photons, the thickness of the atmosphere equals approximately 27 radiation lengths.

There are 2 types of EAS' developed by high-energy particles. The first type is an electromagnetic shower generated by high-energy photons (Figure 1.2). When a photon hits an atmospheric nucleus, it converts into an electron-positron pair. This pair of particles emit photons by Bremsstrahlung when they are slowed down in the atmosphere. The secondary photons convert into electron-positron pairs again since their energies are still high enough to produce pairs. This pair-Bremsstrahlung process is the key process of energy loss, as long as the energy of the particles are high enough. When the energy of the secondary particles drops to a critical level ($\sim$80 MeV), the energy loss by Bremsstrahlung is equal to that of ionization, so the number of particles in an EAS reaches its maximum. At lower energies, ionization becomes the dominant process of energy loss. When a TeV electromagnetic shower hits the ground, there are more photons than charged particles, the ratio of number of the photons to the number of charged particles is about 4:1.

The second type of EAS is a hadronic shower generated by high-energy charged particles, or cosmic rays. In this kind of air shower, the first generation of secondary particles are pions, hadrons and nucleons, and more pions can be generated in further interactions. A neutral pion will decay into 2 photons quickly, and these 2 photons will develop an electromagnetic shower, just like the first type of showers mentioned above. A charged pion will decay into a muon and a neutrino. A muon will lose

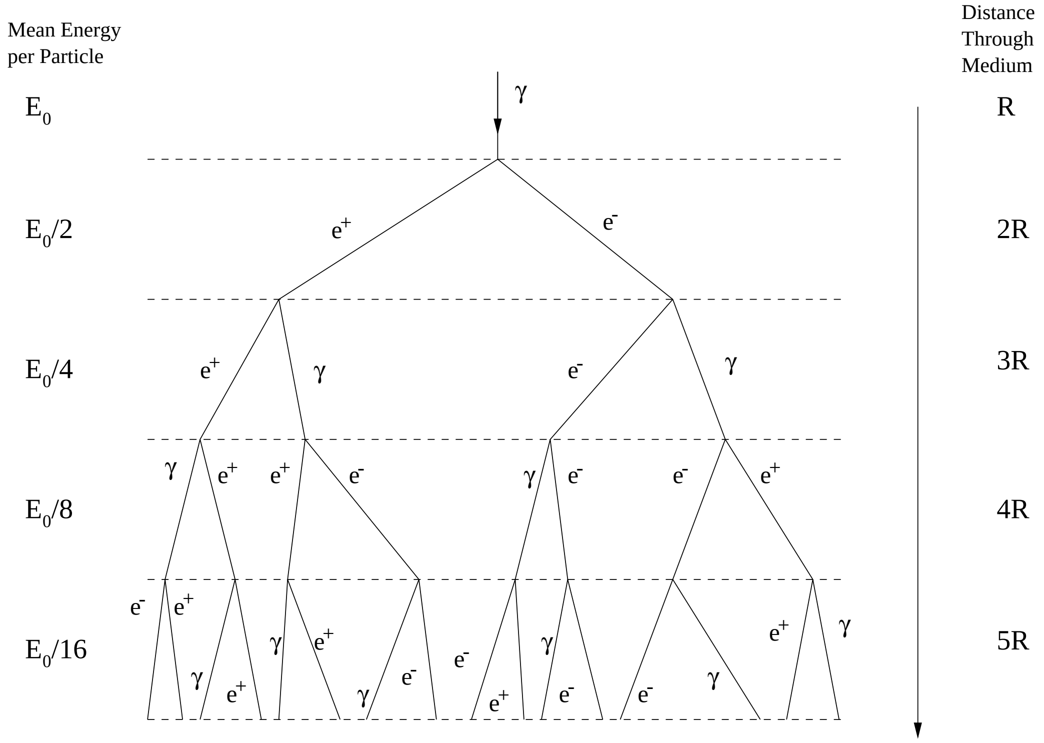

Figure 1.2: Development diagram for an electromagnetic EAS.

energy mainly by ionization and can survive to the ground.

Since there are numerous charged pions in the secondary particles of a hadronic shower, there tends to be many muons in a hadronic shower. The main difference between electromagnetic showers and the hadronic showers is thus whether there are muons in them.

1.3.3 Ground-based Experimental Techniques

Basically, 2 types of ground-based experimental techniques have been used to observe EAS' before the Milagro project: Scintillation counter arrays (SCAs) and air

Cerenkov telescopes (ACTs).

In a SCA a large number of scintillation counters are placed at regular intervals, so that a large surface area is instrumented. When an EAS enters into the area, the counters of the detector are triggered. Each counter in the array records both the relative time and pulse height information. The collective information from all the counters samples the charged particles of the EAS. The shower direction can be reconstructed by using the relative time and pulse height information of each counter in the SCA. (Figure 1.3). The CYGNUS project [21], which operated from 1986 to 1996 in Los Alamos National Laboratory, is an example of this technique; and the CASA-MIA project [22] used this technique as well.

The advantages of a scintillation counter array (SCA) are that it can be operated all the time, despite of the weather, and it is sensitive to the whole sky; i.e. it has a high duty factor ($\sim$ 95%) and a large aperture ($\sim$1sr). The limitations of this technique are that it has an extremely high energy threshold (CYGNUS' energy range was 20 TeV$\sim$100 PeV, CASA's was 50TeV$\sim$100 PeV [22]) because it only samples charged secondaries over a very small fraction of the area of an EAS (0.5% in CYGNUS).

An ACT collects the Cerenkov radiation produced by the charged particles of an EAS, when the speed of these particles exceeds the speed of light in the atmosphere. The Cerenkov light is collected by many small optical mirrors or a big parabolic mirror, and then projected to a focus, at which there is an array of Photo-multiplier Tubes

(PMTs); the collected light forms an "image" of the EAS. Many projects use ACT for observation, such as the Whipple Observatory in Arizona [10][23], CANGAROO in Australia [24][25], and HEGRA in the Canary Islands [9][26].

The advantages of the ACT technique are that it has relatively low energy threshold (100 GeV), and excellent background rejection since the image of an electromagnetic shower differs significantly from an hadronic shower. The drawbacks of the ACT technique are that this kind of telescope can only be operated on moonless and cloudless nights, and each time it must point to a certain source in the sky; i.e. it has a low duty factor ($\sim 5\%$) and a small aperture ($3^\circ \sim 5^\circ$) of sky. Some TeV sources are not stable over time, and all sources only show up at night during a specific period of a year, so an ACT telescope cannot monitor the whole sky, nor can it monitor a given source at all times.

1.4 The Milagro Project

Milagro, which means "Miracle" in Spanish, is designed to combine the advantages of both techniques, while minimizing the disadvantages of each technique. To realize this, Milagro uses the Water Cerenkov Technique (WCT).

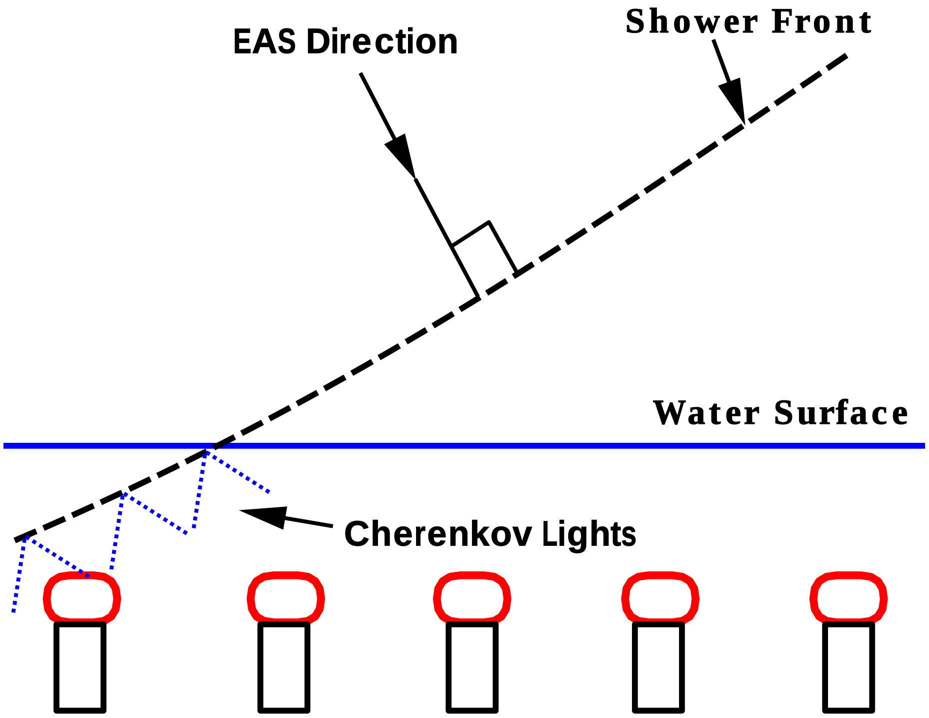

Figure 1.3: The direction reconstruction of an EAS for a water-Cerenkov detector. Each Photo-multiplier tube (PMT) meansures the relative time and pulse height of an EAS. The direction reconstruction for a SCA is the same as for a water-Cerenkov detector.

1.4.1 Water Cerenkov Technique

Milagro is designed to use 2 layers of PMTs in a water pond, with a light-tight cover. The top layer, refered to as the shower layer, consists of 450 PMTs separated by 2.8 meters. It is placed 1.5 m under water to detect the Cerenkov light from the electromagnetic secondaries of the shower. The bottom layer, consisting of 173 PMTs under 7 meter depth of water and also separated by 2.8 meters, has more sensitivity to the muons in the shower. The shower layer is used to trigger the detector and to reconstruct the direction of showers, whereas the bottom layer is used to do the background rejection.

In this technique one collects Cerenkov light produced by the shower particles, since the speed of shower particles in water is larger than the speed of light in water. The shower reconstruction of Milagro is the same as in the Scintillation Counter Array, each PMT collects the relative arrival time of an EAS it samples, so the shower direction can be determined.

1.4.2 Advantages Of Milagro

Milagro keeps the advantages of Scintillation Counter Arrays: High duty factor and large aperture to the sky, so it can monitor every source and simultaneously conduct an all-sky survey.

Compared to a Scintillation Counter Array, Milagro has a much lower energy threshold because of the usage of WCT. When an EAS hits the detector, charged particles emit Cerenkov photons in the water, and high-energy photons convert into electron/positron pairs while colliding with water molecules, and those electron/positron pairs emit Cerenkov radiation as well. Since the ratio of number of photons to charged particles in an EAS is 4:1, Milagro samples many more particles of an EAS than a Scintillation Counter Array. Also, the Cerenkov angle in water is about 41°, which means the Cerenkov light covers most of the detecting area. Thus, although the PMTs are separated by 2.8 meters from each other so they cannot possibly collect all the photons, they may collect some photons generated from most of the relativistic particles. A typical SCA has an energy threshold of 50∼100 TeV, whereas Milagro has an energy threshold below 1 TeV even at a trigger threshold of 100 PMTs (See section 2.4).

The muon layer of Milagro is used for background rejection. The muon layer may tell whether an EAS is a γ-ray shower or a hadronic one by the the distribution of pulse height collected by the PMTs. When a muon hits the muon layer, only a few nearby PMTs have very big signals. When an electromagnetic shower hits the pond, the muon layer will not have this kind of phenomena because there is no muon in the shower. Due to the information collected in the muon layer, Milagro has some background rejection capability.

1.4.3 Physics Goals For Milagro

Milagro is the first WCT telescope which can monitor the entire northern sky. All known sources are to be confirmed by Milagro, further more, they will be monitored all the time in order to collect more information for further study. It is hoped, that Milagro may discover some new sources, both by blind searching and by non-blind searching if there are some candidate sources. We also hope to see some Gamma-ray Bursts (GRBs) with Milagro since there is no conclusive evidence that a GRB has radiation in the TeV range [27]. Other interesting topics, such as primordial black holes and solar physics, can also be studied by using Milagro data.

1.4.4 Milagrito - The 2nd Prototype Of Milagro

There were 2 prototypes constructed and run before Milagro. Since there are many uncertain things of the detector that need to be determined, such as the problems of PMTs under the water, the efficiency of the online software package, the stability of the calibration setup, etc, it is good to use prototypes in advance so that Milagro can be more successful. Also, the research of prototype detectors offers the general idea and information on how a WCT really works, such as the sensitivity.

The very small prototype of Milagro, Milagrisimo, consisted of only 28 PMTs distributed in the same water pond of Milagro. Milagrisimo was built during May to November 1995 and it took data for 3 months, during April to June 1996 [28]. The experience from this prototype led to the preparation for PMTs.

The 2nd stage prototype of Milagro, Milagrito, consisted of 228 PMTs distributed in the same water pond of Milagro as well. Milagrito was a one-layer prototype of Milagro and was the first big water-Cerenkov telescope for TeV γ-rays [29]. Milagrito was constructed from May to October 1996, and it took data for 15 months, during February 1997 to May 1998. There were $\sim$9 billion events accumulated.

My thesis is based on an all-sky survey using Milagrito. I will describe the Milagrito detector in the 2nd Chapter, and then the event reconstruction in the 3rd Chapter. The 4th and the 5th Chapters will be devoted to the discussions of the simulation and analysis technique. The results will be given in Chapter 6.

Chapter 2

The Milagrito Experiment

2.1 Detector And Site

2.1.1 Experimental Design

Milagrito, which was the prototype of Milagro and also the first large water Cerenkov detector for γ-ray observation in the world, was similar to the top layer of Milagro. It used PMTs deployed under 0.9∼1.5 m of water to detect the Cerenkov photons produced by relativistic charged particles of the EAS in the water. The water above the PMTs should be thick enough to allow all the photons to convert into electron-positron pairs, but should not be so thick that photons are absorbed by the water before they reach the PMTs. The results of Monte Carlo simulation showed that optimal depth of water above the PMTs ought to be 1∼2 meters. About 9 billion events were recorded with Milagrito with a water depth of 1 meter (6.2 billion

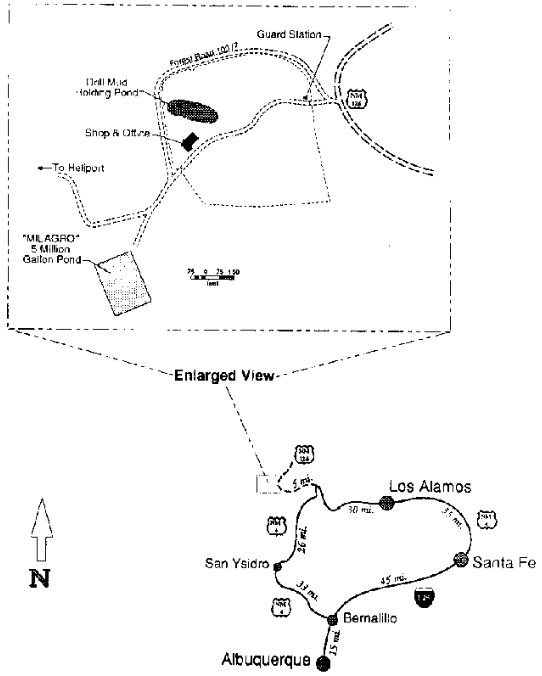

Figure 2.1: Location of Milagrito experiment site.

events), 1.5 meters (1.9 billion events) and 2 meters (1.8 billion events).

Milagrito used 228 PMTs located in a plane on a grid of 2.8 m × 2.8 m. Since the bottom of the pond is not flat (Figure 2.3), all PMTs were tied to the bottom with short strings of various length in order to be in a horizontal plane. The PMTs are lighter than the water, so they will float vertically in the water. When an EAS hits the pond, each individual PMTs collects the photons produced by the relativistic particles of the EAS. Thus the arrival time of the shower can be measured, and the direction of an EAS can be reconstructed (Figure 1.3).

Figure 2.2: Aerial picture of Milagro site.

2.1.2 The Water Pond

Milagrito was built in the same water pond that now houses Milagro. The Milagrito experimental site, which used to be the site for the Hot Dry Rock geothermal energy project in the Jemez Mountains, is located at 35.9° N and 106.7° W, about 32 miles away from Los Alamos (Figure 2.1). This pond has an altitude of 2650 m above sea level. The total volume of the pond is about 21 million liters. The surface of the pond is a rectangle of 82 m in length and 61 m in width; the sides of the pond are sloped which lead to a smaller bottom of 52 m in length and 30 m in width. The depth of the pond is 7.6 m at the edges and 8.2 m at the center because the bottom is not flat (see Figure 2.3).

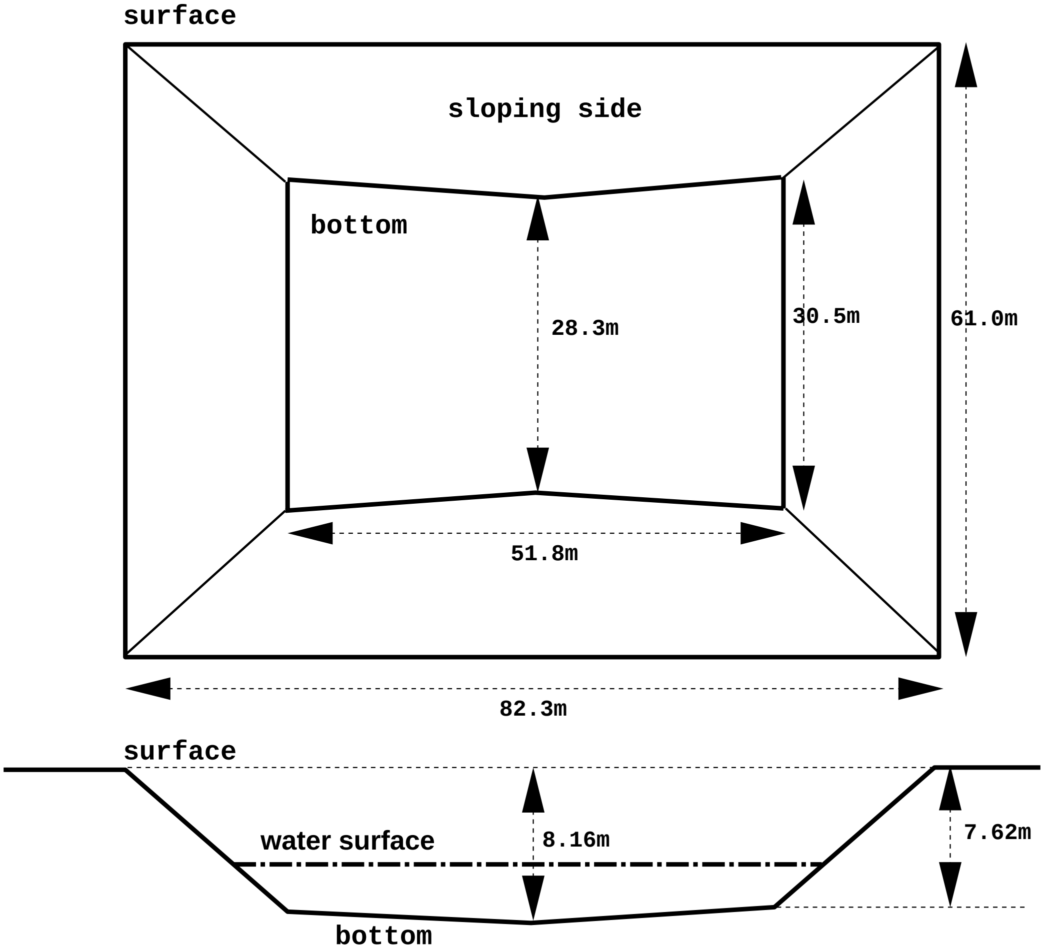

Figure 2.3: Geometry of the water pond for Milagrito.

2.1.3 PMTs And Cables

The PMTs are the key part of Milagrito telescope. To measure the arrival times of different points of the shower front, which differs by several ns (10^{-9} second), the PMTs must have very good time resolution. In order to collect as much light as possible and also to be sensitive to very weak light, the PMTs must have high efficiency and a large photo-cathode area. In addition, the intensity of Cerenkov light varies over a wide range because the number of the relativistic particles varies from shower to shower, therefore a good PMT should have good charge linearity over a wide dynamic range.

Considering the requirements above, the 20-cm-diameter Hamamatsu 10-stage R5912SEL PMTs were used. Each PMT was encapsulated in a PVC housing to be waterproof. A silicone conformal coating was put on each PMT base to protect the components from humidity.

The dark noise of each PMT were studied in order to determine their working voltages. For a same amplitude of dark noise for each PMT, the working voltages varied from positive 1600v to 2200v, and the gain at this voltage is $\sim 10^7$. The passive base of each PMT had a resistance of 20 MΩ. One 75 Ω coaxial cable (RG59) connected a PMT to the control room, supplying the high voltage to the PMT and conducting the PMT signal to the electronics, i.e. this cable is used for both the power line and the signal line. All the cables had the same length of 137 m.

The photo-cathode in the PMT responds to light of wavelength 300 nm$\sim$650 nm, with a peak efficiency at 420 nm. To measure the linearity of the PMTs before they were installed inside the pond, a 337-nm Nitrogen laser with $\sim$0.3 ns pulse width was used. The result of testing several PMTs (Figure 2.4 and Figure 2.5) shows that the gain for a typical PMT is $\sim 2 \times 10^7$, and the PMT is linear up to $\sim$75 photoelectrons (PEs).

2.1.4 Water Filtration

The water in the pond should be as transparent as possible in order to reduce the attenuation of light. The water was drawn from a deep fresh water well located on the site, and a water-filtration and recirculation system was installed in the pond utility building (PUB) next to the pond. Figure 2.6 is a schematic diagram of the water filtration system of Milagrito.

When the filtration system is in filling mode, the water from the well was pumped through a media filter, then through a carbon filter, a softener, a 1.0μm filter, a UV lamp and a 0.2μm filter before it enters the pond. The water softener exchanges the "hard" ions (Mg^{++} and Ca^{++}) by "soft" ions (K^+ and Na^+) to avoid the deposition of $MgCO_3$, $MgSO_4$, $CaCO_3$ and $CaSO_4$ on the surface of PMTs. The media filter was used only during the filling. When the filtration system is in circulation mode, water from the pond by-passed the media filter and the water softener. The UV lamp was used to kill the living organisms, which are normally $\sim$0.5 μm in size.

After the filtration of 0.2μm, the attenuation length for 337-nm-wavelength light was $\sim$4 meters. (Figure 2.7)

2.2 Electronics

The main function of the electronics was to receive and to convert raw analog signal from each PMT channel, including both timing and pulse height, into digital information. The output of the electronics was the input to the online data acquisition system (DAQ).

The raw signal from the HV cables connected to the PMTs enters the input of a custom-made “analog board”(Figure 2.8). The signal was AC-coupled to the amplifier inputs by a high-voltage capacitor so that the DC part of the signal was blocked. The AC coupled signal was split and passed through 2 amplifiers of different gains. The output from the low-gain amplifier was input to the low-threshold discriminator, whose threshold was set to a level equivalent to ∼1/4 PE. The output from the high-gain amplifier was split into 2 paths. One output went to the input of the analog-to-digital converter, an external FASTBUS crate, after passing through a 25 ns delay-line chip. The other output went to a high-threshold discriminator, whose threshold was set to a level equivalent to ∼5 PEs. Both discriminators generate standard ECL pulses which are ToTs (Time over Threshold), and the ouputs of these two discriminators are added togather for the same pulse. Thus a pulse less than ∼5 PEs generates a 2-edge event, which is simply a low-ToT; and a pulse larger than ∼5 PEs generates a 4-edge event, which is a high-ToT inside a low-ToT. (Figure 2.9).

The ToT output were the input to a “digital board”, which was also custom-made. Both the high-ToT and the low-ToT for each PMT channel were passed to the time to digital converter(TDC), in an external FASTBUS crate. The low-ToT, however, was also used to provide trigger and monitor information. Each low-ToT passed through a discriminator and generated a fixed-duration, 300 ns pulse of 25 mV amplitude.

The analog summation of these signals supplied the trigger information.

The ToT output from the digital board went to the TDC modules. A TDC module recorded all the rising and falling edges and then digitized the information. (1 ns = 2 TDC counts). The timing information of the events was recorded by reading the output of a 137/2 FASTBUS GPS clock. There were 3 LeCroy 1887 FASTBUS TDC modules used in Milagrito, each module having 96 channels. In addition, a LeCroy 1881M FASTBUS ADC module was used to digitize the analog output from the analog board. This digitized information from the ADC was only used for calibration purposes.

2.3 Data Acquisition

The Data Acquisition system (DAQ) received the trigger, read the digitized data from the TDC modules, and passed the data to the online computer. This computer did the online analysis and stored the useful information onto its hard drive. The DAQ included a FASTBUS smart crate controller (FSCC), VME system, and a Silicon Graphic (SGI) Challenge L multi-CPU computer. The VME system included a pair of dual-ported VME memory modules, a smart controller (Access Dynamics DM115/DC2, or DC2), and an external VME crate. (Figure 2.10).

The digital output from the TDCs were read by the FSCC. The FSCC then transfered the data to one of the two VME modules, which were connected in series, via the DC2. The DC2 wrote the data into its memory boards. The SGI computer read data from the memory board over the VME bus.

The experiment was controlled by commands from the SGI computer. The computer used the Unix operating system and communicated with the FSCC via ethernet. The communication was performed by running socket (a type of Unix Inter Process Communication (IPC) code written in C language) routines at the FSCC and SGI respectively. Thus the SGI could initialize the FASTBUS modules and prepare the system for data taking.

The online data processing was executed by routines written in C language. The event calibration and reconstruction were performed at the same location of the computer memory by applying the shared memory technique. A third routine accessed the reconstructed data and wrote it out to the hard drive.

Both the raw data and reconstructed results were saved so that the off-line reconstruction could be repeated. The data temporarily existed on the disk and then was archived to DLT tapes.

2.4 Trigger Rate

The trigger threshold of Milagrito was set to ∼2.5 V, which required at least 90∼100 PMTs triggered. A trigger was generated when signals from more than 90∼100 fired within a period of 300 ns. Under this trigger threshold, the trigger rate for Milagrito was 300∼400 Hz. It takes ∼750 ns for the DAQ to complete processing a trigger, resulting in a dead time of less than 5% of the electronics.

The trigger rate for the entire Milagrito lifetime is shown in Figure 2.11. Whenever there was water or snow on the cover, the trigger rate dropped because the air shower particles lost some energy before they entered the water pond. In fact, the Monte Carlo result had confirmed this. The snow season of the site is from October to April, so the trigger rate changed frequently during this period because the snow on the cover sometimes accumulated and sometimes melted as the weather changed. For example, there was a lot of snow in February 1997, and very little snow in March 1997, which resulted in a change of trigger rate from 140 Hz to 300 Hz.

For most of the lifetime of Milagrito (from February 1997 to February 1998), the water depth above the PMTs was 1.0 m, and the trigger rate was around 300 Hz. After February 1998, more water was pumped into the pond, so more Cerenkov photons were generated and sampled, therefore the trigger rate went higher.

2.5 Operation Of Milagrito

The operation of Milagrito began on February 8, 1997 (Julian Date 50487) and ended on May 7, 1998 (Julian Date 50940). Most of the data were taken with 1 m, 1.5 m, or 2 m water above the PMTs. Data were acquired continuously except for some periods of construction.

Since the experimental site is about 35 miles away from the laboratory, Milagrito operated largely unattended. An environmental monitoring system (EMS), which was developed by U. C. Riverside, was built at the site to monitor and control the experiment.

The function of the EMS is to periodically monitor the experimental conditions, such as the trigger rate, HV of the PMTs, depth of water, temperature, water pressure of the water recirculation system, status of tape drive, etc. The information were collected by various sensors and meters in the experiment. All the information was written onto an internet EMS homepage located in a personal computer in the control room at the site, which was used as the EMS server. The homepage is automatically updated once every 5 minutes while monitoring the experiment. The shift person can access the EMS homepage through an internet navigator from any office computer. This server-client system allows the remote control of the experiment. For security purposes, an internet firewall and password protection were put on the system.

Milagrito used a motor generator system, the M.G. set, to buffer the power supply for the experiment. The output power of the M.G. set is very stable even if its input power is unstable, and protected the experiment from the trouble or damage caused by unstable power. In case of bad weather (rainy, windy, etc.), the M.G. set turned off automatically, which avoided accidents when nobody was at the site.

When there was a serious error condition, such as the loss of electrical power, an abnormal event rate (including zero), or an abnormal pressure of the water recirculation system etc., an automatic alert was generated by the EMS and the shift person was paged. Less serious errors could be corrected remotely through the internet. For example, individual HV channels could be turned on or off and the data-taking SGI computer could be rebooted remotely. For serious errors, which were mostly weather related (snow or high winds), the shift person had to restart the experiment at the site.

The Milagrito detector was operating about 79.5% of the available time during the 15 months it operated. Most of the downtime was attributed to power outages ($\sim$11.5%), calibration($\sim$3%) and scheduled maintenance and construction($\sim$3%).

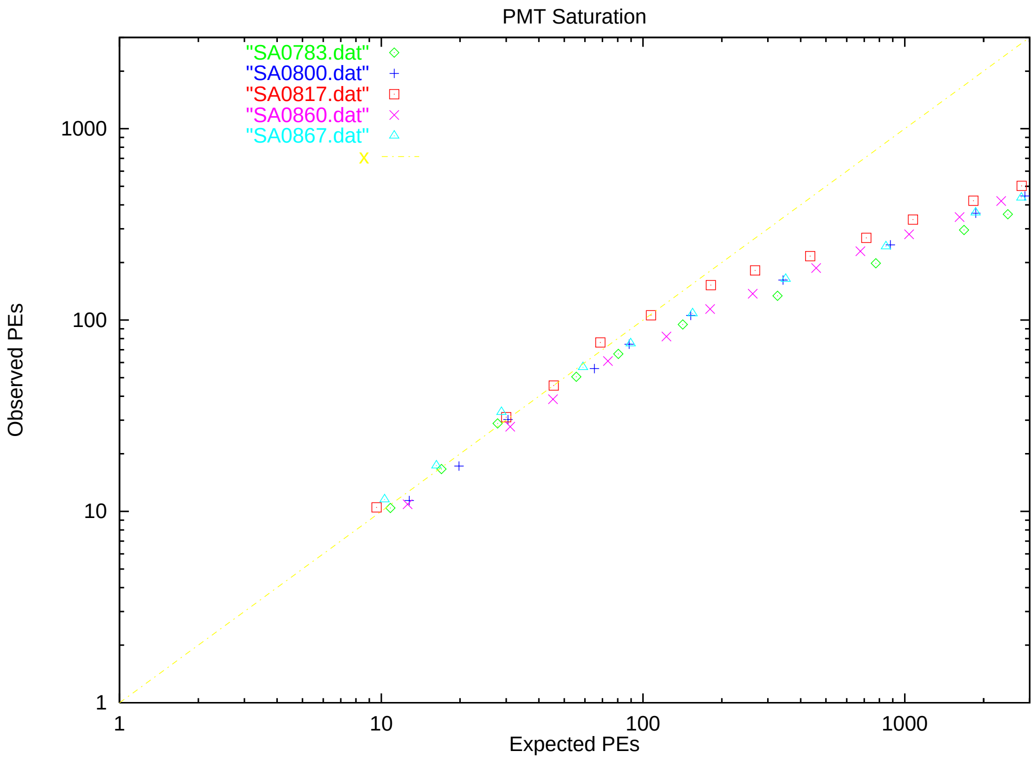

Figure 2.4: Typical linearity of PEs for several PMTs.

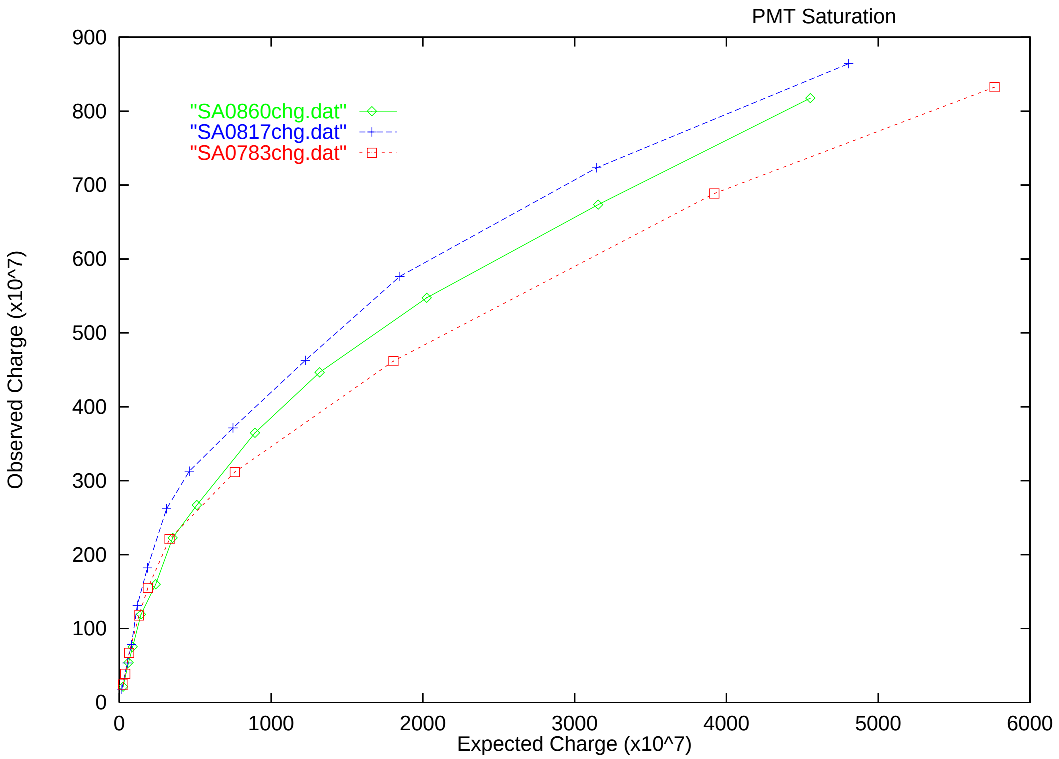

Figure 2.5: Typical gain for several PMTs.

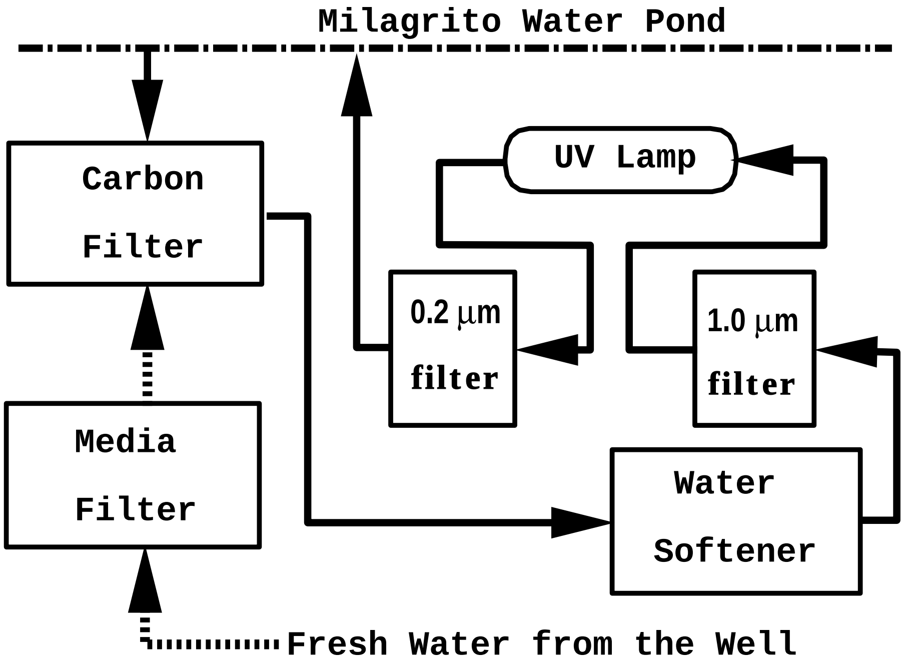

Figure 2.6: The water filtration and recirculation system of Milagrito. The spot arrows stand for the water outside the recirculation, and the solid arrows stand for the water inside the recirculation.

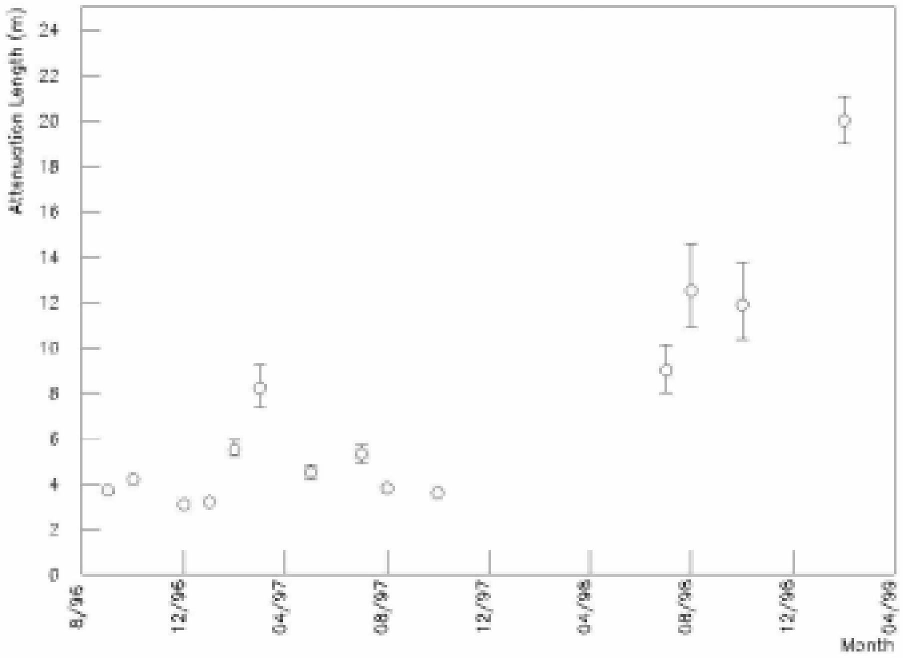

Figure 2.7: Attenuation length of water in Milagrito at 337 nm wavelength. Note: the information for Milagrito is before 12/97, and the information for Milagro is after 04/98. The water in Milago is cleaner than that in Milagrito, and this was because the water in Milagrito is much “softer”.

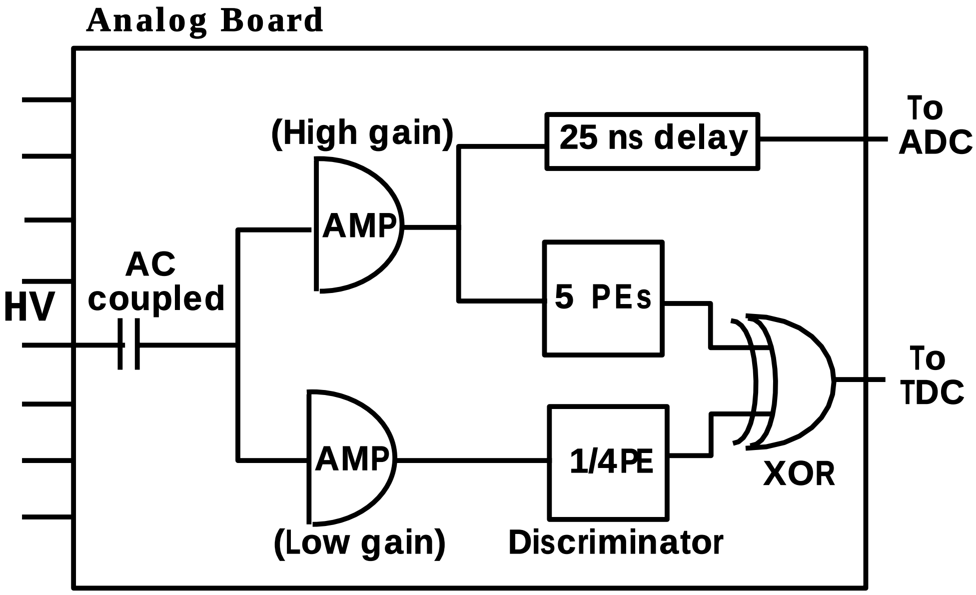

Figure 2.8: Conceptual figure of “analog board”.

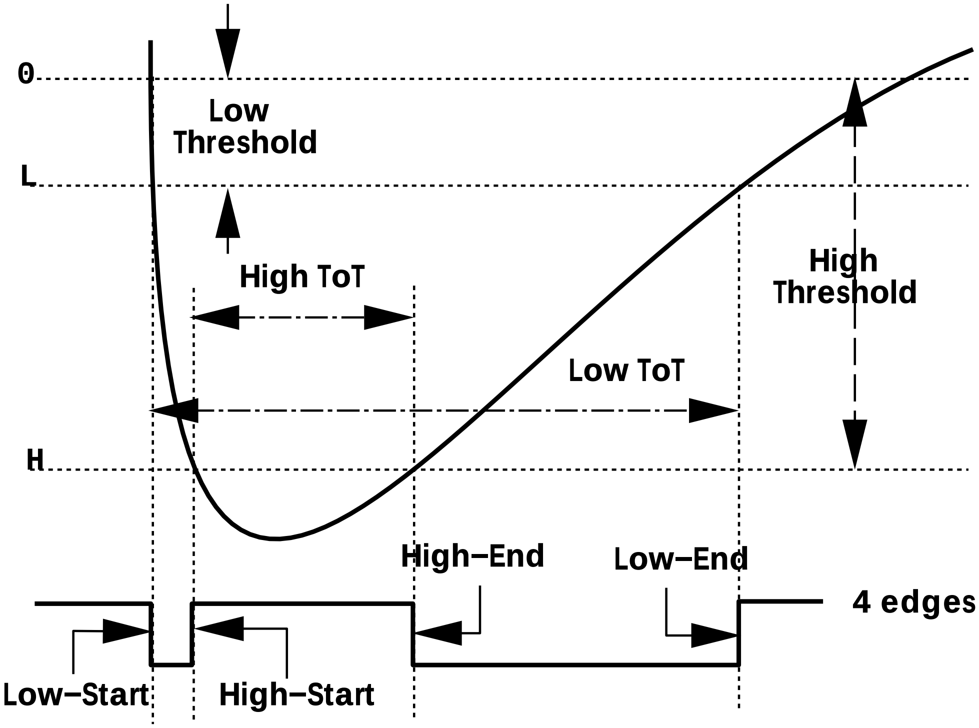

Figure 2.9: Time over Threshold (ToT). A low ToT is created if a pulse height exceeds the threshold of the low-threshold discriminator. A high ToT is created is a pulse height exceeds the threshold of the high-threshold discriminator. The edges for the low-ToT are low-start, low-end, respectively; the edges for the high-ToT are high-start, high-end, respectively. The pulse in the figure forms a 4-edge event since it passes both the low-threshold discriminator and the high-threshold discriminator.

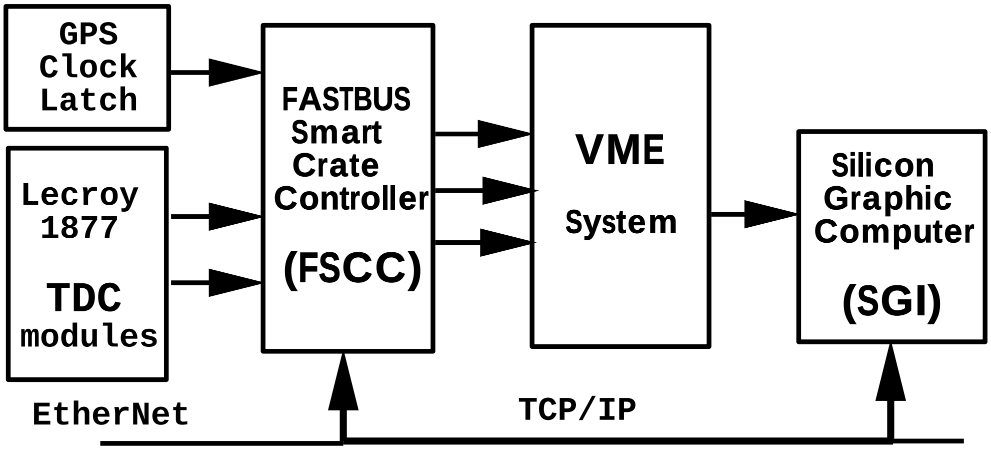

Figure 2.10: Conceptual figure of DAQ

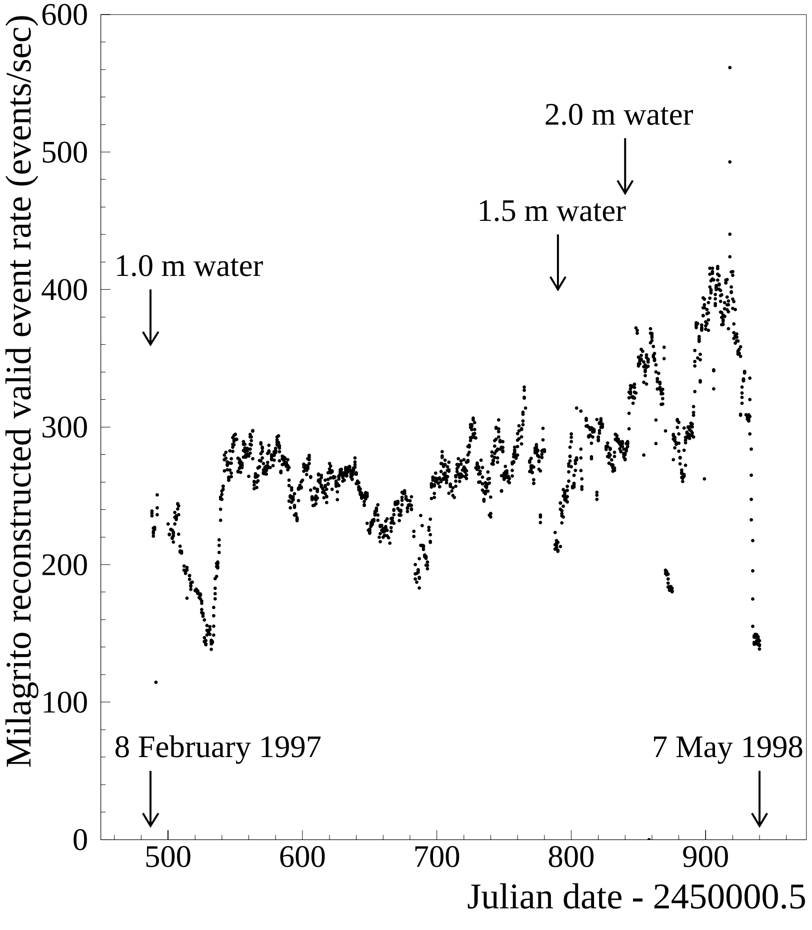

Figure 2.11: Trigger rate for Milagrito

Chapter 3

Reconstruction Of EAS

The goal of the reconstruction program is to determine the direction of the extensive air shower (EAS). The reconstruction of an EAS from the PMT hit information involves a series of steps: the calibration of detector, correction of the arrival time of each PMT hit due to the pulse height, sampling and shower curvature, and the determination of the direction of the shower.

3.1 Direction Reconstruction

When an EAS triggers the detector, the relative time information will be generated by each triggered PMT (Figure 1.3). Once the time information is determined, the direction of the EAS can be reconstructed with the real-time reconstruction method.

In principle, the ideal reconstruction method is the maximum likelihood technique when fitting data with non-Gaussian error distributions. However, maximum likelihood computations take appreciably large amounts of computer time, which is a precious commodity in real time data processing. The angle fitter used for online Milagrito data reconstruction is a simple χ^2 minimization over the arrival time of the shower plane.

$$\chi^2 = \sum_{i=1}^{NHIT} w_i(t_i - t_0 + x_i\hat{\imath} + y_i\hat{\jmath} + z_i\hat{k})^2 \tag{3.1}$$

in which x_i, y_i, z_i are the position coordinates of the i^{th} PMT, t_i is the corresponding time. *NHIT* is total number of PMTs involved in the event, w_i is a function of the intrinsic width of the shower front (which depends on core distance), and the measurement of the pulse height. i.e. w_i stands for the sampling correction in the formula. Minimization of χ^2 with respect to the corresponding time $\mathrm{t_i}$ results in the following equation:

$$t_0 = \frac{1}{W}(T + X\hat{\imath} + Y\hat{\jmath} + Z\hat{k}) \tag{3.2}$$

where,

$$W = \sum_{i=1}^{NHIT} w_i \tag{3.3}$$

$$T = \sum_{i=1}^{NHIT} w_i t_i \tag{3.4}$$

$$X = \sum_{i=1}^{NHIT} w_i x_i \tag{3.5}$$

$$Y = \sum_{i=1}^{NHIT} w_i y_i \tag{3.6}$$

$$Z = \sum_{i=1}^{NHit} w_i z_i \tag{3.7}$$

To minimize the number of iterations associated with the χ^2 fitting, good initial values of $\mathrm{t_i}$ should be selected. When the χ^2 reaches its minimum in the iteration of computing χ^2 and t_0, the iteration will stop therefore the reconstruction for the EAS is completed. The final value of t_0 is used to determine the shower direction. If the χ^2 cannot converge to a minimum, the reconstruction fails.

Only PMTs with measured pulses larger than 2 Photoelectrons (PEs) are used in the fit, since pulses less than 2 PEs are mostly late hits (Figure 3.1). Late hits are mostly the reflected Cherekov light from the bottom of the pond, which has small light density (less than 2 PEs) and hit the PMTs a little later (several ns to more than 50 ns). This 2-PE-cut also significantly reduces the non-Gaussian behavior of the data (Section 4.2).

By applying the χ^2 minimization technique, 92% of the events were successfully fit. The remaining 8% of triggered events, which failed the χ^2 fitting, are most likely associated with single muons passing through the detector at nearly horizontal angles.

3.2 Curvature Correction

The shower front is not a plane, instead, it has a curvature (Figure 3.2). Although no strong evidence for curvature was found in the real data, the Monte Carlo studies indicated that the angular resolution improves if a fixed pulse-height-independent curvature of 4 ns/100 meters is applied. The time information of each PMT used in the direction reconstruction should be corrected for the curvature of the shower front before being used.

As shown in Figure 3.2, the curvature starts at the core position of the shower front, thus to apply the curvature correction, the core position of the shower must be well determined.

3.3 Core Position

The core position of an EAS is the position that the primary high energy particle would hit the pond if no EAS develops. Since an incorrectly determined core position in an EAS will make the whole curvature correction wrong, locating the core of an EAS is a very important part of the shower reconstruction.

Many methods have been used to determine the core position of an EAS, such as the 2-dimensional Gaussian, fast Fourier tranformation (FFT), the gradient convergence, etc. Fitting locaters which use iteration algorithm consume much more CPU time than other locaters without significantly improving the precision of the core position. Since online processing must be fast, Milagrito used a “center of weight” method, which calculates the center of weight of PEs that the PMTs detected.

According to the Monte Carlo, of all the showers that trigger the detector, $\sim 80\%$ have their cores outside the pond, and we have no knowledge where their core positions are. The reasons are that Milagrito is smaller than the lateral size of a TeV shower, and the relatively thin water layer above the PMTs leads to large fluctuations in the observed pulse heights. This results in the big uncertainty of the core position.

A very effective option to reduce the uncertainty of the core position is to use a big *NHIT* in calculating the core. *NHIT*, which means "number of hit", is the number of PMTs triggered by an EAS. In Milagrito, a *NHIT* of 90$\sim$100 PMTs was used. The bigger the *NHIT* is required, the more information of an EAS is collected, thus the less uncertainty the core position would be.

3.4 Sampling Correction

Other than curvature, the shower front of an EAS also has a thickness, which is thinner around the core position and thicker on the edge of a shower. (Figure 3.3). The thickness of the shower front is due to the lower energy particles in the shower, as they were scattered more than higher energy particles in the atmosphere.

The arrival time of the shower that each PMT measured is the time of the first particle that triggers it, not necessarily the particle at the front edge of the shower.

For an EAS, the sampling correction is relatively smaller around the core position, where each PMT collects more photons, and bigger in the lateral positions away from the core, where each PMT collects fewer photons. For a given PMT, the sampling correction is a function of pulse height (Figure 3.4) according to the Monte Carlo.

3.5 Calibration For Milagrito

The reconstruction of EAS' requires many calibration constants for the detector.The electronic devices should response at exactly the same time for various size of pulses; the ToTs from each PMT channel should be converted into PEs because the core postiton is calculated from the PEs that each PMT measured, and also there are 2-PE-cuts applied to each triggered PMT in the direction reconstruction.

The calibration for Milagrito requires the parameters of the following parts: offsets of the PMT time, ToT-PE conversion and slewing correction.

3.5.1 Slewing Correction

The term slewing is used to describe the time variation when the discriminator triggers for pulses that arrive at the same time with different pulse heights. Suppose there are 2 pulses arriving into 2 identical discriminators of the same threshold at exactly the same moment. The bigger pulse always reaches the threshold earlier than the smaller one. The time difference between those 2 start-edges of ToTs is the relative slewing time (Figure 3.6). Slewing correction enables us to obtain the uniform timing information independent of pulse height.

To calibrate the slewing time of each PMT, a system of a setup of a pulsed Nitrogen-dye laser with laser balls is used. The laser pulses are conducted to the water pond with a fiber cable, and at the end of the cable a glass ball was installed in order to have diffusive emission of lights.

The laser pulses can simulate the water-Cerenkov light in the pond. A filter wheel with 21 filters of different optical thickness, was put in the path of the laser to adjust the intensity of light. A splitter is put in the path of the laser light, separating the laser into 2 parts: the transmitted part is used to fire the laser-ball, the reflected part is to trigger the DAQ via a photodiode. To calibrate all the PMTs, 9 laser-balls were distributed in the pond, and only one laser-ball was fired each time in the calibration (Figure 3.5).

The task of slewing correction is to measure both the low-start (of the low ToT) and the high-start (of the high ToT) as a function of the pulse height, i.e. the width of the ToT.

Since each PMT channel has both low-start slewing and high-start slewing, for a given pulse what is the choice of using those 2 slewings? To answer this question we have to study the pre-pulsing behavior of the PMTs.

All the PMTs have some pre-pulsing behavior which influences the low-start time. Pre-pulsing most likely happens when strong light hits the PMT photocathode. The PEs normally go through the dynodes in order, however, some scondary electrons might skip one of the dynodes and go directly to the next stage of dynode. This results in a small pulse coming a few ns before the big pulse comes, which makes the low-start early.

High-start slewing is not influenced by pre-pulsing, so using the high-start slewing whenever it is possible is always the first choice. Figure 3.7 is a sample plot of 4 PMTs for low ToT slewing, and Figure 3.8, for high ToT slewing.

3.5.2 Time-offset Of PMT Response

Each PMT has a specific working High Voltage (HV), in order to reach a gain of $\sim 10^7$ (Section 2.1.3). Because of this, the response times of PMTs for the same incident light are different. To correctly measure a shower front and its direction, all PMTs must be synchronized, i.e. one should subtract the "time-offset of" each PMT from the start-edge of its ToT.

To find the time-offset of each PMT, we used the same laser-ball setup which was used in the slewing correction, with the filter wheel position set to "transparent". The idea is to measure the travel time difference of lights from two laserballs to the same PMT.

Basically, 2 parameters are needed to determine the time offset: The position of the laser-ball, and the travel time of light in water. However, several problems need to be taken care of. The known position of the laser-balls in the water were nominal. Each laser-ball was tied to a PVC pipe with a string, and the strings were longer than the depth of water so that the laser-balls may float on the surface of the water. Because of this, the laser-balls can drift inside a circle of radius up to 1.6m due to the motion of water. Some drifted even further because the ties to the cables were even looser. In addition, one should use the group velocity of light in the water, instead of c/n, because a laser pulse has a spectrum of frequenies.

It is convenient to find the positions of a pair of laser-balls together by looking at time differences of the lights from 2 laser-balls to the same PMT. These time differences are independent of PMTs' time offset. Define:

$$\tau = T_1(x_1, y_1) - T_2(x_2, y_2) \tag{3.8}$$

in which $\mathrm{T}_1, \mathrm{T}_2$ are the travel times of light from laser-ball #1 (x_1, y_1), #2 (x_2, y_2) to the same PMT, respectively. Suppose the PMT's position is (x_i, y_i), and the difference in relative propagation time between optical fibers is T_{fiber}, the above equation changes into:

$$\tau = \frac{1}{v_g}[\sqrt{(x_1 - x_i)^2 + (y_1 - y_i)^2} - \sqrt{(x_2 - x_i)^2 + (y_2 - y_i)^2}] + T_{fiber} \tag{3.9}$$

In which x_i, y_i are known, τ can be measured. v_g is the unknown group velocity of the light in water. Since there are 6 variables in equation (3.9), one needs to use 6 PMTs to calculate the coordinates of the laser balls.

There were 5 laser-balls of 9 in the pond that worked well, and they were used as 6 groups. Figure 3.9 shows the result of measurements of speed of light in the water. Laserball pairs (0-9) and (5-9) are the 2 pairs with the largest separations. This figure shows that the speed of light in the water is 22.12 ± 0.46 cm/ns (or 11.06 ± 0.23 cm/count, since 1 ns = 2 counts).

With the speed of light set to 22.12 cm/ns, the laser-ball positions were found with fitting errors.

The time offset distribution for all PMT channels of Milagrito is shown in Figure 3.10. The plot shows a peak with a width of ±10 ns.

3.5.3 ToT-PE Conversion

Since Milagrito used the ToT technique to obtain both timing and pulse height information, one needs to convert the ToT into number of PEs for each PMT channel. In the Milagrito experiment, there was only one ADC module in the FASTBUS crates, and this ADC module is only used to determine the ToT-PE conversion.

The task of the ToT-PE conversion is to find the distribution of ADC counts vs low ToT and vs high ToT for each PMT channel, respectively. Since for each PMT channel 1 PE equals to a definite number of ADC counts, ToTs can be converted to PEs using this information.

To determine how many ADC channels equal to 1 PE, or the 1-PE value of each PMT, one needs to study the raw ADC distribution, which typically has 2 peaks: the pedestal and the 1-PE peak. (Figure 3.11).

The pedestal peak is caused by the internal circuit current of the ADC FASTBUS module. There is always some DC current, which is manually set, flowing through the input circuit of an ADC even though the input analog signal is zero. So when a signal comes, the starting point to sample the level of the input signal is the default DC level, which corresponds to a pedestal in the ADC readout.

When weak Cherenkov light hits the photo-cathode of a PMT, it is most probable that the PMT emits only 1 PE in its first-stage cathode, which forms the 1-PE peak in ADC readout. The difference between the pedestal and the 1-PE peak is the 1-PE value for the PMT channel.

The distributions of ADC vs ToT (both low and high ToT) for each PMT channel are obtained by using the 1-PE values. The function used to relate those 2 distributions is:

$$F(x) = P1 \times log(P2 \times x) + P3 \tag{3.10}$$

in which $F(x)$ stands for the ADC channels, and x stands for the ToT (PEs).

Figure 3.12 and Figure 3.13 show a typical distribution of ADC vs low ToT and high ToT, respectively. The low ToTs start from 0 and saturate at ~7 PEs, whereas the high ToT start from ~5 PEs. *P1*, *P2* and *P3* are fitting parameters.

For the overlap region (5~7 PEs), there are 2 groups of fitting parameters. The study of the RMS of ADC distribution at this region was performed, for both low ToT and high ToT. The result shows that using high ToT will introduce much less uncertainty than using the low ToT. Therefore high ToT is always used whenever it is available.

Comparing the fitting result to the data yields an error of $\leq$5-10% for all the PMT channels.

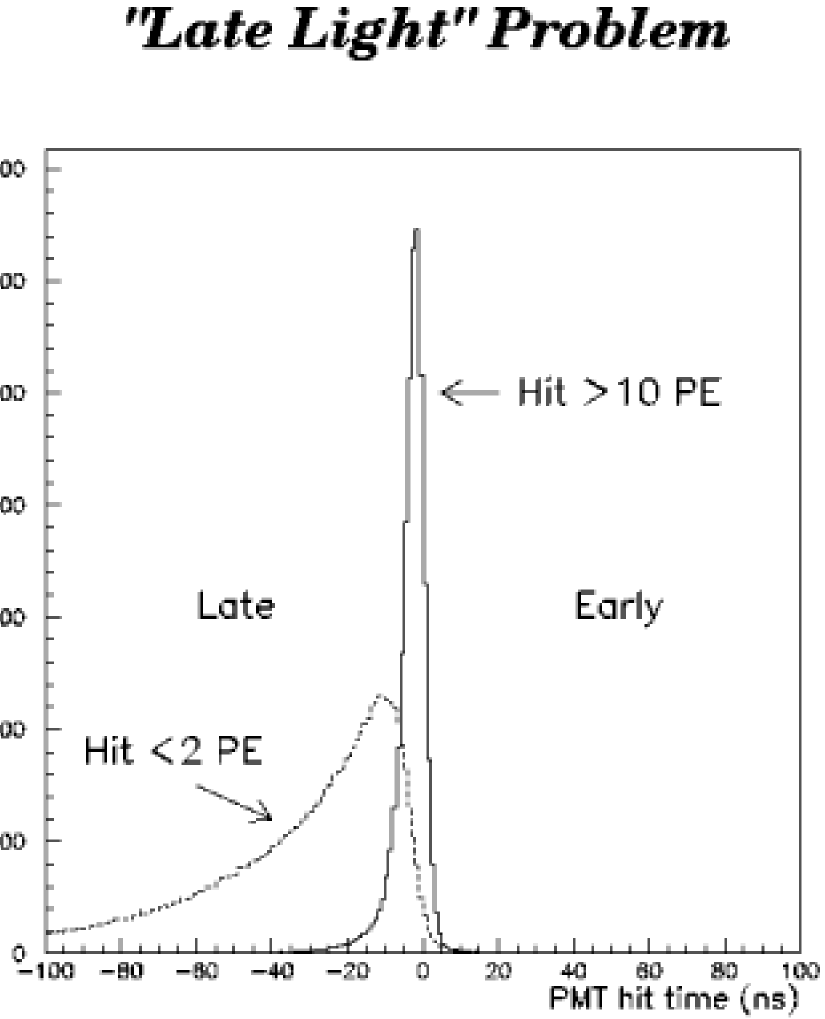

Figure 3.1: The late hits for Milagrito events. Note the "0" stands for the starting time that an EAS triggered the detector.

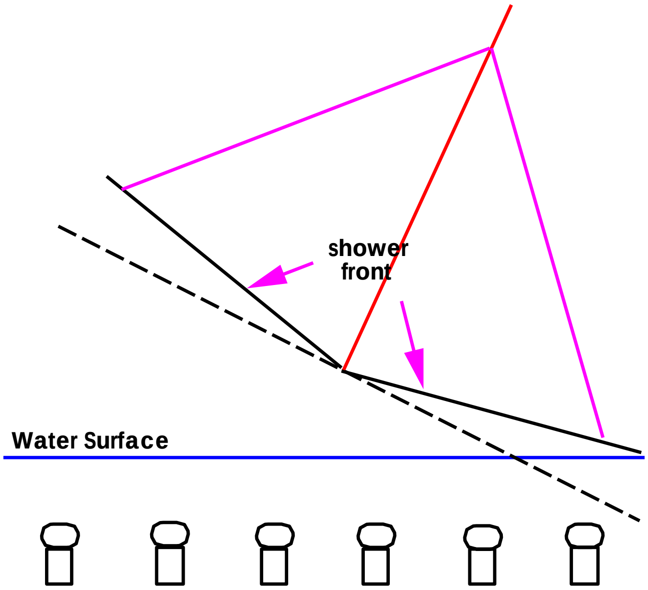

Figure 3.2: Curvature correction.

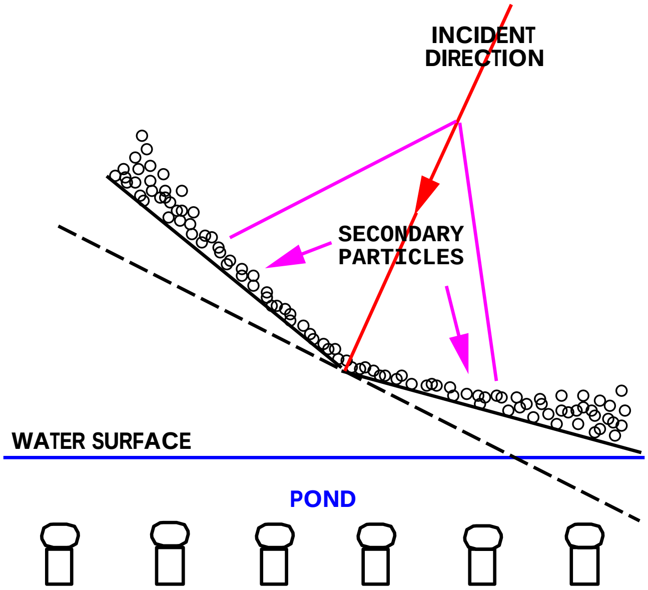

Figure 3.3: Sampling correction.

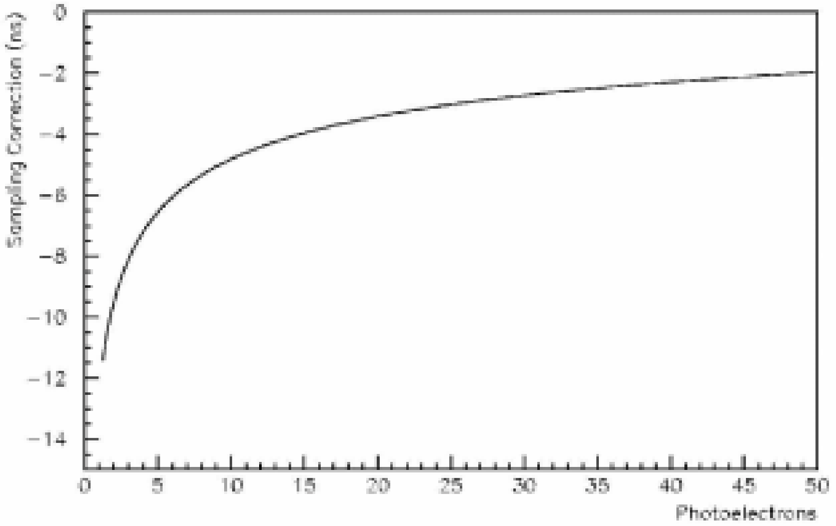

Figure 3.4: The sampling correction as a function of the pulse height in a PMT (Monte Carlo data).

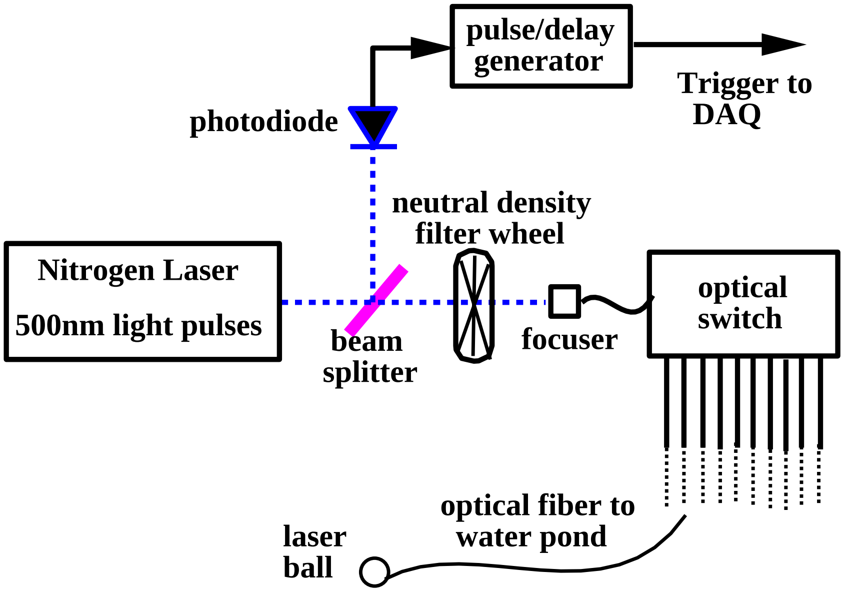

Figure 3.5: Setup of Laser.

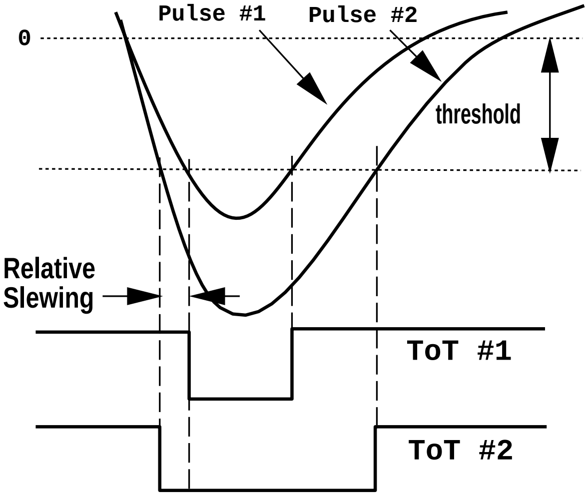

Figure 3.6: Slewing Correction.

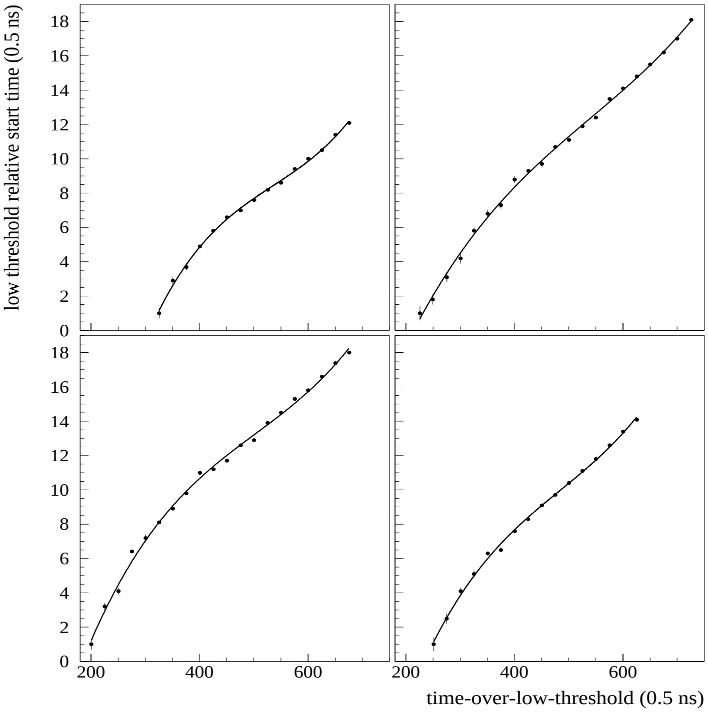

Figure 3.7: Sample low ToT slewing curves of four PMTs. The dots are data using laser light, the lines are fitted polynomials. To make the y-axis uniform for the four plots, the low start for each curve was shifted by an amount such that the four curves started at the same point on the y-axis.

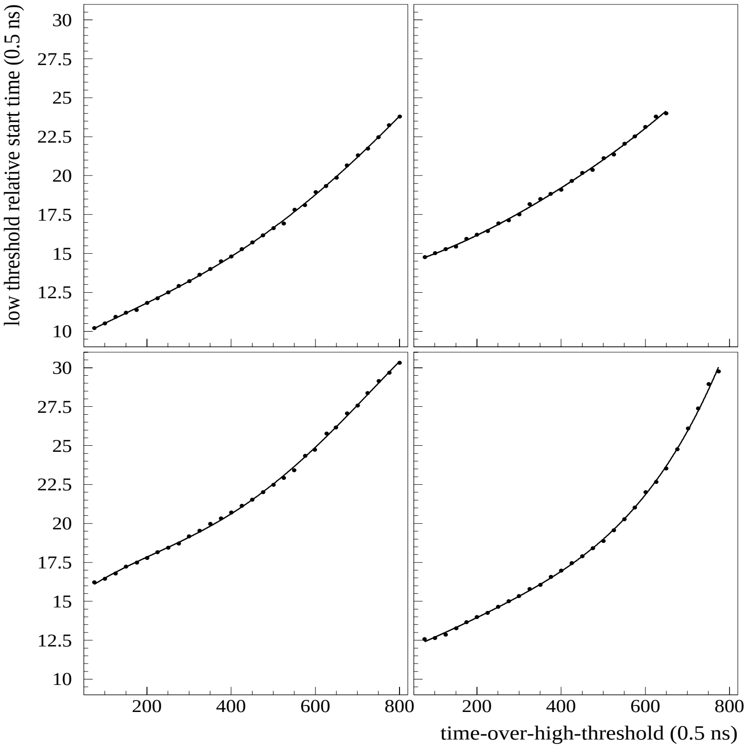

Figure 3.8: Sample high ToT slewing curves of four PMTs. The dots are data using laser light, the lines are fitted polynomials. The y-axis is an extension of the y-axis of the low tot slewing curves.

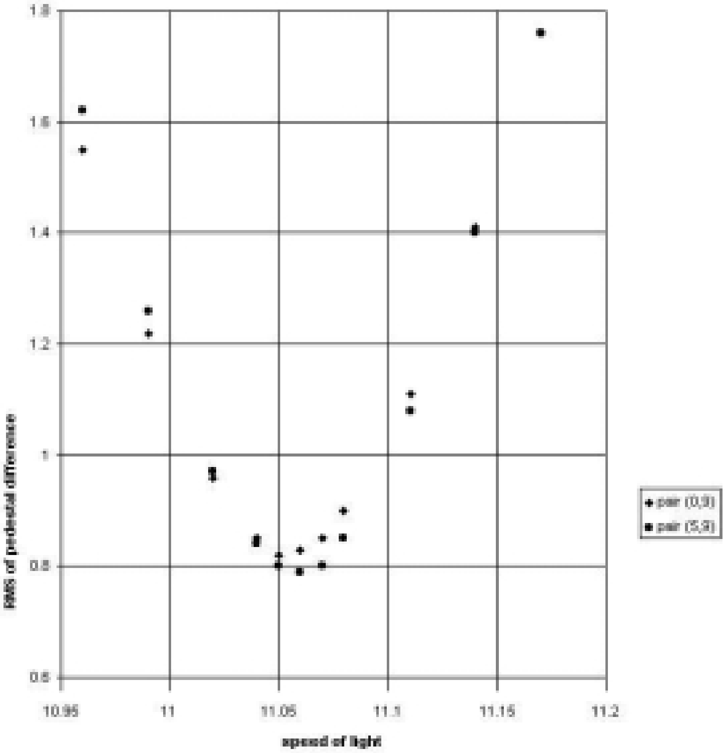

Figure 3.9: RMS of time-offset difference vs measurement of speed of light. The x-axis is the speed of light (cm/counts), the y-axis is the RMS of time-offset difference (count). The diamonds are the result for laserball pair (0-9), and the circles are for laserball pair (5-9).

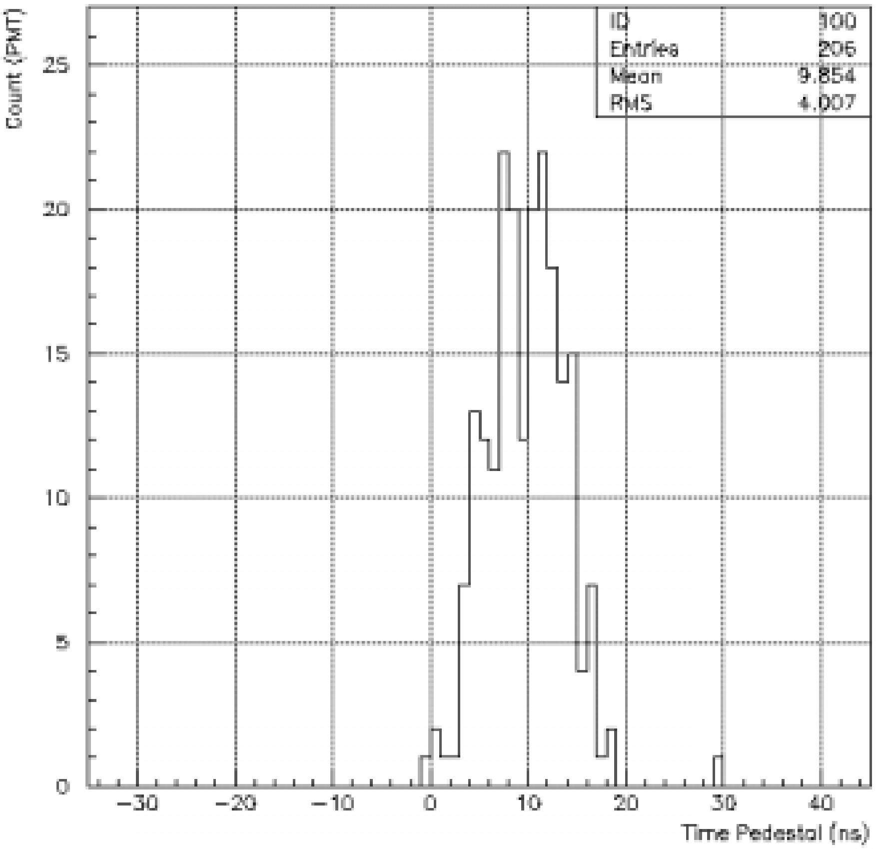

Figure 3.10: Time offset distribution.

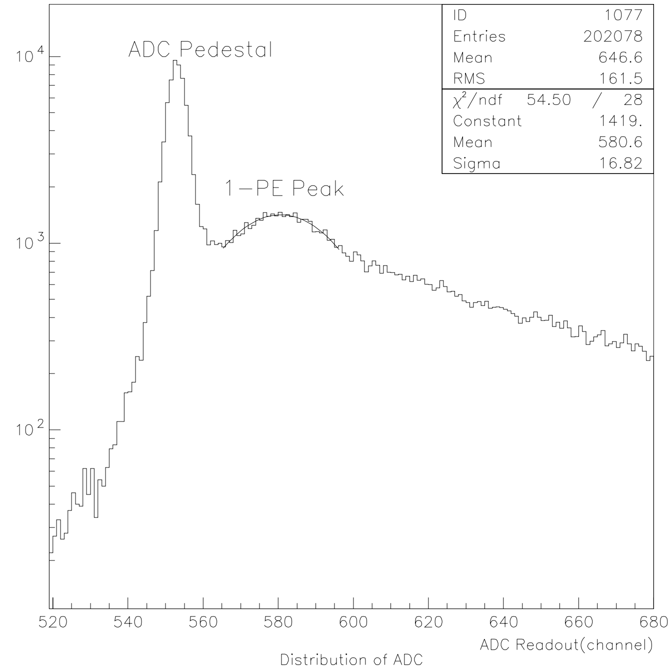

Figure 3.11: Pedestal and 1-PE peaks from ADC readout

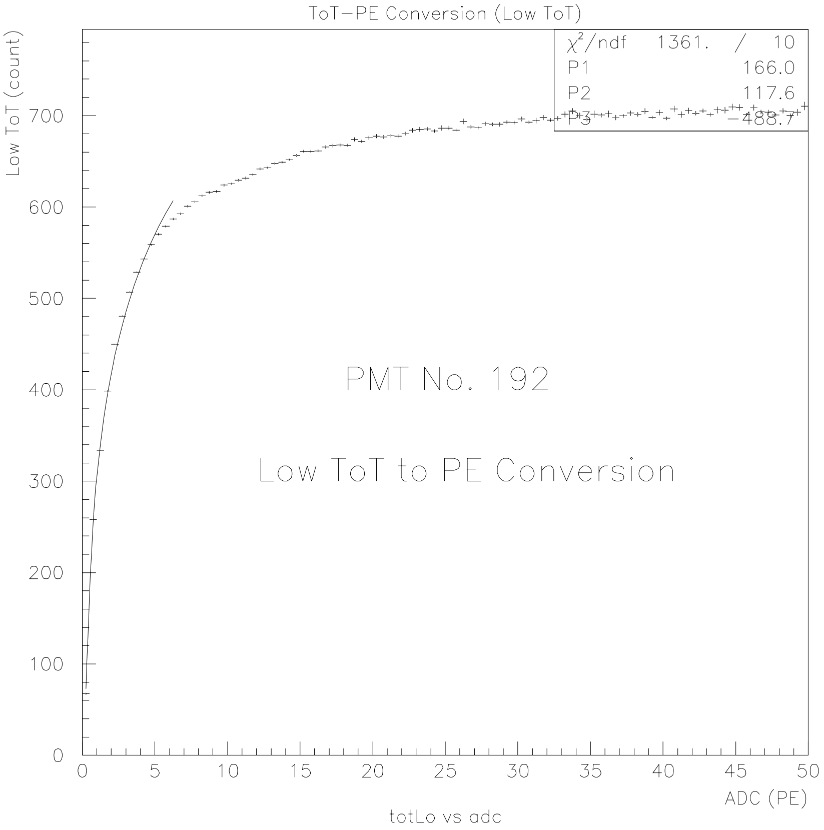

Figure 3.12: Typical distribution of Low ToT vs ADC. The horizontal coordinate is ADC(channel), and the vertical coordinate is Low ToT(count). Low ToT is fully saturated after ADC∼700 channels (Note: 1 count of ToT = 0.5 ns).

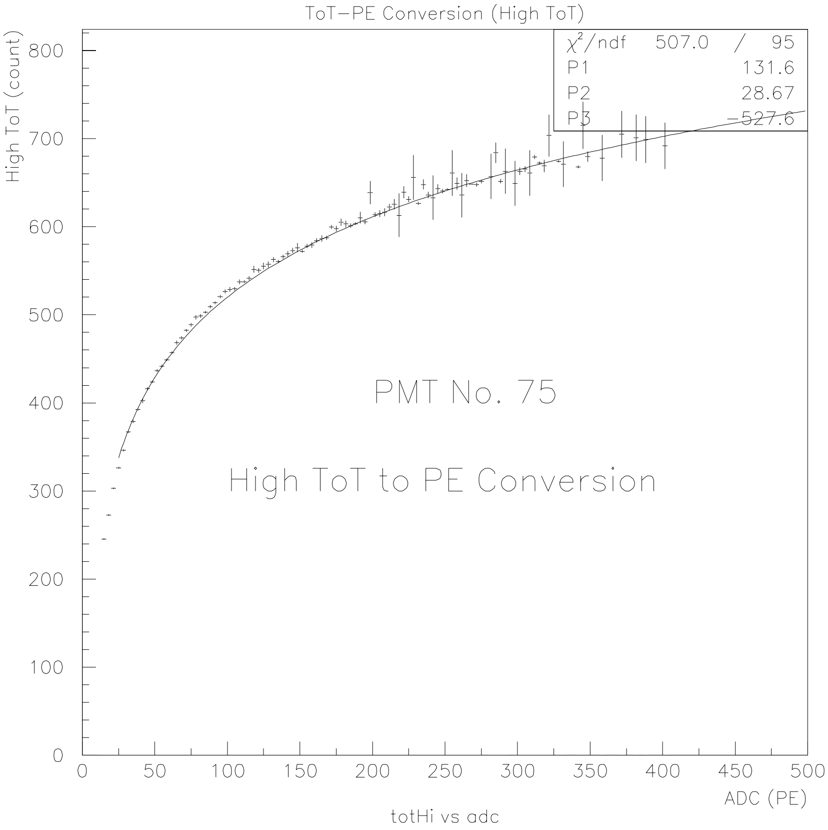

Figure 3.13: Typical distribution of High ToT vs ADC. The horizontal coordinate is ADC(channel), and the vertical coordinate is High ToT(count). There is no event for High ToT less than 50 counts (Note: 1 count of ToT = 0.5 ns).

Chapter 4

Milagrito Simulations

The performance of Milagrito has been studied with Monte Carlo simulation. Ideally, the results of the Monte Carlo simulation are compared with real data from a well-known and steady source used as a standard candle, such as the Crab Nebula. Unfortunately, the data sample obtained with Milagrito does not have enough sensitivity in detecting the emission of the Crab Nebula for a meaningful confirmation of the Monte Carlo simulation of Milagrito. Consequently, we have to rely on the basic detector performance to verify the Monte Carlo simulation.

The Monte Carlo simulation for Milagrito includes 2 parts: generation of the air showers and the detector response. The simulation package used to generate air showers is the CORSIKA package [30][31], developed by Kaskade group in Heidelbag. The simulation of the detector response is based on the GEANT package [32], developed by CERN.

4.1 Monte Carlo Simulation Of Air Showers

In section 1.3, the processes of EAS development were described. For a primary particle, photon or proton, of a specific energy and direction, the Monte Carlo simulation follows its interaction with the atmosphere, and subsequently the decays, collision and interactions of all the secondaries, according to properties of each type of particle and the known interaction cross sections. The full sequences of decays, collisions and interactions are followed until the particles either stop or reach the ground. The kinematical information of the shower particles are used as input for the detector response simulation.

The flux of cosmic ray protons falls off rapidly as a function of energy, commonly described by a power-law, $E^{-2.7}$ (Equ. (1.2)). Similarly, the flux of γ-ray photons is described by a power-law $E^{-2.4}$ (Equ. (1.2)). In the Monte Carlo simulation, primary particles are generated according to these power-law spectra. In practice, events are generated according to the energy distribution. Although lower energy particles, for example, ~10 GeV, have higher flux, they will die out in the atmosphere before reaching the ground. Particles of energy less than 100 GeV cannot reach the ground, so the energy range of the primary particles in the simulation is chosen from 100 GeV to 100 TeV.

In order to trigger the detector effectively, showers are generated with cores over a region 500m×500m centered on the pond. This region is large enough that includes all possible showers that can trigger the detector, and showers thrown outside this

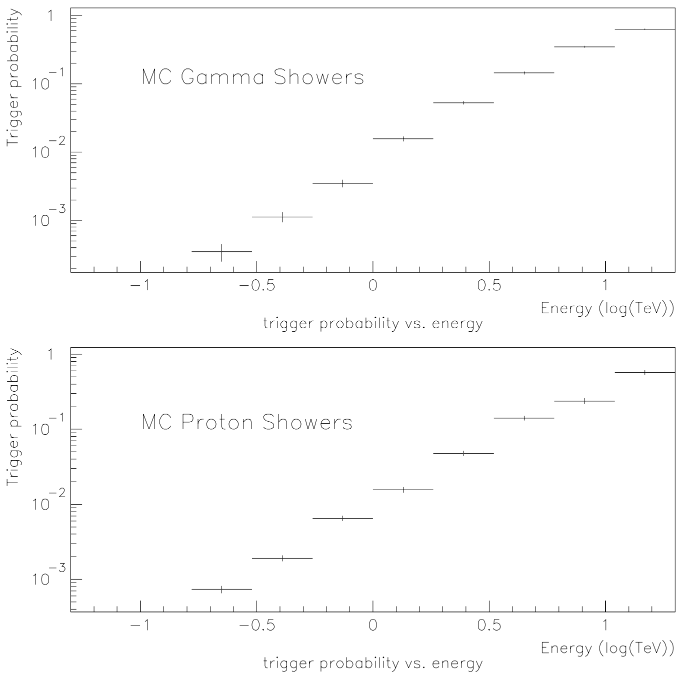

Figure 4.1: Total trigger probability ($\theta \leq 45°$) as a function of energy for Monte Carlo γ showers and proton showers. The γ showers has larger trigger probability than proton showers at higher energy (E $\sim$ 10 TeV), and has smaller trigger probabilty than proton showers at lower energy (E $\sim$ 200 GeV).

region are too far away from the pond that will not trigger the detector.

Showers come from all directions. However, showers of very large zenith angle ($\theta > 45°$) will rarely trigger the detector, because the atmosphere is effectively thicker from these showers' angle of view therefore they will die out in the atmosphere before reaching the detector. The incident directions that are thrown from $0° \sim 45°$ in θ (zenith angle) and $0° \sim 360°$ in ϕ (azimuthal angle).

The output of the air shower simulation, which includes the information of the secondary particles, such as the energies, directions, arrival times to the pond and the positions in the pond, is used as the input of the detector response simulation.

4.2 Monte Carlo Simulation Of Detector Response

The PMT positions and the water depth in the pond are included in the detector simulation. We assumed a 20-m optical scattering length in water and a complete internal reflection at the bottom of the pond with a 5% reflectivity.

The air shower information is read and the directions and densities of Cerenkov light are calculated. If the Cerenkov light reaches a PMT before it is absorbed by water, that PMT is triggered. The relative arrival time of the shower for the triggered PMT is calcuated, and so is the number of PEs.

The simulation data includes the positions of the PMTs that are triggered, the relative arrival time measured by the triggered PMTs, the pulse height (PEs) measured by the triggered PMTs, the incident direction (θ, ϕ), the energy and the particle type of the primary particle. Figure 4.1 shows the total trigger probability ($\theta \leq 45°$ and $0°$-$360°$ for ϕ), as a function of energy for Monte Carlo γ showers and proton showers. Of more than 150 million photons and protons thrown, $\sim$2% triggered more than 1 PMT and $\sim 9\times10^{-5}$ triggered more than 90 PMTs. Of all the showers that trigger the pond, only 21% of the γ-showers and 16% of the proton showers have their cores in the pond.

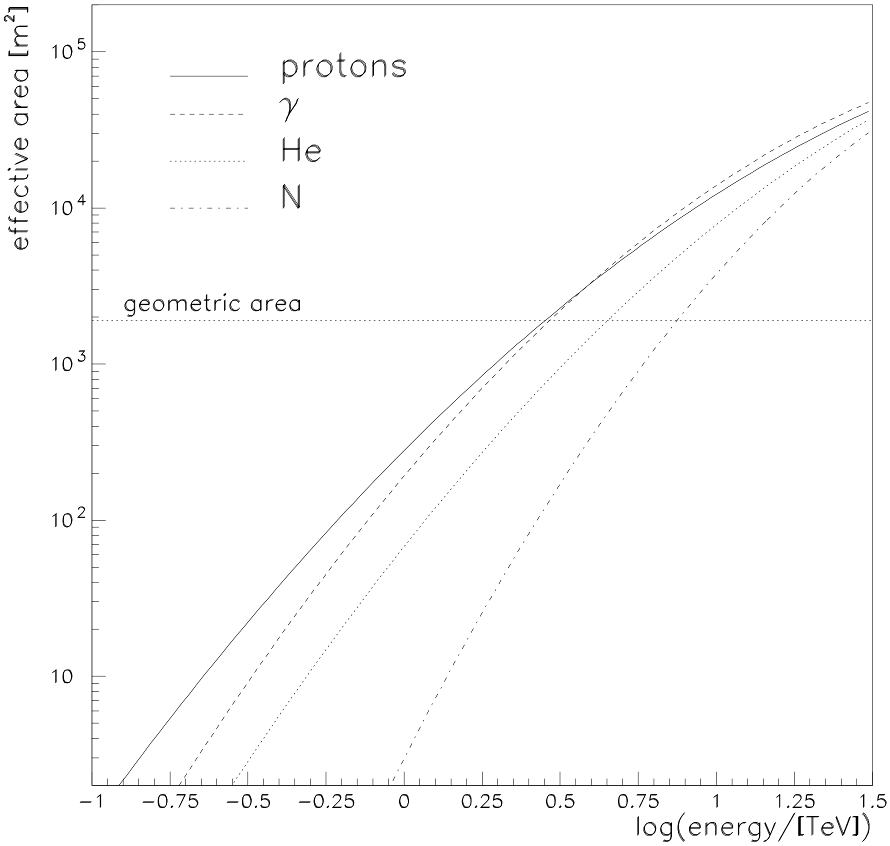

Figure 4.2: Effective area of Milagrito for different primary particles vs primary energy.

4.3 Sensitivity Of Milagrito

4.3.1 Effective Area

Suppose a large number of simulated EAS' (N_{total}) of energy E were thrown in a sufficiently big area A_{thr} at a zenith angle θ, and there are N_{trig} showers triggered the detector. The differential effective area $A_{eff}(\theta, E)$ is:

$$A_{eff}(\theta, E) = \frac{N_{trig}}{N_{total}} \times A_{thr} \tag{4.1}$$

The differential effective area tells the trigger sensitivity of the detector. Besides, the total effective area for all E and θ is related to the flux F and the trigger rate R:

$$R = F \times A_{eff}^{tot} \tag{4.2}$$

The differential effective area of Milagrito $A_{\mathit{eff}}(\theta, E)$ for various θ as a function of primary energy E is shown in Figure 4.2. The $A_{\mathit{eff}}(\theta, E)$ for γ showers is the same as the proton showers when E $\sim$ 3 TeV. Below this energy, $A_{\mathit{eff}}(\theta, E)$ for γ showers is smaller that proton showers, and above this energy, $A_{\mathit{eff}}(\theta, E)$ for γ showers is bigger than proton showers. This is because that the proton showers are more clumpy than the γ showers.

The total A_{eff} is larger than the physical area of the pond above $\sim$3 TeV for both γ showers and hadron showers. Since the shower information outside the pond is unknown, the core-locater cannot be further improved. This effect leads to a very broad energy distribution for detected events.

The real Milagrito data has a trigger threshold of 90-100 PMTs. To properly compare the Monte Carlo and the real data, a *NHIT* cut of 90 PMTs is put into the analysis for Monte Carlo events.

4.3.2 Δ-Angle, Δ_{EO} and Angular Resolution

Δ_{EO}, which means “Difference of Even and Odd”, is the difference of the directions reconstructed by even number of PMTs and odd number of PMTs (Figure 4.3). And either the even number of PMTs or the odd number of PMTs covers the whole physical

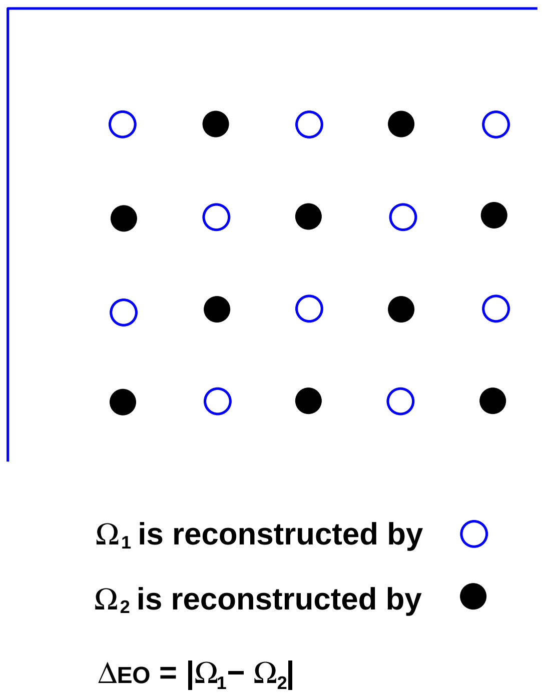

Figure 4.3: Definition of Δ_{EO}.

area of Milagrito. If there is no systematic effect, $\Delta_{\rm EO}$ should the angular resolution. In reality, the angular resolution is always bigger than the $\Delta_{\rm EO}/2$, i.e. the angular resolution is never better than $\Delta_{\rm EO}/2$.

Figure 4.4 is the comparision of $\Delta_{\rm EO}$ for Monte Carlo events (both proton showers and γ showers), and the real Milagrito data, with a *NFIT* cut equals to 30 PMTs. (*NFIT* is the number of PMTs used in the reconstruction of an EAS.) Since nearly all the real events are due to background, in ideal case, the $\Delta_{\rm EO}$ for real data should be very consistent with that of the Monte Carlo proton showers. In Figure 4.4, the MEAN of $\Delta_{\rm EO}$ for real data is larger than the MEAN of $\Delta_{\rm EO}$ for Monte Carlo proton showers. The reason is that real data has a long tail in its $\Delta_{\rm EO}$ distribution, whereas

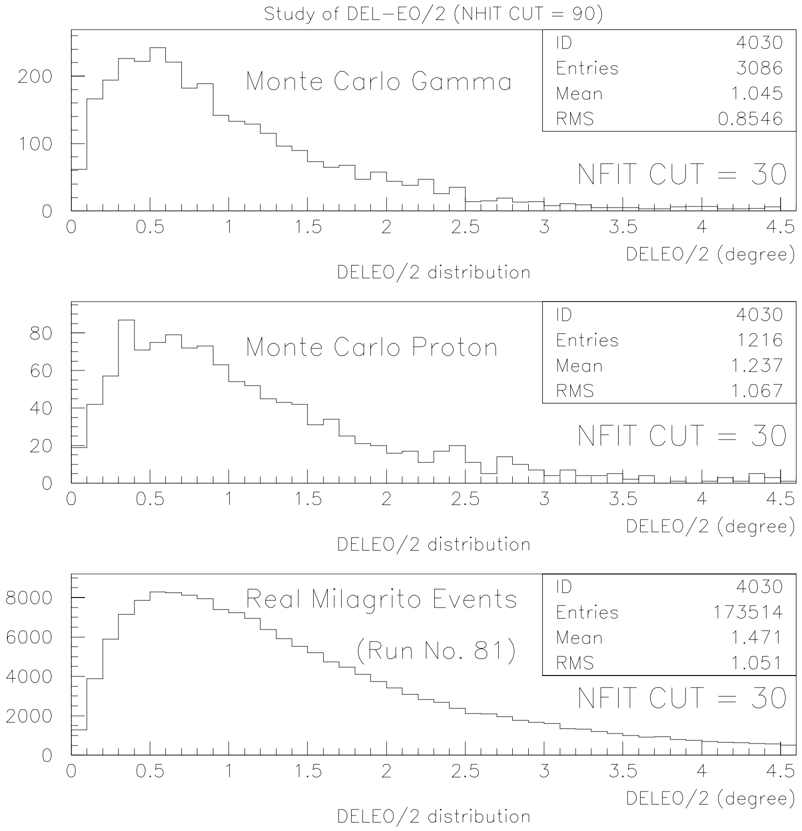

Figure 4.4: Comparision $\Delta_{\rm EO}/2$ of Monte Carlo γ, proton and real Milagrito events for $NFIT \geq 30$ and $NHIT \geq 90$.

the Monte Carlo data does not, and this long tail enlarge the MEAN of $\Delta_{\rm EO}$ for the real data.

To determine the difference of $\Delta_{\rm EO}$ between the Monte Carlo and the real data, the MEAN of $\Delta_{\rm EO}$ under various *NFITs* are studied. Figure 4.5 shows the MEAN of $\Delta_{\rm EO}$ as a function of *NFIT*. For $NFIT \leq 30$, the difference is bigger; for $NFIT \geq 40$, the difference between Monte Carlo proton showers and the real events is an constant.

Δ-Angle is only meaningful in Monte Carlo showers, and it is the difference be-

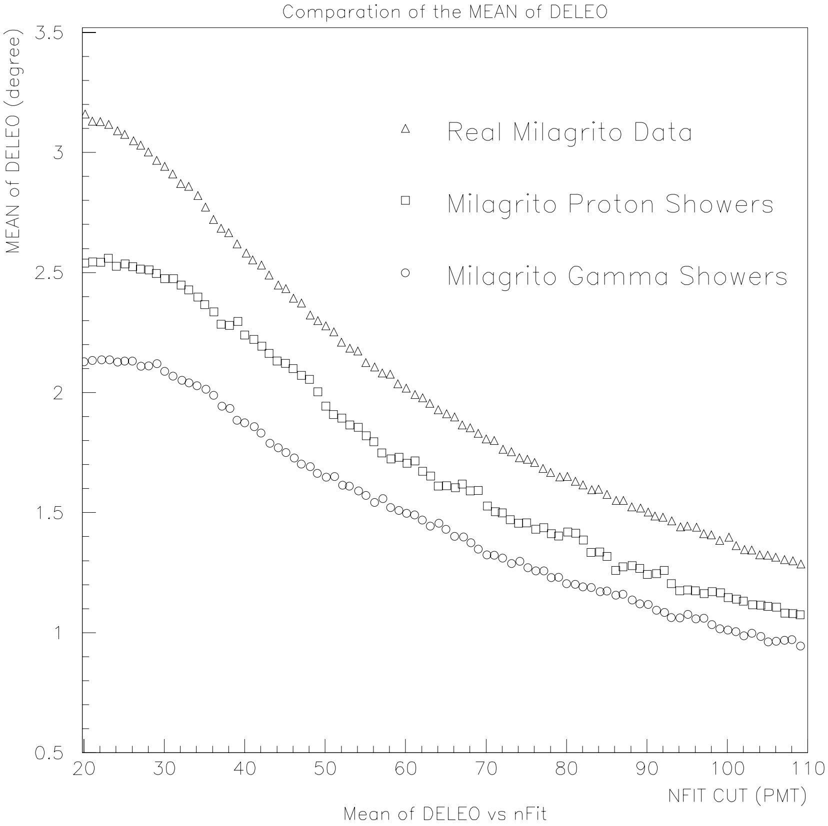

Figure 4.5: Comparision the MEAN of Δ_{EO} of Monte Carlo γ, proton and real Milagrito events

tween the reconstructed direction and the real incident direction of the shower. So Δ-Angle is the angular resolution if the simulation is perfect the same as the real detector. Figure 4.6 is the Δ-Angle distributions of both Monte Carlo proton showers and γ showers, with $NFIT \geq 30$ PMTs. Like in the Δ_{EO} distribution, the distribution for proton showers has a bigger MEAN than that for γ showers.

Generally, the angular resolution tells how well the detector may discriminate 2 nearby sources. The excess of an ideal source is a 2-dimensional Gaussian distribution,

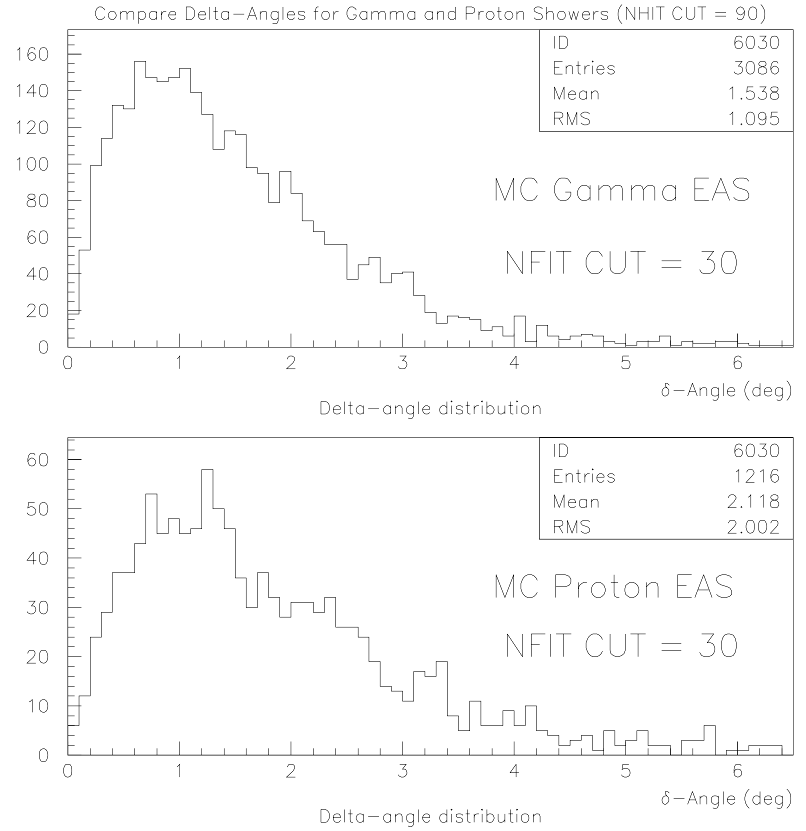

Figure 4.6: Comparision of Δ-Angle of Monte Carlo γ and proton EAS' for $NFIT$=30

of which the width is what is normally called the "angular resolution". So both the Δ_{EO} and the Δ-Angle distribution should have the shape of function $\theta \times \mathrm{G}(\theta)$ ($\mathrm{G}(\theta)$ is an one-dimensional Gaussian distribution as a function of θ), because,

$$< \theta >= \int \theta G(\theta) d\theta \tag{4.3}$$

Figure 4.4 to Figure 4.6 show that the Monte Carlo data obey eqaution (4.3) very well. However, the Δ_{EO} of Milagrito data does not exactly obey equation (4.3), since it has a longer tail than the Monte Carlo data, which causes the MEAN of Δ_{EO} to be larger than the Monte Carlo data. This non-Gaussian effect for the real data results in difficulties for the determination of angular resolution. The reason for the non-Gaussian effect and the algorithm on determining the resolution by using Monte Carlo data are described in Chapter 5.

4.3.3 Trigger Efficiency For Known Sources

For a known source, such as the Crab, if we assume the spectrum measured by some ACT (such as Whipple) is precise, the number of photons that Milagrito can see is given by the following:

$$N_{day} = \int_{E} \int_{Day} \Phi(E) A_{eff}(E, \theta(t)) dE dt \tag{4.4}$$

where $\mathrm{A_{eff}(E, \theta(t))}$ can be determined by the Monte Carlo. $\Phi(E)$ is known, for example, the $\Phi(E)$ for the Crab was given by equation (1.3). To calculate $\mathrm{N_{day}}$, all one needs to do is to simulate a whole source day and integrate the total trigger probability, as the effective area $\mathrm{A_{eff}(E, \theta(t))}$ is given by equation (4.1).

Since the detector has an angular resolution, a source bin should be introduced in the calculation. Thus equation (4.4) becomes:

$$N_{day} = \int_{E} \int_{Day} \int_{bin} R(\theta) \Phi(E) A_{eff}(E, \theta(t)) dE dt \tag{4.5}$$

where $R(\theta)$ is the angular resolution. This can be done by accumulating the trigger probability of a whole source bin while simulating the source day, and then multiplying by an efficiency of 72% since an optimal bin contains 72% of the source events. This is a good approximation even the angular resolution is not a Gaussian.

4.3.4 Effective Trials For Overlapping Bins

In many cases, the source is not located in the center of a chosen source bin. To optimize the source significance, overlapped bins are applied.

A typical optimization is to shift half of the bin size in RA, and half of the bin size in δ, and shift half of the bin bize in both RA and δ, thus 4 group of bins are created. In this optimization, each event in the sky is used 4 times so those 4 group of bins are not independent. The effective trials for a certain significance σ should be larger than 1 because there are more than 1 trial, and less than 4 because those 4 trials are partially dependent. By definition,

$$n_{eff}(\sigma) = \frac{n_{ex}(\sigma)}{n_{tot} \times \rho(\sigma)} \tag{4.6}$$

in which $n_{\mathit{eff}}(\sigma)$ is the effective trial as a function of significance, $n_{ex}(\sigma)$ is the number of bins which have significances larger than σ, n_{tot} is the total number of bins, and $\rho(\sigma)$ is the probability of more than σ significance in a Gaussian distribution:

$$\rho(\sigma) = 1 - \varphi(\sigma) = 1 - \frac{1}{\sqrt{2\pi}} \int_{-\infty}^{\sigma} e^{-\frac{v^2}{2}} dv \tag{4.7}$$

Since the bins which have source excesses appear at the right side of a Gaussian, n_{eff} remains 1 for most low significance ($\leq 3\sigma$).

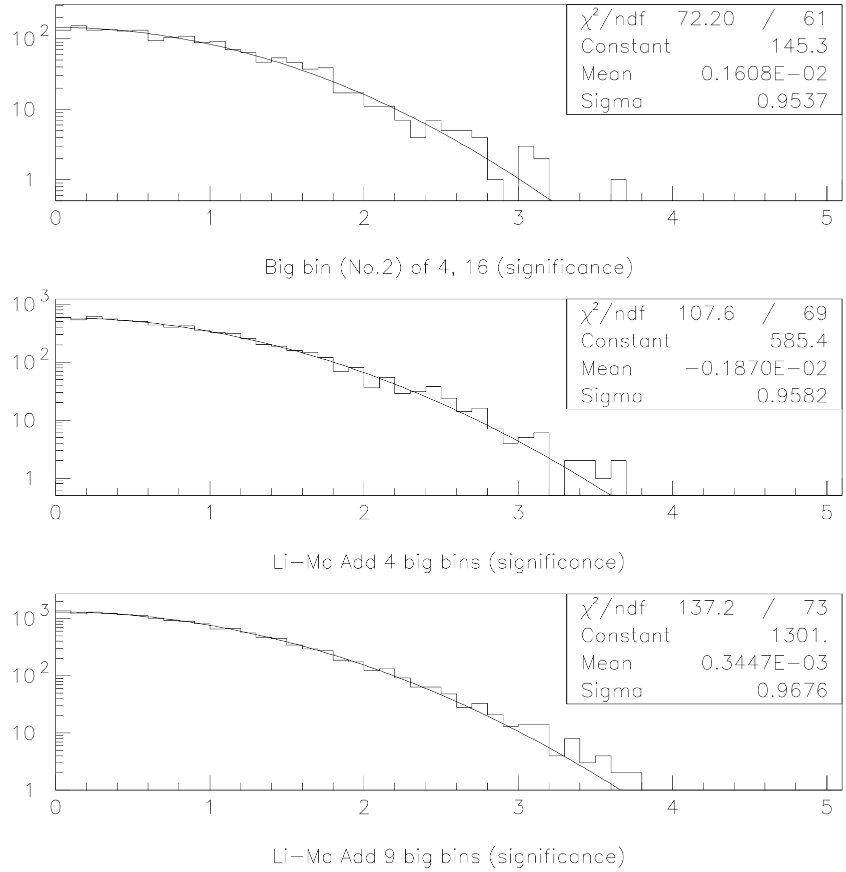

Figure 4.7: Typical significance distributions (Monte Carlo data) for no-overlapping bins (upper plot), 4-overlapping bins (middle plot), 9-overlapping bins (lower plot).

To study the distribution of n_{eff} as a function of significance $\hat{S}$, a Monte Carlo simulation is used. 54 million events were thrown into a simulated sky which has 60×60 source bins. The source bins were shifted 1/3 and 1/2 bin size respectively therefore the optimizations of 9 and 4 overlapped bins can be studied.

For a survey with four groups of overlapping bins, $n_{eff} \sim 1$ when $\hat{S} \leq 3.0\sigma$, and n_{eff} reaches 2.5 when $\hat{S} \sim 3.6\sigma$.

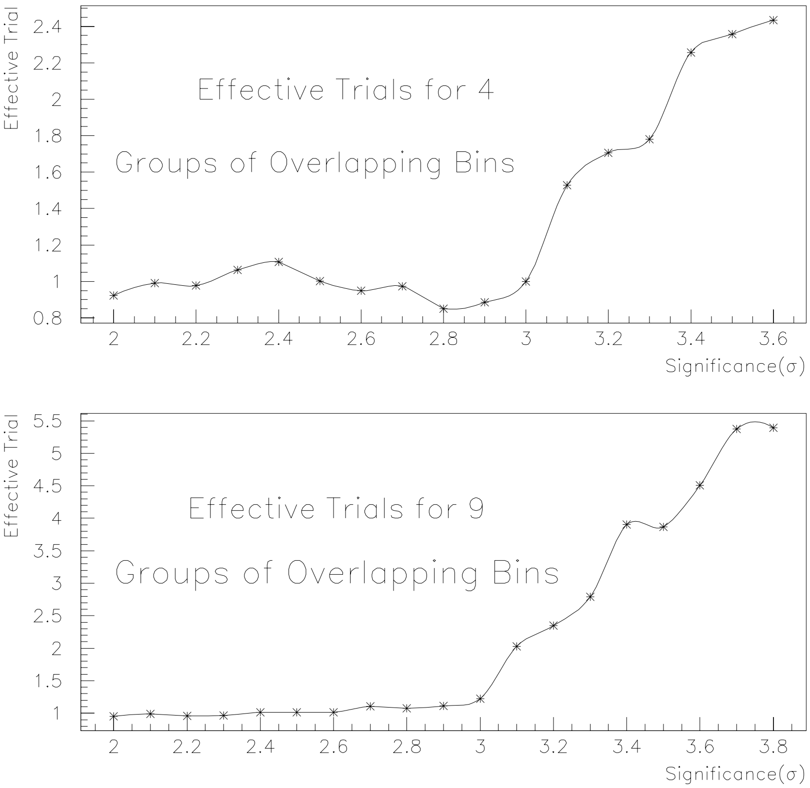

Figure 4.8: Effective trials as a function of significance (σ).

Chapter 5

Analysis Technique

The analysis technique for the all-sky survey combines the optimal bin and the time-sloshing methods. Time-sloshing method is used to generate the background because any signal would be observed in the presence of background. The optimal bin, which maximize the significance of a source, was determined by Monte Carlo result. To properly estimate the significance for time-sloshing method, the Li-Ma estimation was used.

5.1 Optimal Bin Size

5.1.1 Optimal Bin In Ideal Situation

The optimal bin is the bin size that maximizes the source significance. If the bin size is too big, it will include more background events which will weaken the significance. If the bin size is too small, it will exclude some excess, which also weakens the significance.

In an ideal situation, the excess events forms a 2-dimensional Gaussian of width σ, and the background is flat. The number of excess events within a circular bin of radius $r(^\circ)$ is:

$$N_s(r) \propto \int G(r)ds = \frac{1}{2\pi\sigma^2}\int_0^{2\pi} d\phi \int_0^R e^{-\frac{r^2}{2\sigma^2}} r dr = 2(1 - e^{-\frac{r^2}{2\sigma^2}}) \tag{5.1}$$

For a flat background, the significance $\hat{S}(r)$ is:

$$\hat{S}(r) = \frac{N_s(r)}{\sqrt{N_b(r)}} \propto \frac{N_s(r)}{r} = \frac{2}{r}(1 - e^{-\frac{r^2}{2\sigma^2}}) \tag{5.2}$$

To maximize $\hat{S}(r)$, we let the derivative of it to be zero:

$$\frac{d\hat{S}(r)}{dr} = \frac{d(\frac{2}{r}(1 - e^{-\frac{r^2}{2\sigma^2}}))}{dr} = 0 \tag{5.3}$$

Suppose R is the radius of an optimal bin, and we use σ_θ to substitute σ in (5.1) to (5.3),

$$R = 1.592 \times \sigma_\theta \tag{5.4}$$

For a square bin of length L which has the same area as a circular bin,

$$L = 2.822 \times \sigma_\theta \tag{5.5}$$

In theory, the optimal bin size can be determined by measuring a strong known γ-ray source. If the distribution of the source excess forms a perfect Gaussian, the width is σ_θ. However, this kind of source does not exist for Milagrito. Moreover, the non-Gaussian tail of Δ_{EO} indicates that the measurement of width is meaningless.

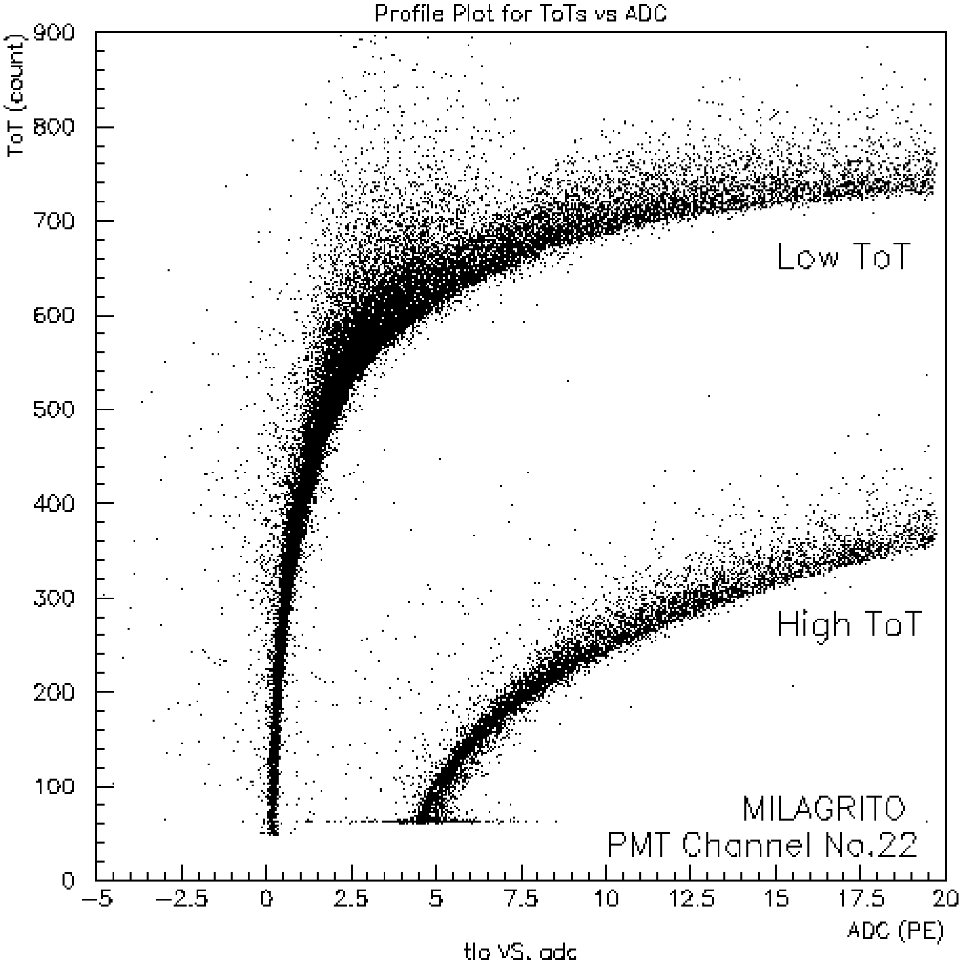

Figure 5.1: Profile plot of ToT (both low ToT and high ToT) vs ADC (for ADC $\leq$ 20 PEs)

5.1.2 The Reason For Non-Gaussian Tail Of Δ_{EO}

As discussed in Section 3.1, a 2-PE-cut is used in direction reconstruction, since pulses less than 2 PEs are mostly late hits. In fact, this cut significantly reduces the non-Gaussian tail of Δ_{EO}. The question is: Is there a certain cut that might totally get rid of the non-Gaussian tail?

To understand better the non-Gaussian behavior, the raw profile distributions of

ADC vs low ToT and high ToT are re-studied. Figure 5.1 shows the ToT distribution of less than 20 PEs. In low PE region (0∼5 PEs), the low ToT has an extremely big flunctuation for a given PE value. The high ToT, however, has much smaller fluctuation than the low ToT.

If the low ToT profile is divided into many small PE regions (0-2 PEs, 2-4 PEs, 4-6 PEs...), the events in each small region form a Gaussian distribution. However, the whole events in the profile plot will not form a Gaussian because the Gaussian distributions of each small PE region differ dramatically from each other due to the big flunctuation, i.e. the sum of Gaussians of different widths is not a Gaussian. If the high ToT profile is divided into small PE regions, just like the low ToT profile was, the Gaussian distributions of each small PE region are similar to each other, therefore the whole events in the high ToT profile forms a Gaussian as well.

To fully eliminate the non-Gaussian effect, a direct option is not to use the low ToT but to use the high ToT only. However, a large number of events will be thrown away. In another words, this option acquires the quality of the data by trading off the quantity of the data. Another option is to avoid the late hits as much as possible since the late hits mainly contributes to the low ToT. This option, however, cannot totally solve the non-Gaussian problem since it still uses the low ToT information. This option can be realized by improving the hardware of detector, and the improvement has been applied on Milagro. [1]

---

[1] In Milagro, a baffle has been put on each PMT. This improvement can increase the vertical light, and block the lights from horizontal direction, which are mostly late hits.

5.1.3 Using Δ-Angle To Determine The Optimal Bin

Because of the non-Gaussian tail of the data, a new method of using Δ-Angle is applied to determine the optimal bin size.

Δ-Angle should be the angular resolution of the real data if the simulation is exactly consistent with the real detector. Thus using Δ-Angle of the Monte Carlo is a better choice than using Δ_{EO}.

The approach we used to find the optimal bin is to calculate the relative significance within a certain bin, and then find the peak of this distribution. The relative significance $\hat{S}$ is:

$$\hat{S} = \frac{N_s(r)}{\sqrt{N_b(r)}} \tag{5.6}$$

In which $N_s(r)$ is the source excess, $N_b(r)$ is the number of background events, and r is the radius of the bin. Assume the background is flat, so $N_b(r) \propto r^2$. In a typical Δ-Angle distribution, $N_s(r)$ can be obtained by counting the number of excess within a certain Δ-Angle, and r is the exactly the Δ-Angle. Thus equation (5.6) becomes:

$$\hat{S} \propto \frac{N_s(r)}{r} \tag{5.7}$$

The optimal bin size R is found when $\hat{S}$ reaches its maximum (Figure 5.2).

This method finds the optimal bin size directly without knowing the angular resolution σ_θ.

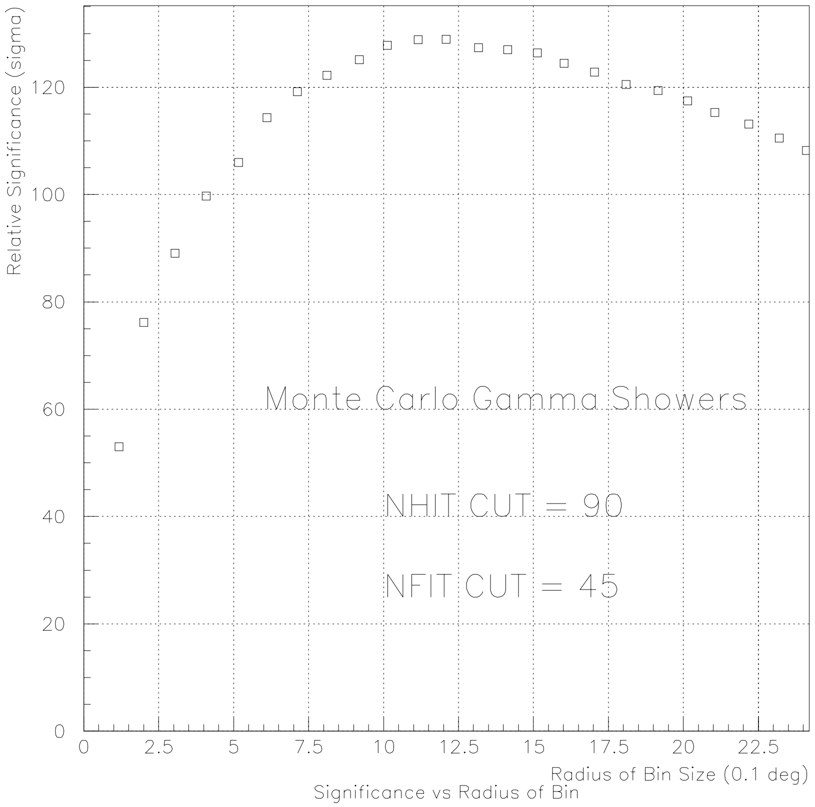

Figure 5.2: Determine the optimal bin size from Δ-Angle for NFIT ≥ 45.

5.1.4 Optimal Bin For Different NFIT

NFIT is the number of PMTs used in the event fitter of (section 3.4). Generally, the angular resolution is better if *NFIT* is bigger, because if more PMTs are triggered, more time meausurements are acquired, and the core location can be determined more precisely, which reduces the error in direction reconstruction.

The relative significance vs bin size for different *NFIT* is shown in Figure 5.3. The optimal bin size is not a strong function of *NFIT*, as it changes only from 1.2°

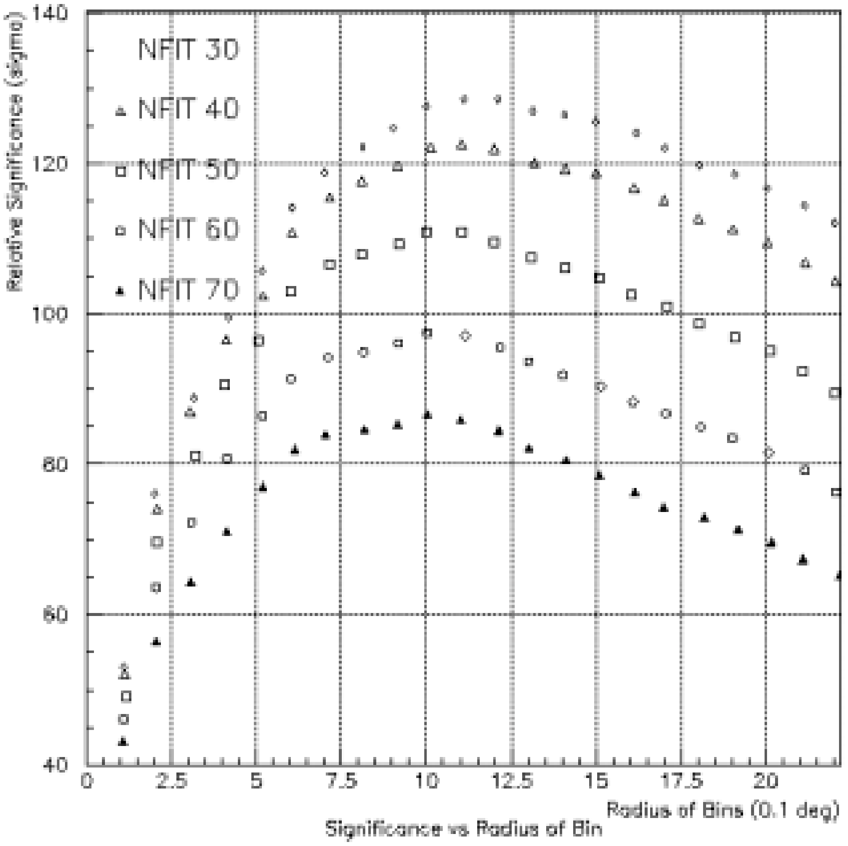

Figure 5.3: Variation of optimal bin size for different *NFITs*. Note: the optimal bin sizes are 1.2∼1.0 degrees when *NFITs* are 30∼70.

to 1.0° when *NFIT* increases from 30 to 70. In another words, to slightly increase the angular resolution ($\sim 0.1°$) means to throw away a large number of events, so this trade-off does not need to be taken.

5.2 Method For All-sky Survey

5.2.1 Sensitive Region Of The Sky For Milagrito

The celestial coordinates, *right ascensions* (RA or α) and *declination* (Dec or δ), are used in the all-sky survey. The galactical coordinates are not used in my thesis because the survey are not necessarily concentrated on the galactic plane of our galaxy.

Milagrito is located in 35.9° N (Section 2.1.2). From the observation view of Milagrito, all sources are rotating around the North Celestial Pole (NCP) of the sky. The sources close to the NCP (declination $\geq 75°$) have large zenith angles ($\theta \geq 40°$), so Milagrito is not sensitive to them. The sources close to the Celestial Equator (CE), also have large zenith angles to Milagrito and only appear in the sky for a short time in a day, thus Milagrito is not sensitive to them either. In reality, Milagrito is sensitive to range of δ ($\sim -4°$ to $\sim 75°$) for all α ($0°\sim360°$) in the sky. The range of the sky accessible to Milagrito is centered at $\sim 36°$ in δ.

5.2.2 Bins And Iteration

An all-sky survey is a blind search for sources, which means the positions of the potential sources are unspecified. Since every portion of the sky has equal probability of source excess, the bin size of the survey should be fixed. Each bin is an independent search of the sky. To have good bin iteration power in the survey and to avoid unnecessary overlaping of bins, square bins are used; round bins are more suitable for point sources with known positions. To maximize the significance, the optimal bin size should be used as well.

The whole α range might not be an exact multiple of the optimal bin size. This might cause problems in the iteration of bins. One option is to divide the whole α into 2 halves, allowing each half to cover more than 180° in α so it becomes an exact multiple of the bin size. In this case, the map changes into 2 "Half-sky maps" instead of an "All-sky map", and the effect of over-sampling should be estimated because events of a certain region of α will be used twice. Another option is to generate one whole map of α, allowing one special bin to have different size than the rest of the bins.

In this work, the second option was taken. The regular bin width was chosen to be $2.2222^\circ/\cos(\delta)$. For example, at $\delta = 0^\circ$, 162 α bins are used, and the last one is of size 2.2228° to adjust the total size to 360°. At other δ, the number of α bins is given by equation (5.8) and the size of the last bin is adjusted according to the portion l of the sky left to complete the 360° survey. If after the last iteration $1.1111^\circ \leq 1 \ \cos(\delta) \leq 2.2222^\circ$, then a new bin is created of size l; if $l \ \cos(\delta) < 1.1111^\circ$, then no extra bin is created, instead, l is added to the size of the previous bin.

The iteration, or the number of bins in α, is determined by:

$$Bin(\alpha) = integer(162 \times cos(\delta)) \tag{5.8}$$

The whole δ range is divided into 34 equal bins of 2.2222°.

5.2.3 Significance Loss And Multiple Search

Since the all-sky survey is a blind search, the probabilty that a source happens to be in the center of a bin is extremely small. If a source is not centered in the bin, some of its significance will be lost. To figure out the loss of significance, a series of Monte Carlo simulations were applied.

Suppose n_s, n_b stand for the number of excess and background events in an optimal bin, respectively, and N_s, N_b stand for the total number of source events and background events. The optimal bin contains 72% of the source excess if the bin is centered on the source:

$$N_s = \frac{n_s}{0.72} = 1.39 \times n_s \tag{5.9}$$

The source events thrown form a 2-dimensional Guassian distribution of a width 0.8°, whereas the background events were thrown homogenously. The length of the square optimal bin is $\mathrm{L} = 2 \times 1.12°$, which is appropriate to an angular resolution of 0.8°. Each time the source events and the background events were thrown, the number of excess events in the optimal bins of various offsets to the center of the source were counted, and the corresponding significances $\hat{S}$ were computed, respectively.

Simulations for various source bin excesses ($50 \sim 7000$) with significances of 3.5σ and 4.0σ at the bin center have been studied. Figure 5.4 shows the significance loss as a function of the source offset from the bin center. If a source happens to be at the edge of a bin, the significance loss is up to 43%.

To avoid considerable loss of significance, I use overlapping bins. In general, the

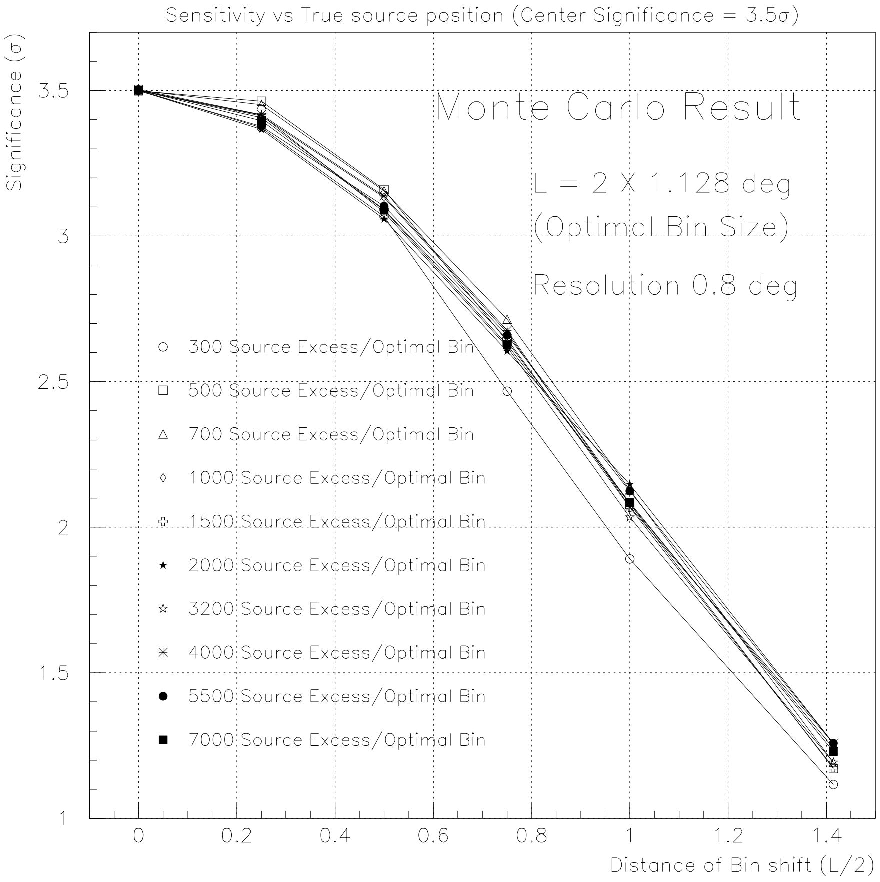

Figure 5.4: Significance loss as a function of relative location to the center of an optimal bin. The center significance is 3.5 σ.

more overlapping bins are used, the less significance will be lost. However, more overlapping bins means more penalty to pay in statistics (Chapter 6). According to Figure 5.4, the maximum source offset to the center of a bin of using 4 overlapping bins is $\sqrt{2}/4 \times$ L (L is the size of the optimal bin), which results in a maximum significance loss of 20%∼25%. If 9 overlapping bins are used, the maximum offset to the center of a bin is $\sqrt{2}/6 \times$ L, which results in a maximum significance loss of

9%∼12%. I used 4 overlapping bins in the all-sky survey.

The problem of using overlapping bins in an all-survey map is that there are different number of bins for different δ. To solve this problem, I made 4 overlapping all-sky maps, with each map shifted either in α or δ or both for half of the bin size. For each map, the bins are independent to each other.

The first map covers a range of δ from -3.8839° to 71.6709°, with a starting $\alpha = 0^\circ$; the second map covers the same range of δ as the first one, but with an offset of 1.1111° in α; the third map covers a range of δ from -4.995° to 70.5598°, with a starting $\alpha = 0^\circ$; the fourth map covers the same range of δ as the 3^{rd} one, but with an offset of 1.1111° in α.

5.3 Time-sloshing And Background Estimation

Unlike Milagro, which has a hadronic layer to provide some background rejection, Milagrito has only one layer of PMTs. We estimated the background via the method of time-sloshing (TS).

In the TS method, one accumulates events during a time period (normally 1∼2 hours) during which the experiment environment is assumed constant. An event of a fixed position is assigned a time information of a real randomly chosen event in this period. By looping over all the events for many times, the generated background is a good representation of the true background.

The assumption for TS is that all events are due to background. In case there is a strong excess of source events, some of the source excess events will be treated as background events in TS, so the background will be over-estimated and some significance of the source will be lost. The percentage of significance loss depends on how many bins there are in a time-sloshing period. For a 2.2° source bin, if the background is estimated once every 2 hours, there are about 14 bins in the TS period, so the maximum significance loss for a strong source is 1/14 (∼7%). Since very strong sources are not observed with Milagrito, so in general TS method is effective in background estimation.

The most important thing for the time-sloshing technique is the number of times the events are used. If the looping time is too small (i.e. 1∼3 times), there are statistical fluctuations in the background estimation; on the other hand, if the looping times is too big (i.e. ∼100 times), it will take a considerably more computer time without improving the quality of the background. A proper number of times in TS will minimize the statistical flunctuation in the background estimation, and take as less computer time as possible.

The result of the TS technique is further discussed in Chapter 6.

5.4 Significance Estimation For Time-Sloshing Method

In 1983 Li and Ma ([33]) showed how to properly estimate the significance of an excess of events, when measurements are on and off source. This paper has been widely adopted in astrophysics. The Li-Ma formula for significance is:

$$\hat{S} = \frac{N_{on} - \alpha N_{off}}{\sqrt{\alpha(N_{on} + N_{off})}} \tag{5.10}$$

Where N_{on} is the number of on-source events, N_{off} is the number of off-source events, α is ratio of time of measuring with source on ($\mathrm{t_{on}}$) to the time of measuring with source off ($\mathrm{t_{off}}$).

$$\alpha = \frac{t_{on}}{t_{off}} \tag{5.11}$$

Applying the maximum likelihood method, the above formula becomes:

$$\hat{S} = \sqrt{2}[N_{on}ln[\frac{1+\alpha}{\alpha}\frac{N_{on}}{N_{on}+N_{off}}] + N_{off}ln[(1+\alpha)\frac{N_{off}}{N_{on}+N_{off}}]]^{1/2} \tag{5.12}$$

Equ. (5.10) and (5.12) are essentially the same except that the likelihood method requires N_{off} to be not too small.

Special care needs to be taken while applying Li-Ma formalism onto the time-sloshing method [34]. In the observation with Milagrito, the excess events are in generally included in the background estimation by using time-sloshing, so if there is an excess, the background is over estimated. If there is an excess,

$$N_{off} = \frac{N_{on}}{\alpha} - \frac{N_s}{\alpha} \tag{5.13}$$

so equation (5.10) becomes:

$$\hat{S} = \frac{(N_{on} - \alpha N_{off})}{\sqrt{\alpha(1+\alpha)N_{off} + \alpha N_s}} = \frac{N_s}{\sqrt{(1+\alpha)N_b + \alpha N_s}} \tag{5.14}$$

Chapter 6

Results And Discussion

6.1 Data Selection

The analysis was performed with the whole Milagrito data set, which covers a period from February 8, 1997 (MJD50487[1]; Run 1) to May 7,1998 (MJD50940; Run 896). It contained a total of about 8.9×10^9 events. The total effective exposure time of Milagrito was about 370 days, with most of the downtime being due to power outages and maintenance. The total number of Runs is 770. Run 490, 825, 832-836 were excluded because none of them contained more than 10,000 events, which is not enough for time-sloshing. Run 601, 602 (MJD50780, MJD50905) were excluded because of the problems in time information.

We required $NFIT \geq 50$ for events used in the analysis. The data sample contained

---

[1] Modified Julian Date(MJD) equals to Julian Date(JD) minus 2,400,000.5. One Julian Day is $\sim$240 seconds shorter than one normal day.

3.4×10^9 events which were successfully reconstructed and satisfied this *NFIT* cut. The number of trials in time-sloshing was 15, and the period of doing time-sloshing (TS) was either 2 hours or 1 million events. Before MJD50810, the period of doing TS was mainly 2 hours, and the events accumulated in this period was ~750,000; after MJD50810, Milagrito had a higher trigger rate because the pond was filled with more water, so the period of TS was whenever the events accumulated reached 1 million events.

If the end of a Run was reached, the remaining events between the previous period and the end were added to the previous period with the background re-estimated.

We peformed a search for steady sources and a search for transient sources. The search for steady sources included the data set for the entire run. In addition, a search for transient sources used one month as a searching period was performed: no shorter time period of searching was taken. The whole data set was divided into 15 equal Julian months, each of which includeed 30 Julian days except for the last one which contained 33 days, and there was no overlap among those 15 periods.

6.2 Search For Steady Emission In Northern Sky

6.2.1 Four Dependent All-Sky Maps

I examined four all-sky maps, each consisting of of 34×162 bins. The bin size is 2.2222° (in δ) $\times 2.2222^\circ / \cos(\delta)$ (in RA). The starting coordinates of each map are

Map name	Max Dec(°)	Min Dec(°)	Start RA(°)
A1	70.5598	-4.9950	0.0030
A2	70.5598	-4.9950	1.1141
B1	71.6709	-3.8839	0.0030
B2	71.6709	-3.8839	1.1141

Table 6.1: Coordinates of the 4 all-sky maps.

listed in Table 6.1.

Since the number of bins changed with δ, it is more convenient to draw a map with axes of number of bins instead of the real RA and δ. Figure 6.3 and 6.4 are the 2-dimensional significance maps for all northern sky. To find any position in RA and δ on a map, the conversion of bin coordinates into RA and δ are given below.

For map A1 and A2, suppose n_δ is the bin number in Figure 6.3, the $\delta(^\circ)$ of the center of the bin is:

$$\delta = (n_\delta + 1) \times 2.2222 - 3.8839 \tag{6.1}$$

And, for map B1 and B2,

$$\delta = (n_\delta + 2) \times 2.2222 - 4.995 \tag{6.2}$$

For map A1 and B1, the RA(°) is:

$$RA = \frac{n_\delta}{162 \times Cos\delta} \times 360 - \frac{10}{9 \times Cos\delta} \tag{6.3}$$

And, for map A2 and B2,

$$RA = \frac{n_\delta}{162 \times Cos\delta} \times 360 - \frac{20}{9 \times Cos\delta} \tag{6.4}$$

Figure 6.2 is one of the four all-sky events maps. As expected, the event map peaks at $\delta \sim 36°$, which is ~16.5 (in δ) in the map.

For each map, the results show that the significance of each bin forms a normal Gaussian distribution centered at 0 with a width of ~1. The width is less than 1 because of Li-Ma estimation of the significance (Section 5.4).

The Gaussian covers a range of $\sim \pm 3.4\sigma$. Of all the 4 maps, only map B2 contains an excess of 3.9σ, which occurs at RA = 29 and $\delta = 23$. By using formulae (6.2) and (6.4), the position of this bin is: RA = 78.23°, $\delta = 50.56°$.

6.2.2 Probablity of Fluctuation for Multiple Excesses

Suppose there are totally n trials, each trial has an equal probability of p, and there is a distinct excess in the n trials, what is the probability that the excess is within the fluctuation?

The probabilities of n trials obey the Binomial distribution in the [0,1] space:

$$P_i = C_n^i p^i (1-p)^{n-i} \tag{6.5}$$

in which $i = 0, 1, ..., n$. By definition, the total probability equals to 1:

$$\sum_{i=0}^{n} P_i = \sum_{i=0}^{n} C_n^i p^i (1-p)^{n-i} \equiv 1 \tag{6.6}$$

The probability for “at least one excess” equals to the total probability subtracting the probability of “no excess”, which is:

$$P_{n\geq 1} = 1 - P_0 = 1 - C_n^0 p^0 (1-p)^{n-0} = 1 - (1-p)^n \tag{6.7}$$

Note: $P_{n \geq 1} \approx np$ when $np \ll 1$. To make the calculation more direct and easier, the above equation can be changed into:

$$P_{n\geq 1} = 1 - e^{ln(1-P)^n} = 1 - e^{nln(1-P)} = 1 - e^{nln\varphi(\sigma)} \tag{6.8}$$

where $\varphi(\sigma)$ is the integration of Gaussian as expressed in equation (4.7), or,

$$\varphi(\sigma) = \frac{1}{\sqrt{2\pi}} \int_{-\infty}^{\sigma} e^{-\frac{v^2}{2}} dv \tag{6.9}$$

Equation 6.7 has been widely used to calculate the probability of fluctuation for multiple trials. However, for an all-sky survey, there might be many excesses on a map, so equation (6.7) is not correct unless there is only 1 excess in the map. For multiple excesses on an all-sky map, a new method of calculation must be derived.

For the case of "at least 2 excesses", the fluctuation probability should be the total probability subtracting the probability of both "no excess" and "one excess":

$$P_{n\geq 2} = 1 - (P_0 + P_1) = 1 - [(1-p)^n + np(1-p)^{n-1}] \tag{6.10}$$

Similarly,

$$P_{n\geq 3} = 1 - [(1-p)^n + np(1-p)^{n-1} + n(n-1)p^2(1-p)^{n-2}] \tag{6.11}$$

For "at least m excesses", a general formula is given:

$$P_{n\geq m} = 1 - \sum_{m=0}^{m} C_n^m p^m (1-p)^{n-m} \tag{6.12}$$

Note: In equation (6.12), p is the probability of the m^{th} excess if there is only 1 trial, and $P_{n\geq m}$ has nothing to do with the excesses of higher significance than the m^{th} one.

In an independent all-sky map, for the 1 excess of 3.9σ, and $n = 4319$ trials for an all-sky search,

$$P_{n\geq1}(3.9\sigma) = 1 - e^{4319\times ln(0.9999519)} = 0.1876 \tag{6.13}$$

However, if four group of overlapping bins are used, and the effective trial n_{eff} at 3.9σ is 2.5 (Section 4.3.4), the probability becomes:

$$P'_{n\geq1}(3.9\sigma) = 1 - e^{4319\times 2.5\times ln(0.9999519)} = 0.4051 \tag{6.14}$$

6.2.3 Upper Flux Limits For A Survey with Four Overlapping Bins

At a given instant, a detector is sensitive to those sources that appear at small zenith angles, and is not sensitive to the sources at large zenith angle. In addition, all celestial sources are moving relative to the detector due to the rotation of the earth. Some sources which have a declination equal to the latitude of the detector will pass right over head at a certain instant; other sources will never pass over head. In a full source-day, the γ-ray sources that happen to pass over head have more trigger possibilities than that of the γ-ray sources that never pass over head. So the flux limit of sources is a function of declination.

Milagrito is located in the lattitude of 35.9° N. So from the Milagrito's view, all celestial sources are rotating around the north pole in the sky. For a given significance, sources of declination (δ) equal to 35.9° has the highest sensitivity, or, in another words, the lowest flux limit than other sources.

To determine the flux limit of a source at a given declination, equation (4.4) can be used. However, in this case, N_{day} should be changed into N_{CL}, which is the number of photons of a certain confidence level (CL), and the $\Phi(E)$ is unknown.

$$N_{CL} = \int_E \int_{Day} \Phi(E) A_{eff}(E, \theta(t)) dEdt \tag{6.15}$$

The CL is determined by:

$$P = 1 - (1-p)^{n_{eff} \times N_{trial}} \tag{6.16}$$

where n_{eff} is the effective trial (Section 4.3.4) for overlapping bins.

If no-overlapping bins are used, $n_{\mathit{eff}} = 1$. $N_{trial} = 4319$ because there are 4319 independent bins. For 99% CL, P = 1 - 99% = 0.01, a significance of 4.58σ is needed for 99% CL. Similarly, for 95% CL, P = 1 - 95% = 0.05, a significance of 4.23 σ is needed for 95% CL; and 4.06σ is needed for 90% CL.

In a search with overlapping bins, a penalty in statistics of using more effective trials must be paid. The CL for a survey with overlapping bins can be calculated with equation (6.16), where n_{eff} is 2.5 for four overlapping bins. To have a 90% CL of flux, a significance of 4.27σ is needed. Similarly, for 95% and 99% CLs, the significances required are 4.43σ and 4.77σ, respectively. The strongest excess in the four all-sky maps is 3.9σ, so no source with flux greater than 90% CL was discovered.

The upper flux limit (Φ(E$\geq$1 TeV)) of 90% CL for a survey with overlapping bins is shown in Figure 6.6. To compare the flux limits with a known source, the flux of the Crab (measured by Whipple) for energy E $\geq$ 1 TeV was determined and put into the plot. The flux of the Crab for E $\geq$ 1 TeV can be calculated with equation (1.3), which is $2.15 \times 10^{-7}\text{m}^{-2}\text{s}^{-1}$.

6.2.4 Significance Of Known Sources

There are several known γ-ray sources in Milagrito's field of view, including the Crab Nebula, Mrk501 and Mrk421. Since all-sky search randomly chooses the starting position of bins, none of these sources is in the center of any bin. However, there is always a bin on each map that contains the source, and the source in 1 of the 4 is closer to the center of the bin than others.

For example, map B2 has a bin which center is more close to the position of the Crab Nebula than other maps, the bin position in the map is (35,10), of which (35.50,9.50) is the center. The Crab Nebula is located at (34.49,9.63), which indicates that up to 7% of its significance might be lost.

The suitable maps for Mrk501 is B1. The location of Mrk501 in its source bin indicates a significance loss of up to 11%.

The result for known sources are listed in Table 6.2 (Position of sources are from J2000). Note: ΔRA and $\Delta\delta$ are the distances to the center of the nearest bin.

A claim of an observation of TeV γ-ray emission from Mrk501 with Milagrito detector was published in the *Astrophysical Journal Letter* on November 1999 [35]. In this publication, a statistical significance of 3.7σ was obtained after all Mrk501

Source Name	RA(°)	δ(°)	Excess (10^2)	N_{off}(10^5)	Signif.
Crab	83.63	22.01	10.5	9.15	1.1σ
Mrk421	166.11	38.21	-8.5	11.3	-0.80σ
Mrk501	253.47	39.76	29.8	11.5	2.8σ
1ES2344+514	356.15	51.43	2.27	10.6	0.22σ

Table 6.2: Significance of known γ-ray sources.

events in Milagrito data set were studied. In the all-sky survey, a significance of 2.8σ was observed at the position of Mrk501. This result is consistent with the publication, since Mrk501 is not centered. The excess rate for Mrk501 is 8.1/day, which is also consistent with the result of the publication (8.7 photons per day).

If we assume that the flux of the Crab measured by Whipple is correct, then the daily excess of E≥1 TeV emission for Milagrito should be ~3.2. The daily event rate measured with Milagrito at $\delta \sim 22°$ is 1929±62, therefore we expect to see 1295 excess and a significance of 1.4σ in 370 Julian days. The result of the Crab (1.1σ) is consistent with the prediction because the Crab is not centered.

6.3 Search For Transient Emission Of The Whole Northern Sky

6.3.1 Monthly Excesses For Blind Searches

To study transient emission of the northern sky, the Milagrito data set is divided into 15 segments, each of which is a Julian Month except for the last month which

Map Name	Significance	RA(bin)	Dec(bin)	RA($^\circ$)	Dec($^\circ$)	Events($\times 10^6$)
B2-No.1	4.0σ	39	9	89.69	19.44	81.5
A2-No.2	3.8σ	53	9	121.85	18.33	149.5
B2-No.3	3.8σ	77	17	212.66	37.22	243.8
A1-No.8	3.9σ	67	30	351.19	65.00	220.6
A1-No.8	3.8σ	28	-1	61.25	-3.89	220.6
B2-No.8	3.8σ	16	8	35.00	17.22	220.6
B1-No.9	4.4σ	118	1	261.22	1.67	228.0
B1-No.11	4.0σ	52	4	115.64	8.22	210.4
A1-No.13	3.9σ	56	22	182.12	47.22	276.4
B2-No.13	3.8σ	71	1	155.62	1.67	276.4
B2-No.13	3.7σ	53	9	122.67	19.44	276.4

Table 6.3: Excess bin ($\geq 3.7\sigma$) for Transient Search.

has 33 Julian Days. Of all the 60 (15×4) maps, there are 10 excesses which have significance $\geq 3.7\sigma$. And of those 10 excesses, 2 are overlapped for a quarter of their bins. The result of excess bins are listed in Table (6.3).

Because each monthly search was independent, the probabilities for background fluctuation would be:

$$P_{n\geq 1}(4.4\sigma) = 1 - e^{4319\times ln(0.99999459)} = 0.02309 \tag{6.17}$$

$$P_{n\geq 1}(4.0\sigma) = 1 - e^{4319\times ln(0.99996833)} = 0.1278 \tag{6.18}$$

$P_{n\geq 1}(3.9\sigma) = 0.1876$ as shown in equation (6.13), and,

$$P_{n\geq 1}(3.8\sigma) = 1 - e^{4319\times ln(0.99992765)} = 0.2684 \tag{6.19}$$

Actually there are 2 excesses more than 3.8σ (including a 3.9σ excess) on map A1-No.8, so the probability of fluctuation can be obtained from equation (6.10):

$$P_{n\geq 2}(3.8\sigma) = 1 - (1-p)^{n-1}[(1-p)(1-n)+n] = 0.03974 \tag{6.20}$$

Month No.	M.J.D.	Run No.	Events($\times 10^6$)	Significance
1	50487-50517	1-25	81.5	0.47σ
2	50518-50547	26-99	149.5	0.75σ
3	50548-50577	100-202	243.8	0.77σ
4	50578-50607	205-284	225.4	-1.3σ
5	50608-50637	285-345	242.8	0.10σ
6	50638-50667	346-401	190.9	0.65σ
7	50668-50697	402-464	198.6	2.4σ
8	50698-50727	465-518	220.6	0.17σ
9	50728-50757	519-570	228.0	1.56σ
10	50758-50787	571-603	164.3	0.18σ
11	50788-50817	604-637	210.4	1.1σ
12	50818-50847	638-673	274.3	0.60σ
13	50848-50877	674-749	276.4	0.44σ
14	50878-50907	750-828	363.2	2.3σ
15	50908-50940	829-896	361.2	0.45σ

Table 6.4: Monthly Monitoring for Mrk501.

Also, on map B2-No.13, there happened to be 2 excesses more than 3.7σ (including a 3.8σ excess), so,

$$P_{n\geq 2}(3.7\sigma) = 1 - e^{(n-1)ln\varphi(3.7)}e^{ln[(1-n)\varphi(3.7)+n]} = 0.07995 \tag{6.21}$$

Considering each monthly search is one trial of the whole year data set, a statistical penalty should be paid in calculating the fluctuation probability:

$$P'_{n\geq 1}(4.4\sigma) = 1 - e^{15\times 4319\times 2.5\times ln(0.99999459)} = 0.5836 \tag{6.22}$$

which is not significant at all.

6.3.2 Monthly Monitoring For Mrk501

Mrk501 is detected to be the strongest TeV γ-ray source so far by Air Cerenkov Telescope. However, it is not a steady source as it flares from time to time. During February to October each year, Mrk501 appears at night, offering the possibility of observation for Air Cerenkov Telescope. In November and December 1997 and January 1998, Milagrito still monitored Mrk501. The result of monthly monitoring of Mrk501 is listed in Table 6.4 (Note: the Air-Cherenkov data for Mrk501 during month 10, 11, 12 is not available.)

6.3.3 Flux Limits For Monthly Search

Similar to section 6.2.3, the flux limits can be determined with equation (6.16), except that a statistical penalty for monthly trials should be paid.

To be 90% confidence on the flux in monthly searching, a statistical significance of $\geq 4.84\sigma$ is needed. For 95% CL, a significance of $\geq 4.98\sigma$ is required.

6.4 Prospects For All-sky Survey With Milagro

The results showed that an all-sky survey with Milagrito is not significantly sensitive for unknown sources. The sensitivity of Milagrito was limited by its small surface area and no background rejection. However, Milagrito served as a prototype of Milagro. Milagro has a much bigger size (60m×80m) and an additional muon layer of PMTs. With its larger effective area and the ability to reject some of the background, Milagro will be much more sensitive than Milagrito. Thus fruitful results are expected with Milagro.

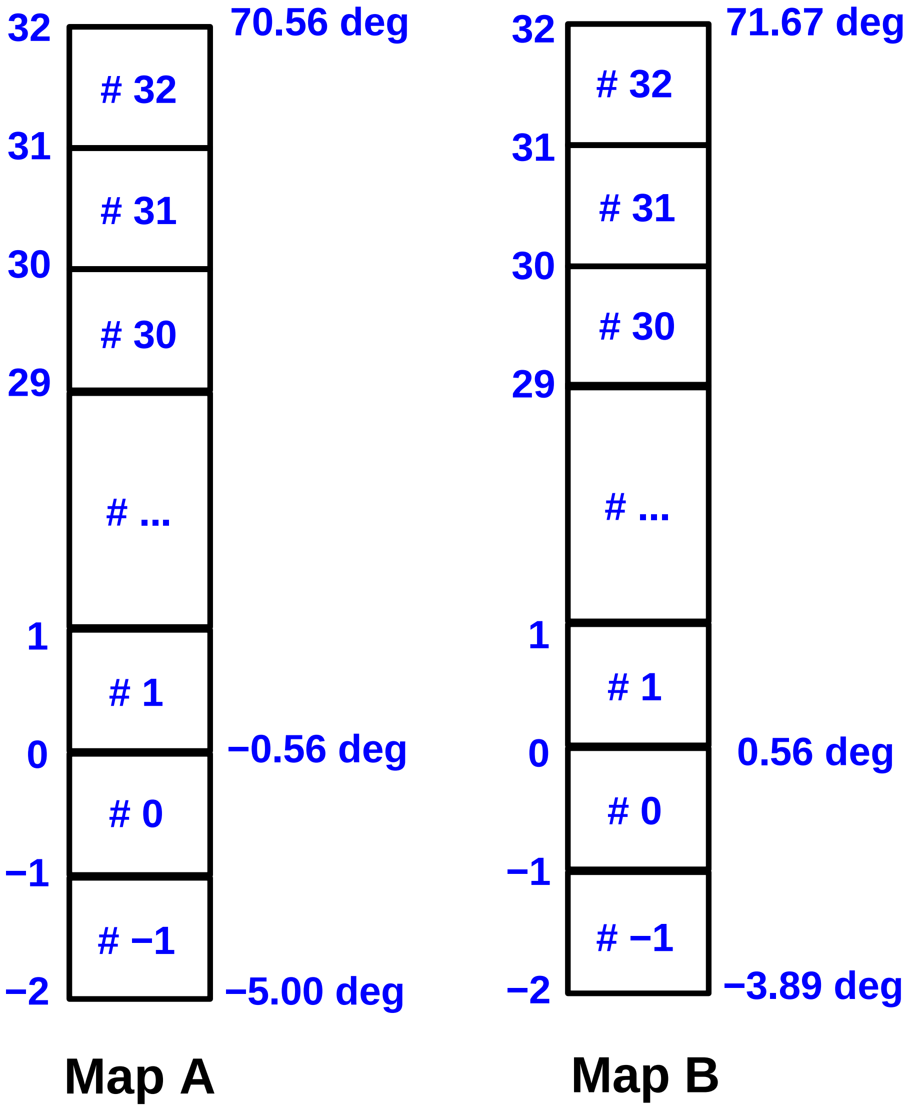

Figure 6.1: Microscopic view of vertical axis of maps. Map A stands for maps that cover a δ range from -5° to 70.56°; map B stands for maps that cover a δ range from -3.89° to 71.67 °.

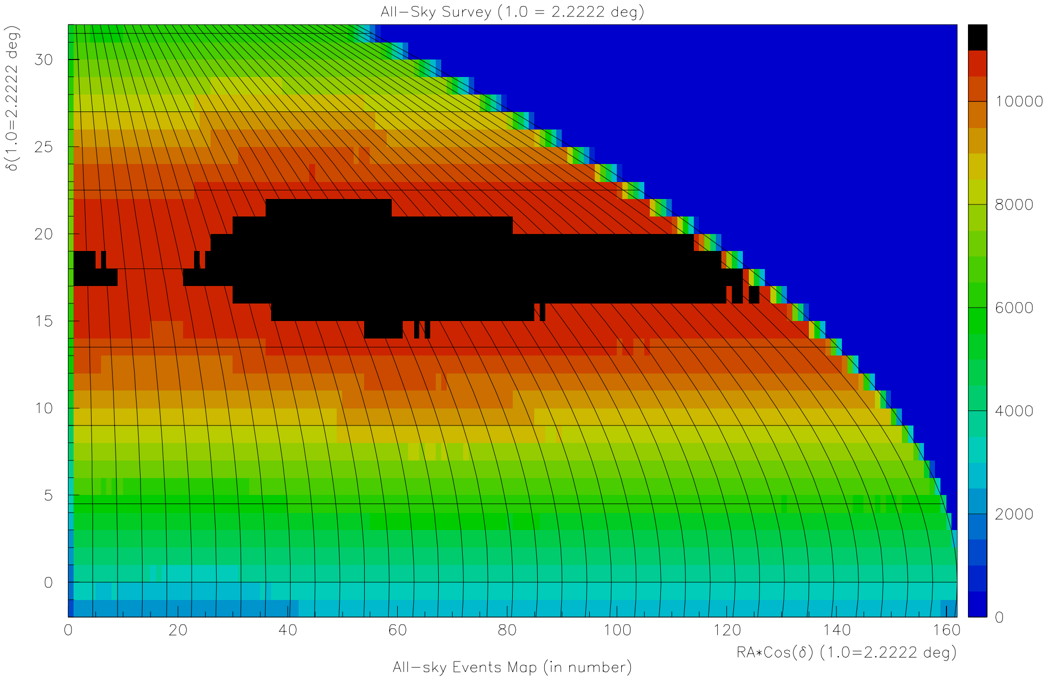

Figure 6.2: Event map for all-sky survey. Note: The coordinate units are in numbers.

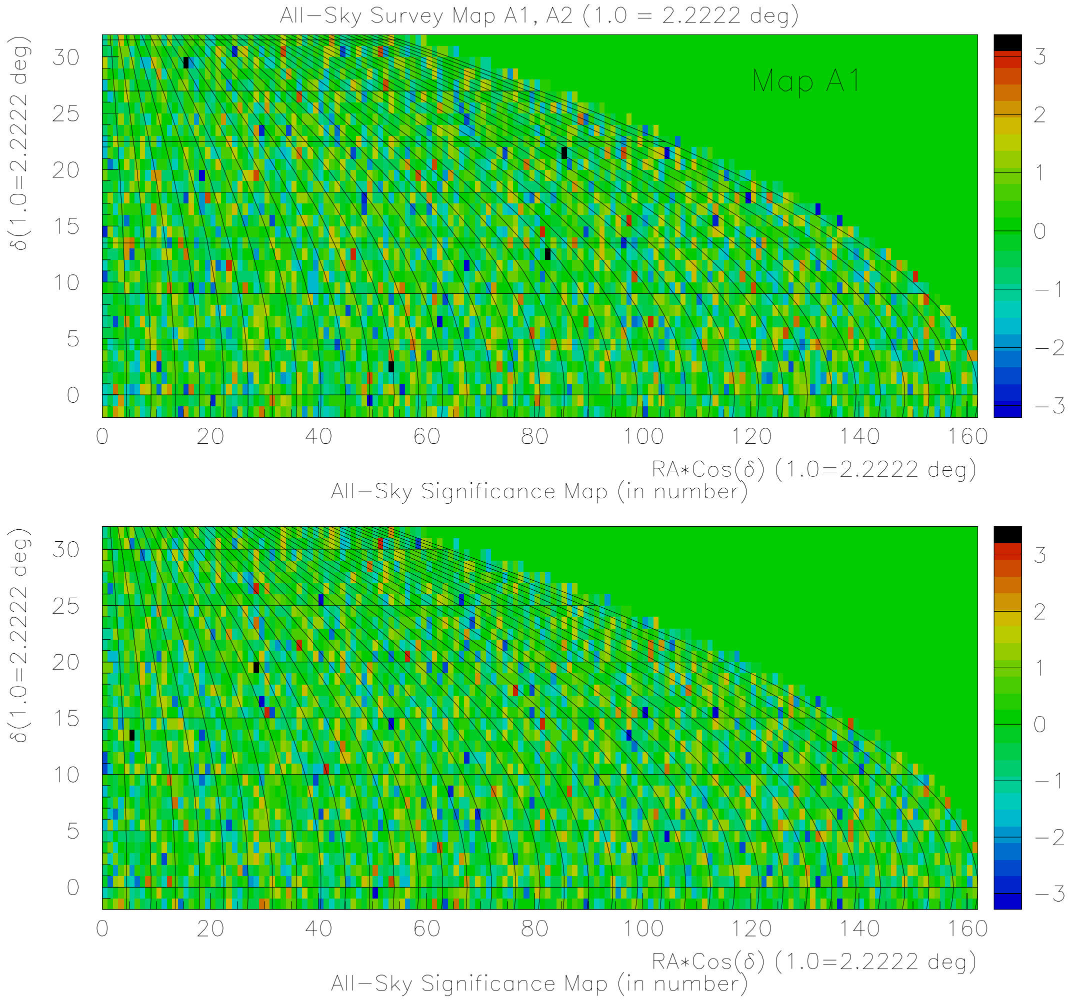

Figure 6.3: All-sky survey significance map A1 and A2. The upper one is A1 and the lower one is A2.

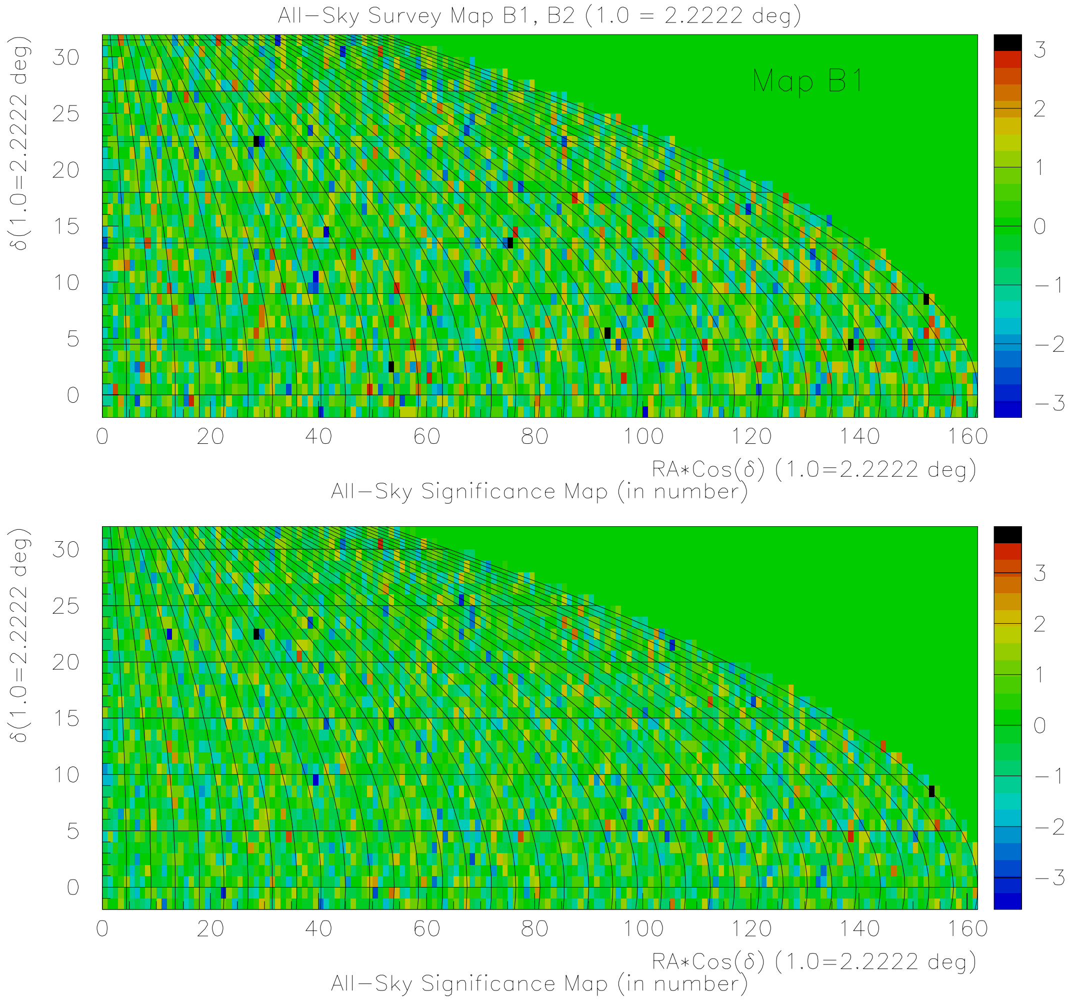

Figure 6.4: All-sky survey significance map B1 and B2. The upper one is B1 and the lower one is B2

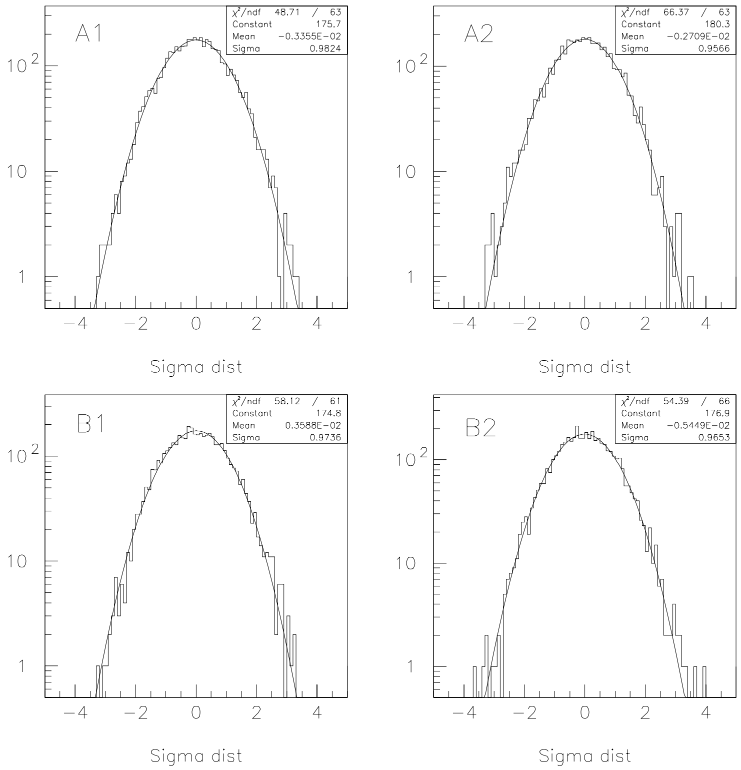

Figure 6.5: σ distributions of the 4 all-sky maps for whole data set.

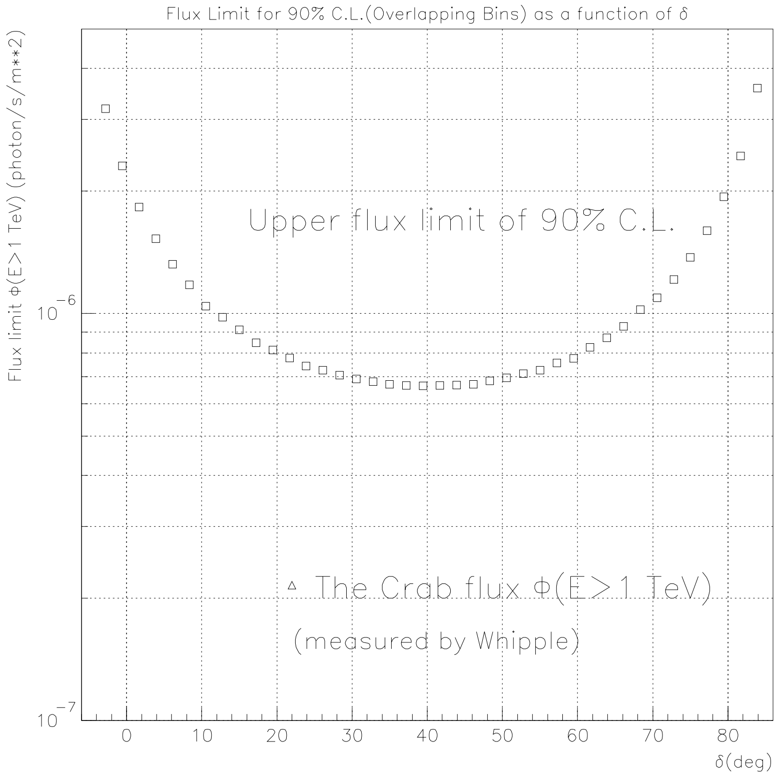

Figure 6.6: Upper flux limit of 90% CL as a function of declination for Milagrito. The flux of the Crab (Φ(E≥1 TeV)), measured by Whipple, is marked in the figure. The upper flux limit of 95% CL is 4% higher than that of 90% CL, and the upper flux limit of 99% CL is 12% higher than that of 90% CL.

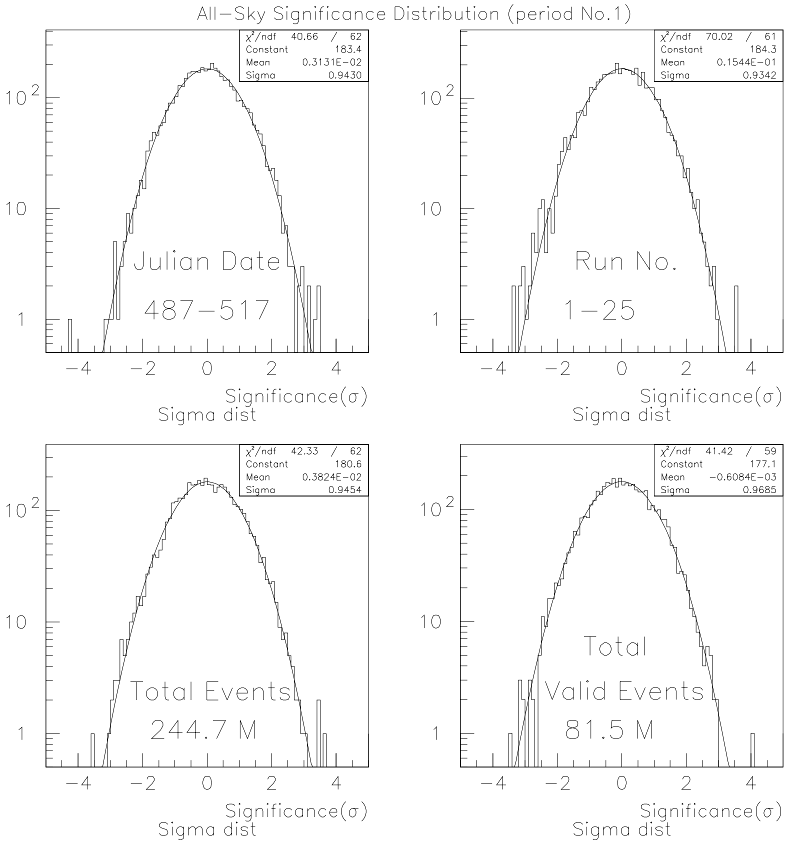

Figure 6.7: σ distributions of the 4 all-sky maps for month No.1.

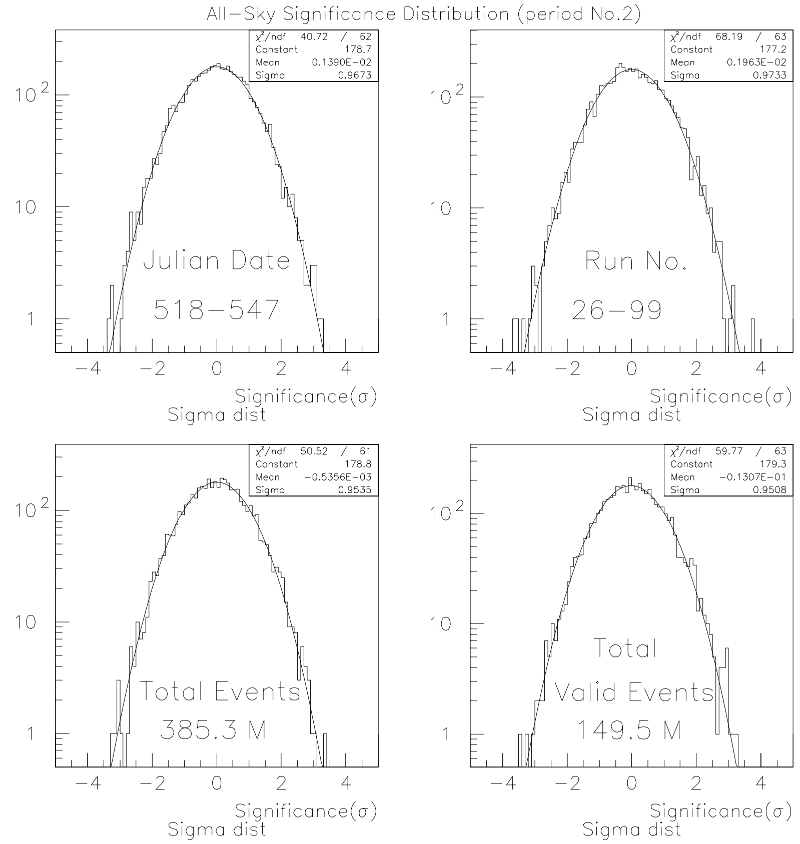

Figure 6.8: σ distributions of the 4 all-sky maps for month No.2.

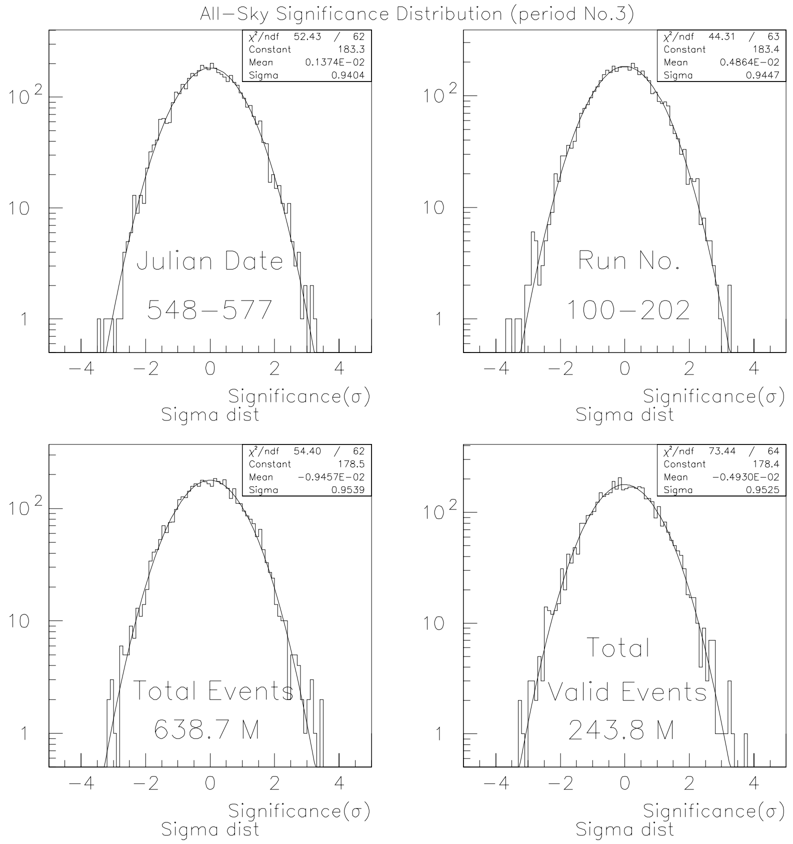

Figure 6.9: σ distributions of the 4 all-sky maps for month No.3.

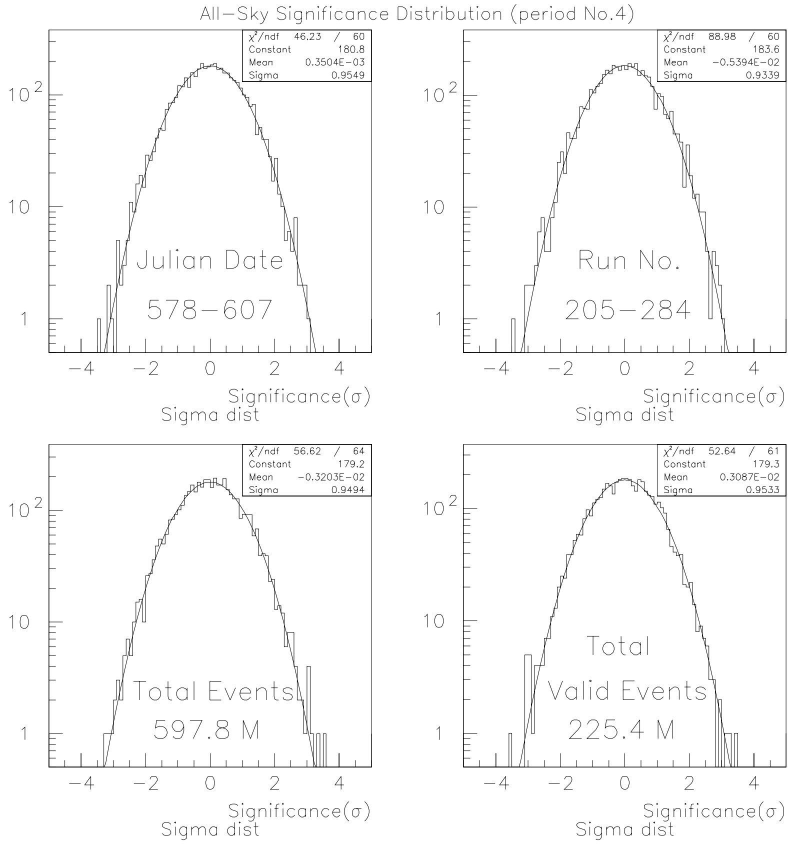

Figure 6.10: σ distributions of the 4 all-sky maps for month No.4.

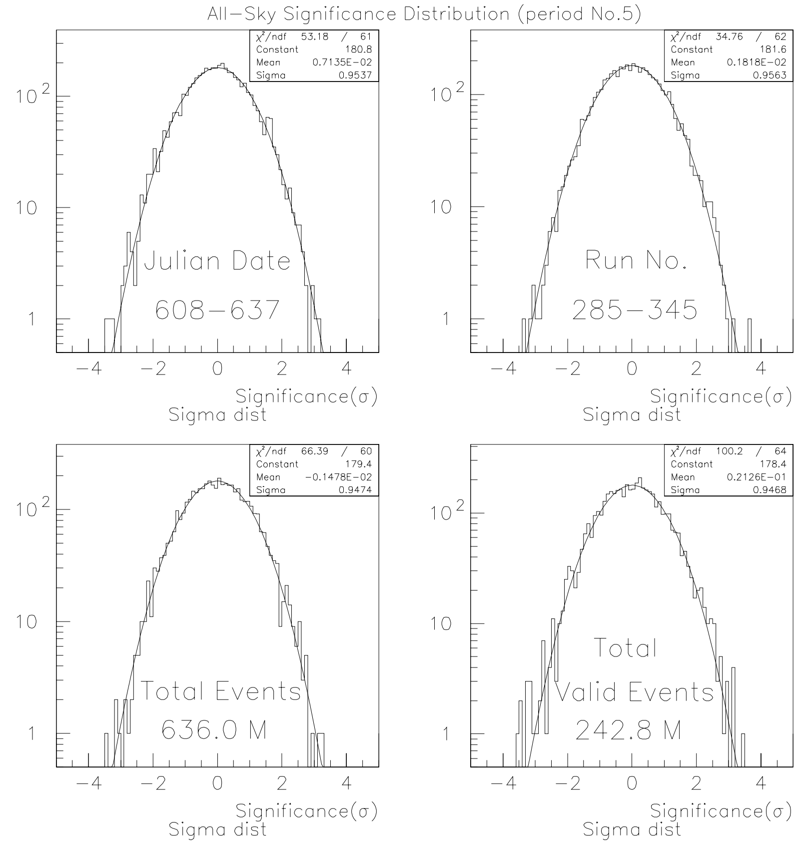

Figure 6.11: σ distributions of the 4 all-sky maps for month No.5.

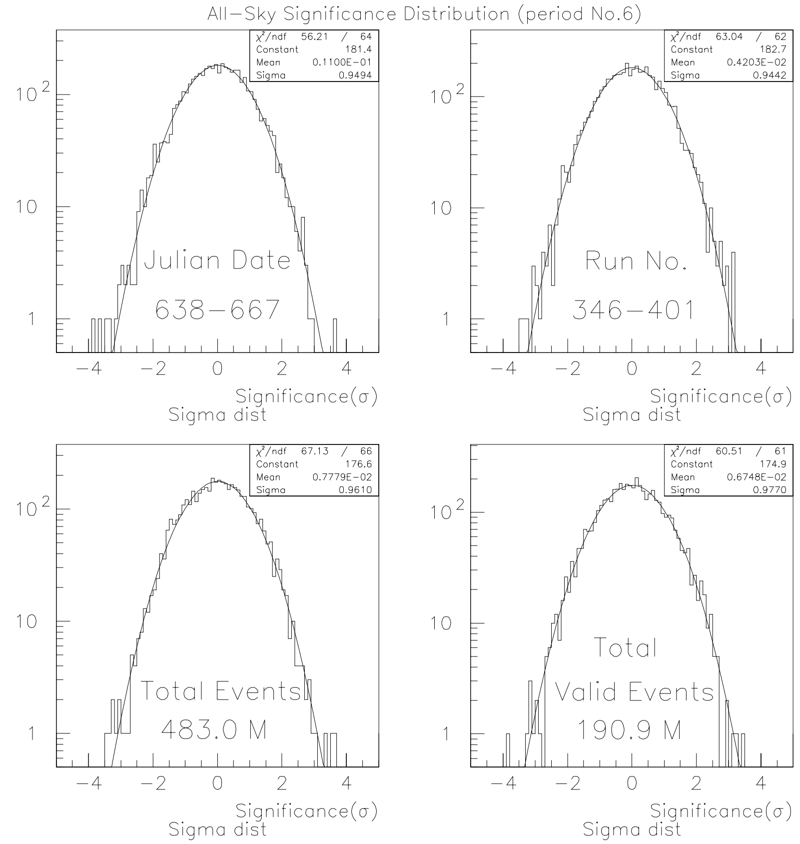

Figure 6.12: σ distributions of the 4 all-sky maps for month No.6.

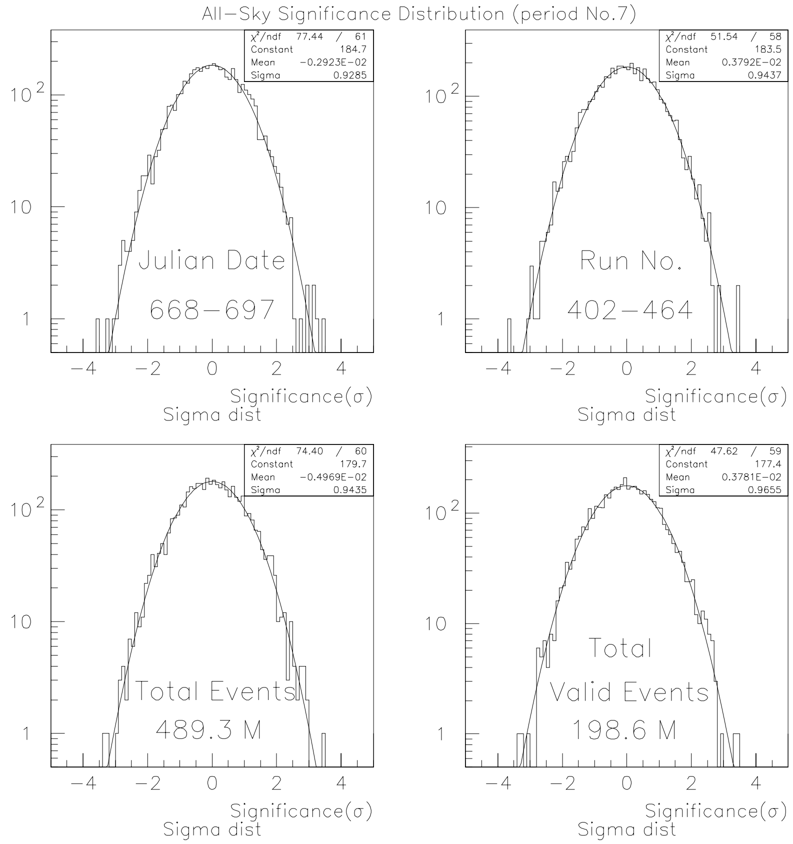

Figure 6.13: σ distributions of the 4 all-sky maps for month No.7.

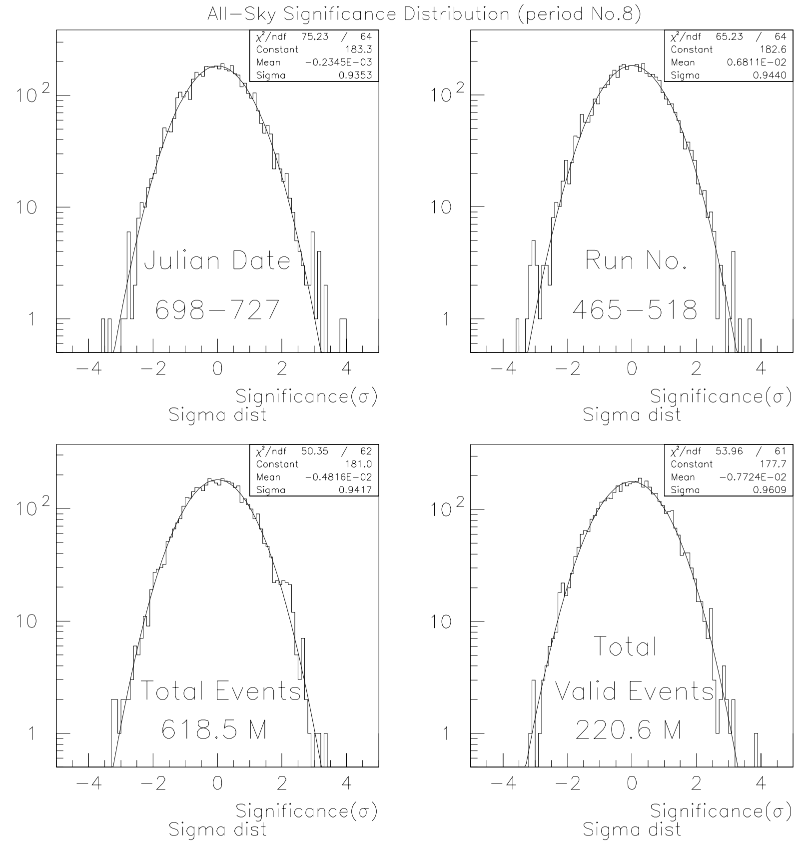

Figure 6.14: σ distributions of the 4 all-sky maps for month No.8.

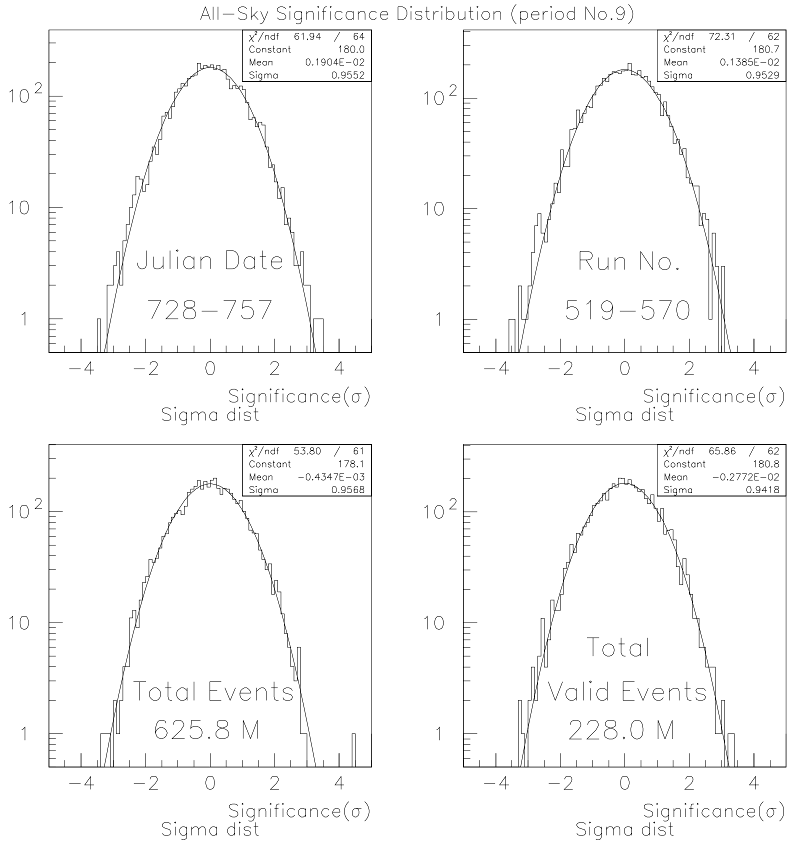

Figure 6.15: σ distributions of the 4 all-sky maps for month No.9.

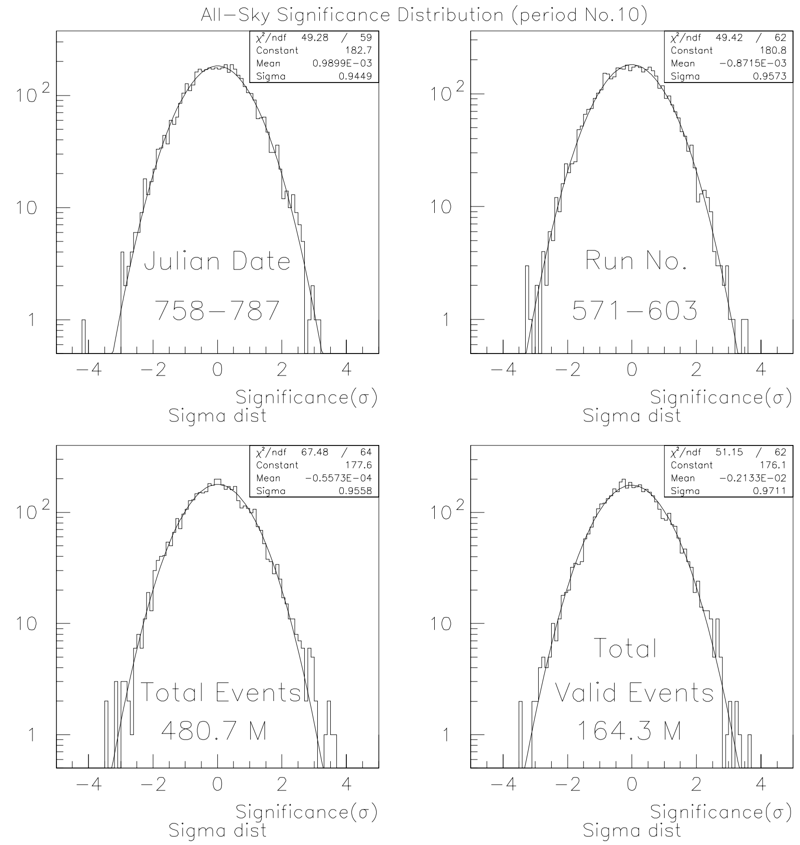

Figure 6.16: σ distributions of the 4 all-sky maps for month No.10.

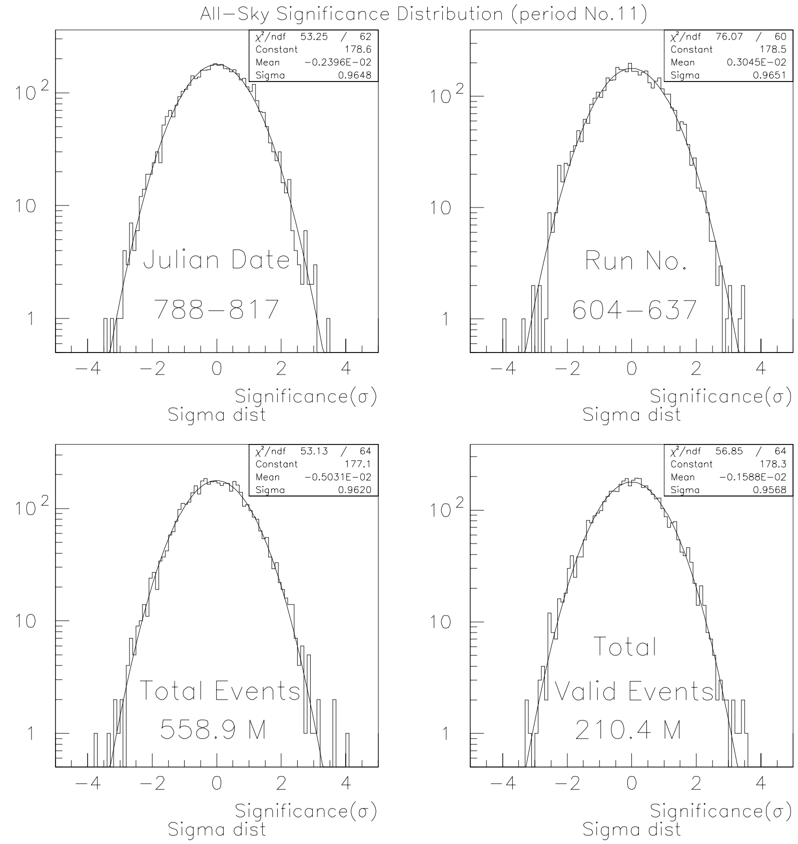

Figure 6.17: σ distributions of the 4 all-sky maps for month No.11.

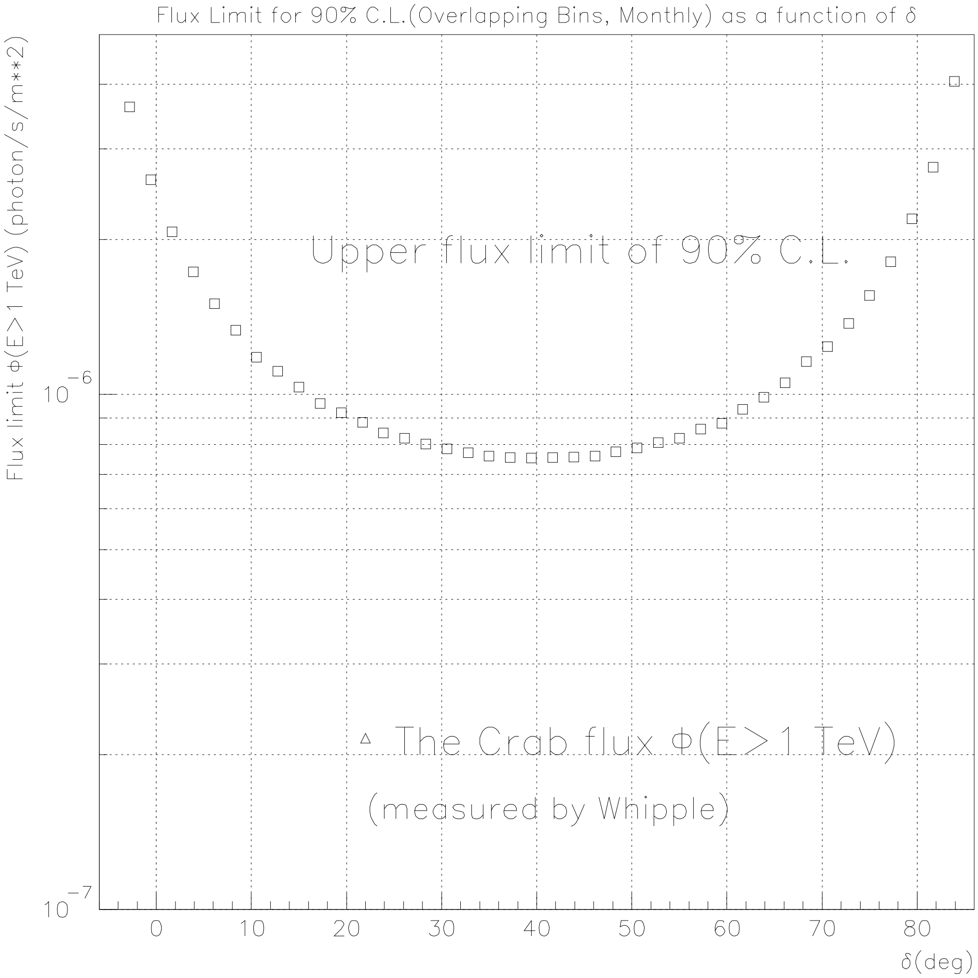

Figure 6.18: Upper flux limit of 90% CL for monthly search with overlapping bins as a function of declination for Milagrito.

Bibliography

[1] M.S. Longair. *High Energy Astrophysics, Vol. 1, 2nd Ed.* Cambridge University Press, Cambridge, England, 1992.

[2] Thomas K. Gaisser. *Cosmic Rays and Particle Physics.* Cambridge University Press, Cambridge, England, 1990.

[3] V. Barger *et al.*. *Phys. Lett. B*, 462:109–144, 1999.

[4] J. Pulido E. Kh. Akhmedov. *Phys. Lett. B*, 485:178–186, 2000.

[5] P. Vogel J. F. Beacom. *Phys. Rev. Lett.*, 83:5222–5225, 1999.

[6] H.-T. Janka W. Keil. *Phys. Rev. D*, 56:2419–2432, 1997.

[7] J. G. Learned C. Hettlage, K. Mannheim. *Astropart. Phys.*, 13:45–50, 2000.

[8] O. C. de Jager A. Mastichiadis. *Astron. Astrophys.*, 311, 1996.

[9] D. Petry *et al.*. *Astron. Astrophys.*, 311:L13–L16, 1996.

[10] M. Catanese *et al.*. Multiwavelength observations of a flare from markarian 501. *Astrophys. J. Lett.*, 487:L143–L146, 1997.

[11] M.S. Longair. *High Energy Astrophysics, Vol. 2, 2nd Ed.* Cambridge University Press, Cambridge, England, 1992.

[12] E. S. Cheng *et al.*. *Astrophys. J. Lett.*, 422:37, 1994.

[13] J.D. Jackson. *Classical Electrodynamics.* Wiley & Sons, New York, 1975.

[14] R. Nemiroff *et al.*. *Phys. Rev. Lett.*, 580:86, 2001.

[15] R. J. Protheroe T. A. Porter. *J. Phys.*, G23:1765–1784, 1997.

[16] A. A. Zdziarski. *ASP Conf. Series*, 161:16, 1999.

[17] N. Gehrels W. Chen. *Astrophys. J. Lett.*, 514, 1999.

[18] B. D. Fields *et al.*. *Astrophys. J.*, 462:276–286, 1996.

[19] S. D. Bloom *et al.*. *Astrophys. J. Lett.*, Oct. 1997.

[20] D. A. Carter-Lewis *et al.*. Spectrum of tev *gamma*-rays from the crab nebula.

[21] D. E. Alexandreas *et al.*. The cygnus extensive air-shower experiment. *Nucl. Instr. and Meth.*, A311:350–367, 1992.

[22] CASA-MIA Collaboration. *Phys. Rev. D*, 55:1714–1731, 1997.

[23] S. LeBohec *et al.*. *Astrophys. J.*, 539:209–215, 2000.

[24] A. Kawachi *et al.*. *Astropart. Phys.*, 14:261–269, 2001.

[25] G. P. Rowell *et al.*. *Astropart. Phys.*, 11:217–219, 1999.

[26] F. Aharonian *et al.*. *Astrophys. J.*, 546:898–902, 2001.

[27] Isabel Leonor. *Search for a TeV Component of Gamma-Ray Bursts Using the Milagrito Detector.* PhD thesis, University of California, Irvine, 2000.

[28] Tom Yang. *Search for High-Energy Emission from Gamma-Ray Bursts with a Large Water Cherenkov Detector.* PhD thesis, University of California, Santa Cruz, 1998.

[29] R. Atkins *et al.*. *Nucl. Instr. and Meth.*, A449:478, 2000.

[30] J. Knapp and D. Heck. *Extensive Air Shower Simulation with CORSIKA: A User's Guide.* Institut für Kernphysik, Forschungszentrum Karlsruhe, 1997.

[31] D. Heck *et al.*. *"CORSIKA: A Monte Carlo Code to Simulate Extensive Air Showers," tech report FZKA 6019.* Institut für Kernphysik, Forschungszentrum Karlsruhe, 1998.

[32] GEANT C.P.L. *GEANT Reference Manual, Version 3.21.* CERN, Geneva, Switzerland, 1994.

[33] Y. Ma T. Li. *Astrophys. J.*, 272:317–324, 1983.

[34] A. Smith. Search for point sources and emission from the galactic plane in milagrito. *Milagro Memo.*

[35] R. Atkins *et al.*. Tev observations of markarin 501 with the milagrito water cherenkov detector. *Astrophys. J. Lett.*, 525:L25–L28, November 1999.